



U.S. DEPARTMENT OF  
**ENERGY**

PNNL-23255

Prepared for the U.S. Department of Energy  
under Contract DE-AC05-76RL01830

# Simulation of Sediment and Cesium Transport in the Ukedo River and the Ogi Dam Reservoir during a Rainfall Event using the TODAM Code

Y Onishi  
H Kurikami  
ST Yokuda

March 2014



**Pacific Northwest**  
NATIONAL LABORATORY

*Proudly Operated by **Battelle** Since 1965*

## DISCLAIMER

This report was prepared as an account of work sponsored by an agency of the United States Government. Neither the United States Government nor any agency thereof, nor Battelle Memorial Institute, nor any of their employees, makes **any warranty, express or implied, or assumes any legal liability or responsibility for the accuracy, completeness, or usefulness of any information, apparatus, product, or process disclosed, or represents that its use would not infringe privately owned rights.** Reference herein to any specific commercial product, process, or service by trade name, trademark, manufacturer, or otherwise does not necessarily constitute or imply its endorsement, recommendation, or favoring by the United States Government or any agency thereof, or Battelle Memorial Institute. The views and opinions of authors expressed herein do not necessarily state or reflect those of the United States Government or any agency thereof.

PACIFIC NORTHWEST NATIONAL LABORATORY  
*operated by*  
BATTELLE  
*for the*  
UNITED STATES DEPARTMENT OF ENERGY  
*under Contract DE-AC05-76RL01830*

Printed in the United States of America

Available to DOE and DOE contractors from the  
Office of Scientific and Technical Information,  
P.O. Box 62, Oak Ridge, TN 37831-0062;  
ph: (865) 576-8401  
fax: (865) 576-5728  
email: [reports@adonis.osti.gov](mailto:reports@adonis.osti.gov)

Available to the public from the National Technical Information Service  
5301 Shawnee Rd., Alexandria, VA 22312  
ph: (800) 553-NTIS (6847)  
email: [orders@ntis.gov](mailto:orders@ntis.gov) <<http://www.ntis.gov/about/form.aspx>>  
Online ordering: <http://www.ntis.gov>



This document was printed on recycled paper.

(8/2010)

# **Simulation of Sediment and Cesium Transport in the Ukedo River and the Ogi Dam Reservoir during a Rainfall Event using the TODAM Code**

Y Onishi  
H Kurikami\*  
ST Yokuda

March 2014

Prepared for  
the U.S. Department of Energy  
under Contract DE-AC05-76RL01830

Pacific Northwest National Laboratory  
Richland, Washington 99352

\*Japan Atomic Energy Agency



# Executive Summary

The accident at the Fukushima Daiichi Nuclear Power Plant in March 2011 caused widespread environmental contamination. Although decontamination activities have been performed in residential areas of the Fukushima area, decontamination of forests, rivers, and reservoirs is still controversial because of the economical, ecological, and technical difficulties. Thus, an evaluation of contaminant transport in such an environment is important for safety assessment and for implementation of possible countermeasures to reduce radiation exposure to the public.

The investigation revealed that heavy rainfall events play a significant role in transporting radioactive cesium deposited on the land surface, via soil erosion and sediment transport in rivers. Therefore, we simulated the sediment and cesium transport in the Ukedo River and its tributaries in Fukushima Prefecture, including the Ogaki Dam Reservoir, and the Ogi Dam Reservoir of the Oginosawa River in Fukushima Prefecture during and after a heavy rainfall event by using the TODAM (Time-dependent, One-dimensional Degradation And Migration) code. The main outcomes are the following:

- Suspended sand is mostly deposited on the river bottom. Suspended silt and clay, on the other hand, are hardly deposited in the Ukedo River and its tributaries except in the Ogaki Dam Reservoir in the Ukedo River even in low river discharge conditions.
- Cesium migrates mainly during high river discharge periods during heavy rainfall events. Silt and clay play more important roles in cesium transport to the sea than sand does.
- The simulation results explain variations in the field data on cesium distributions in the river. Additional field data currently being collected and further modeling with these data may shed more light on the cesium distribution variations.
- Effects of 40-hour heavy rainfall events on clay and cesium transport continue for more than a month. This is because these reservoirs slow down the storm-induced high flow moving through these reservoirs.
- The reservoirs play a major role as a sink of sediment and cesium in the river systems. Some amounts of sediment pass through them along with cesium in dissolved and clay-sorbed cesium forms.
- Effects of countermeasures such as overland decontamination, dam control and sorbent injection were tentatively estimated. The simulation suggested that overland decontamination and sorbent injection would be effective for decreasing the contamination of water in the reservoir and in the river below the dam.



## **Acknowledgments**

This work was based on the collaborative project between the Japan Atomic Energy Agency (JAEA) and Pacific Northwest National Laboratory (PNNL) funded by JAEA. The second author has been assigned from JAEA to PNNL as a visiting scientist from April 2013 to March 2014.



## Acronyms and Abbreviations

Bq	becquerel(s)
h	hour(s)
JAEA	Japan Atomic Energy Agency
kg	kilogram(s)
km	kilometer(s)
m	meter(s)
mm	millimeter(s)
$m^2/s$	square meter(s) per second
$m^3/s$	cubic meter(s) per second
NPP	Nuclear Power Plant
Pa	pascal(s)
PNNL	Pacific Northwest National Laboratory
s	second(s)
TODAM	Time-dependent, One-dimensional Degradation And Migration
UPM	Ukedo Partial Model
USLE	Universal Soil Loss Equation
UWM	Ukedo Whole Model



# Nomenclature

The list shows only the base symbol, without superscripts, subscripts, and the like. The convention used in this document is to modify the base symbol in one or more of the following ways:

- A  $j$  subscript indicates the value applies to a single sediment fraction; for example,  $C_j$  would be the concentration of the  $j^{\text{th}}$  sediment fraction.
- An  $i$  subscript indicates the value applies to a single node; for example,  $q_i$  is the flux past the  $i^{\text{th}}$  node.
- An  $(e)$  superscript indicates the value applies to a single segment, or element, and varies with the element's basis function; for example,  $A^{(e)}(x)$  is a function that describes how the channel's cross-sectional area varies along segment  $e$ .
- The subscripts 1 or 2 are used with the  $(e)$  superscript to denote, respectively, the upstream or downstream end of the segment, for example,  $A_1^{(e)}$  would represent the channel cross-sectional area at the upstream node of segment  $e$ .

$A$	channel cross-sectional area, square meters	$K_a$	armorng coefficient, nondimensional, ranging from 0.0 to 1.0
$B$	channel bed width, meters	$K_{bj}$	mass transfer rate between $j^{\text{th}}$ bed sediment-associated and dissolved contaminant, seconds <sup>-1</sup>
$C_j$	$j^{\text{th}}$ sediment concentration, or general constituent concentration, kilograms per cubic meter	$K_C$	first-order reaction rate of dissolved contaminant degradation from causes other than radioactive decay, days <sup>-1</sup>
$D$	flow depth, meters	$K_d$	contaminant distribution coefficient, cubic meters per kilogram
$d$	sediment particle diameter, meters	$K_j$	mass transfer rate between $j^{\text{th}}$ suspended sediment-associated and dissolved contaminant, seconds <sup>-1</sup>
$d_{50}$	median diameter of bed sediment, meters	$L$	segment length, meters
$G_{Bj}$	contaminant concentration in $j^{\text{th}}$ bed sediment, Bq or Curies per kilogram	$M$	erodibility coefficient, kilograms per square meter per second
$G_j$	$j^{\text{th}}$ sediment-associated contaminant concentration, becquerels (Bq) per cubic meter	$n$	bed sediment porosity
$G_w$	dissolved contaminant concentration, Bq per cubic meter	$Q$	flow rate, cubic meters per second, cubic meters per day
$k$	the Von Karman constant = 0.4	$Q_l$	tributary and lateral inflow of water, cubic meters per day per meter or cubic meters per second per meter
$k_a$	Nikuradse sand roughness, meters		

$Q_{pj}$	tributary and lateral inflow contribution of $j^{th}$ sediment-associated contaminant, Bq per day per meter or Bq per second per meter	$x$	station or longitudinal coordinate, meters
$Q_{sj}$	tributary and lateral inflow contribution of $j^{th}$ sediment, kilograms per day per meter or kilograms per second per meter	$\gamma$	specific weight of sediment solids, kilograms (force) per cubic meter
$Q_T$	noncohesive sediment transport capacity, kilograms per meter per day	$\gamma_w$	specific weight of water, kilograms (force) per cubic meter
$Q_{Ta}$	actual noncohesive sediment transport rate, kilograms per meter per day	$\Delta t$	simulation time step, days
$Q_w$	tributary and lateral inflow contribution of dissolved contaminant, Bq per second per meter	$\varepsilon_x$	longitudinal dispersion coefficient, square meters per second
$R$	channel hydraulic radius, meters	$\lambda$	radioactive decay rate, days <sup>-1</sup> or seconds <sup>-1</sup>
$S$	channel slope, nondimensional	$\rho$	water density, kg per cubic meter
$S_{Dj}$	$j^{th}$ sediment deposition rate, kilograms per square meter per day	$v_s$	effective particle settling velocity, meters per day or meters per second
$S_{Rj}$	$j^{th}$ sediment erosion rate, kilograms per square meter per day	$\tau_b$	bed shear stress, kilograms per square meter
$t$	time, days or seconds	$\tau_{Dc}$	critical shear stress for deposition, kilograms per square meter
$T$	standard bed layer thickness, meters	$\tau_{Rc}$	critical shear stress for erosion, kilograms per square meter
$U$	longitudinal flow velocity, meters per day or meters per second		
$U_*$	shear velocity, meters per day or meters per second		

# Contents

Executive Summary .....	iii
Acknowledgments.....	v
Acronyms and Abbreviations .....	vii
Nomenclature.....	ix
1.0 Introduction .....	1.1
2.0 TODAM Model Description .....	2.1
2.1 Sediment Transport .....	2.1
2.2 Sediment-Sorbed Contaminant Transport.....	2.4
2.3 Dissolved Contaminant Transport.....	2.5
2.4 Discretization and Solution .....	2.6
2.5 Channel Branching.....	2.7
2.6 Bed Materials Accounting.....	2.9
3.0 Ukedo River Modeling.....	3.1
3.1 Description of the Ukedo River .....	3.1
3.2 Simulation in Low and High River Discharge Conditions using the Ukedo Partial Model .....	3.5
3.2.1 Analytical Conditions.....	3.5
3.2.2 Simulation Results.....	3.9
3.3 Sequential Simulation during a Rainfall Event using the Ukedo Whole Model.....	3.19
3.3.1 Analytical Conditions.....	3.19
3.3.2 Simulation Results.....	3.22
3.3.3 Effects of Countermeasures.....	3.30
4.0 Ogi Dam Modeling.....	4.1
4.1 Description of the Ogi Dam Reservoir.....	4.1
4.2 Simulation Results.....	4.3
4.2.1 Analytical Conditions.....	4.3
4.2.2 Simulation Results.....	4.5
5.0 Conclusions .....	5.1
6.0 References .....	6.1

## Figures

2.1	Schematics of Two Cases Where Junctions are Used.....	2.9
3.1	Contamination Map around the Fukushima NPP and the Ukedo River with its tributaries .....	3.1
3.2	The Ukedo River in the Mountainous Area.....	3.2
3.3	The Ukedo River in the Flat Area.....	3.3
3.4	The Ukedo River near the River Mouth .....	3.3
3.5	Evolution of Air Dose Rate Distribution along the Ukedo River Obtained by Airborne Surveys.....	3.4
3.6	The Ukedo Partial Model Setup.....	3.4
3.7	The Ukedo Whole Model Setup .....	3.5
3.8	Conceptual Image of Cesium Transport in the Ukedo River in Low and High River Discharge Conditions.....	3.6
3.9	The USLE Grid and Lateral Inflow Applied to the River Model .....	3.7
3.10	Elevation of the Riverbed .....	3.7
3.11	Longitudinal Distribution of the River Widths under Low and High Flow Conditions .....	3.8
3.12	Distribution of the River Discharge Rate during Low River Discharge.....	3.10
3.13	Distribution of the River Depth during Low River Discharge.....	3.10
3.14	Distribution of the River Velocity during Low River Discharge.....	3.11
3.15	Spatial Distributions of Suspended Sediment Concentrations during Low River Discharge .....	3.12
3.16	Spatial Distributions of Sediment-Sorbed Cesium Concentrations during Low River Discharge .....	3.12
3.17	Spatial Distributions of the Total Cesium Concentrations in the Flow during Low River Discharge .....	3.13
3.18	Distribution of the Bed Layer Thickness during Low River Discharge .....	3.13
3.19	Distribution of Cesium in the Riverbed during Low River Discharge .....	3.14
3.20	River Discharge Rate in the High Flow Case Compared with that in the Low Flow Case .....	3.14
3.21	Distributions of the Water Depth in the Low and High Flow Cases .....	3.15
3.22	Distributions of the Velocity in the Low and High Flow Cases .....	3.15
3.23	Distributions of Suspended Sediment Concentrations during High Flow Conditions.....	3.16
3.24	Distributions of the Total Cesium Concentrations in the Flow during High Flow Conditions ....	3.17
3.25	Distributions of Sediment-Sorbed Cesium Concentrations during High Flow Conditions .....	3.17
3.26	Distribution of the Bed Layer Thickness during High Flow Conditions.....	3.18
3.27	Distribution of the Cesium in the Riverbed during High Flow Conditions .....	3.18
3.28	Elevation of the Riverbed along the Ukedo River .....	3.20
3.29	Distribution of the River Width along the Ukedo River.....	3.20
3.30	River Discharge Rate in the High Flow Condition during the Rainfall Event and in the Low Flow Condition after the Rainfall Event.....	3.22
3.31	Distributions of Depth in the Low and the High River Discharge Conditions along the Ukedo River.....	3.22

3.32 Distributions of Velocity in the Low and the High River Discharge Conditions along the Ukedo River .....	3.23
3.33 Distributions of Concentrations of Suspended Sand at 40 Hours, 60 Hours, and 1000 Hours.....	3.24
3.34 Distributions of Concentrations of Suspended Silt at 40 Hours, 60 Hours, and 1000 Hours .....	3.24
3.35 Distributions of Concentrations of Suspended Clay at 40 Hours, 60 Hours, and 1000 Hours .....	3.25
3.36 Distributions of Suspended Sediment Concentrations at 1000 Hours .....	3.25
3.37 Distributions of Concentrations of Dissolved Cesium at 40 Hours, 60 Hours, and 1000 Hours.....	3.26
3.38 Distributions of Concentrations of Particulate Cesium at 40 Hours, 60 Hours, and 1000 Hours.....	3.26
3.39 Distributions of Cesium Concentrations in the Flow at 1000 Hours .....	3.27
3.40 Time Histories of Concentrations of Dissolved Cesium.....	3.28
3.41 Time Histories of Concentrations of Particulate Cesium.....	3.28
3.42 Distribution of Riverbed Thickness .....	3.29
3.43 Distribution of Riverbed Contamination .....	3.29
3.44 Distribution of Sediments in the Bed of the Ogi Dam Reservoir.....	3.30
3.45 Results of Countermeasure Simulations .....	3.31
4.1 Location of the Ogi Dam and Images of the Area .....	4.1
4.2 Contours of the Bed Elevation in the Ogi Dam Reservoir.....	4.2
4.3 Bed Elevation of the Ogi Dam Reservoir along the Thalweg.....	4.2
4.4 Width of the Ogi Dam Reservoir along the Thalweg .....	4.3
4.5 Velocity Distributions Estimated by the Jet Mixing Theory for $x = 0.1-100$ m.....	4.4
4.6 Velocity Distributions Estimated by the Jet Mixing Theory for $x = 100-580$ m.....	4.4
4.7 Boundary Conditions for Simulation of the Ogi Dam Reservoir.....	4.5
4.8 Distributions of Concentrations of Suspended Sand in the Ogi Dam Reservoir .....	4.6
4.9 Distributions of Concentrations of Suspended Silt in the Ogi Dam Reservoir.....	4.6
4.10 Distributions of Concentrations of Suspended Clay in the Ogi Dam Reservoir.....	4.7
4.11 Distributions of Sediment in the Ogi Dam Reservoir Bed.....	4.7
4.12 Distributions of Dissolved Cesium Concentration in the Ogi Dam Reservoir .....	4.8
4.13 Distributions of Dissolved Cesium Concentration in the Ogi Dam Reservoir (magnified).....	4.8
4.14 Distributions of Clay-Sorbed Cesium Concentration in the Ogi Dam Reservoir .....	4.9

## Tables

3.1 Parameters Used in the Low and High Flow Simulations .....	3.8
3.2 Parameters Used in the Simulations during a Rainfall Event .....	3.21
4.1 Mass Balances of Sediments in the Ogi Dam Reservoir .....	4.9
4.2 Mass Balance of Cesium in the Ogi Dam Reservoir .....	4.9



# 1.0 Introduction

The accident at the Fukushima Daiichi Nuclear Power Plant (NPP) in March 2011 caused widespread environmental contamination. Although decontamination activities have been performed in the residential areas of the Fukushima area, decontamination of forests, rivers, and reservoirs is still controversial because of the economical, ecological, and technical difficulties. Thus, evaluation of contaminant transport in such an environment is important for safety assessment and for countermeasures to diminish radiation exposure to the public.

The previous study (e.g., JAEA 2013a) revealed that heavy rainfall events play a significant role in transporting radioactive cesium via land erosion and sediment transport in rivers. To understand such transport behaviors of radioactive contaminants in environment, the Japan Atomic Energy Agency (JAEA) initiated the F-TRACE (long-term assessment of Transport of RAdioactive Contaminant in the Environment of Fukushima) project (Iijima et al. 2013) in the fall of 2012. In the project, several rivers and reservoirs near the Fukushima Daiichi NPP have been investigated. Among them, the Ukedo River is considered the most important river from the viewpoint of contaminant transport, because it is the most contaminated river and it had widely supplied irrigation water to the coastal area before the accident.

The Pacific Northwest National Laboratory (PNNL)-JAEA collaborative team initiated the numerical simulation of the Ukedo River using the TODAM (Time-dependent, One-dimensional Degradation And Migration) model (Onishi et al. 2007) in Fiscal Year 2012 (Onishi and Yokuda 2013; Kurikami et al. 2013). In this report, the Ukedo River model was updated based on the updates of the investigation results (JAEA 2013a, 2013b). This study focused on rainfall events in particular.

In addition to the Ukedo River simulation, the Ogi Dam reservoir in Fukushima was simulated using the TODAM model. It has been studied in the project as the representative reservoir in the area (Funaki et al. 2013).



## 2.0 TODAM Model Description

TODAM is a finite-element, time-varying, one-dimensional code to simulate sediment and contaminant transport in rivers and estuaries, both in water columns and within river-estuarine bottoms (Onishi et al. 2007). It consists of three submodels of sediment, dissolved contaminant, and sediment-sorbed contaminant transport to simulate sediment and contaminant migration along with their interactions, e.g., adsorption-desorption with sediment, transport, and deposition and resuspension of sediment and sediment-sorbed contaminants. Sediment is divided into three size fractions, usually one for noncohesive sediment (e.g., sand), and the other two for cohesive sediment, (e.g., silt and clay) and/or an organic material.

TODAM was developed by PNNL to predict time-varying longitudinal distributions of the following parameters:

- in the river and estuarine water column
  - concentrations of
    - suspended sand
    - suspended silt
    - suspended clay
  - dissolved contaminant (e.g., radionuclide, heavy metal, and toxic chemical) concentration
  - particulate contaminant concentrations adsorbed by
    - suspended sand
    - suspended silt
    - suspended clay
- in the river and estuarine bed at any given downstream location
  - river/estuarine bed elevation change caused by sediment erosion and deposition
  - vertical distributions of sediment fractions of
    - bottom sand
    - bottom silt
    - bottom clay
  - vertical distributions of contaminant concentrations adsorbed by
    - bottom sand
    - bottom silt
    - bottom clay.

The TODAM model uses the principle of conservation of mass to predict these parameters.

### 2.1 Sediment Transport

Because the movements and contaminant adsorption capacities of sediments vary significantly with sediment sizes, the sediment transport submodel describes the migration of sediment (transport,

deposition, and resuspension) for three sediment size fractions of cohesive and noncohesive sediments. The sediment transport submodel includes mechanisms of

1. advection and dispersion of sediments;
2. fall velocity and cohesiveness;
3. deposition on the river and estuarine bed;
4. resuspension from the river and estuarine bed;
5. sediment contributions from tributaries and point and nonpoint sources into the river and estuarine systems.

Sediment mineralogy and water quality effects are implicitly included through Mechanisms 2, 3, and 4 above.

Mass conservation of sediment passing through a control volume combined with the equation of continuity leads to the following expression for the one-dimensional sediment transport:

$$A \frac{\partial C_j}{\partial t} + UA \frac{\partial C_j}{\partial x} = \frac{\partial}{\partial x} \left( \varepsilon_x A \frac{\partial C_j}{\partial x} \right) - Q_l C_j + B (S_{R_j} - S_{D_j}) + Q_{S_j} \quad (2.1)$$

where

- $C_j$  = the concentration of sediment of the  $j^{\text{th}}$  size fraction, kilograms per cubic meter
- $A$  = channel cross-sectional flow area, square meters
- $B$  = channel bed width, meters
- $Q_{S_j}$  = sediment contribution of the  $j^{\text{th}}$  size fraction from tributary and/or lateral inflow, kilograms per meter per day
- $S_{D_j}$  = deposition rate of sediment, kilograms per square meter per day
- $S_{R_j}$  = erosion rate of bed sediment, kilograms per square meter per day
- $U$  = longitudinal flow velocity, meters per day
- $\varepsilon_x$  = longitudinal dispersion coefficient, square meters per day
- $Q_l$  = net lateral inflow, cubic meters per day per meter
- $t$  = time, days
- $x$  = station or longitudinal coordinate, meters

TODAM simulates the transport of three separate sediment size classes using Equation (2.1). These classes are nominally called “sand,” “silt,” and “clay” in this document. The “sand” class is considered to be noncohesive; “silt” and “clay” are both considered to be cohesive. Erosion and deposition, represented by  $S_R$  and  $S_D$  in Equation (2.1), are computed differently for cohesive and noncohesive sediment classes. For noncohesive sediment (“sand”),  $S_R$  and  $S_D$  are computed as

$$S_R = \begin{cases} K_a \left( \frac{Q_T - Q_{Ta}}{\Delta x} \right) & \text{for } Q_T > Q_{Ta} \\ 0.0 & \text{for } Q_T \leq Q_{Ta} \end{cases} \quad (2.2)$$

and

$$S_D = \begin{cases} \frac{Q_{Ta} - Q_T}{\Delta x} & \text{for } Q_{Ta} > Q_T \\ 0.0 & \text{for } Q_{Ta} \leq Q_T \end{cases} \quad (2.3)$$

where

- $K_a$  = an armoring coefficient, ranging from 0.0 to 1.0
- $Q_T$  = the (noncohesive) sediment transport capacity, kilograms per meter (of width) per day
- $Q_{Ta}$  = the actual sediment transport rate, kilograms per meter per day
- $\Delta x$  = the length of the stream segment under consideration, meters.

Erosion rates are limited by available bed sediment (see Section 2.6). Three methods are available in TODAM to compute sediment transport capacity:

- The *Du Boys* method (Du Boys 1879) as described by Vanoni (1975)
- The *Toffaletti* formula (Toffaletti 1969), as described by Vanoni (1975)
- The *Colby* method (Colby 1964) as described by Vanoni (1975).

Erosion and deposition of cohesive sediment fractions are estimated by formulas of Partheniades (1962) and Krone (1962):

$$S_R = \begin{cases} K_a M \left( \frac{\tau_b}{\tau_{Rc}} - 1 \right) & \text{for } \tau_b \geq \tau_{Rc} \\ 0.0 & \text{for } \tau_b < \tau_{Rc} \end{cases} \quad (2.4)$$

and

$$S_D = \begin{cases} C v_s \left( 1 - \frac{\tau_b}{\tau_{Dc}} \right) & \text{for } \tau_b \leq \tau_{Dc} \\ 0.0 & \text{for } \tau_b > \tau_{Dc} \end{cases} \quad (2.5)$$

where

- $M$  = erodibility coefficient, kilograms per square meter per day
- $\tau_b$  = bed shear stress, kilograms per square meter
- $\tau_{Dc}$  = critical bed shear stress for deposition, kilograms per square meter
- $\tau_{Rc}$  = critical bed shear stress for erosion, kilograms per square meter
- $v_s$  = effective particle settling velocity, meters per day.

In TODAM, the bed shear stress,  $\tau_b$ , can be read as input data, or it can be estimated in one of two ways within TODAM. The first is used for running streams with a nonzero slope:

$$\tau_b = \gamma_w SR \quad (2.6)$$

where  $\tau_b$  = bed shear stress, kilograms per square meter  
 $\gamma_w$  = the specific weight of water, kilograms (force) per cubic meter  
 $S$  = the channel bottom slope, meters per meter  
 $R$  = the channel's hydraulic radius, meters.

The second method is more suited to reservoirs, for example, where the energy slope is different from the channel slope:

$$\tau_b = \frac{\rho}{g} U_*^2 \quad (2.7)$$

where  $g$  is the acceleration of gravity, meters per square second and  $U_*$  is the shear velocity, meters per second, and  $\rho$  is the water density;

$U_*$  is computed by Graf (1971), as

$$U_* = \frac{U}{17.66 + \frac{2.3}{k} \log \left( \frac{D}{96.5k_a} \right)}$$

where  $D$  = the flow depth, meters  
 $k_a$  = the Nikuradse sand roughness, meters, which  
= the median bed sediment diameter,  $d_{50}$ , according to Chow (1959)  
 $k$  = the Von Karman constant = 0.4.

## 2.2 Sediment-Sorbed Contaminant Transport

The transport submodel of contaminant attached to sediment includes the following mechanisms:

1. advection and dispersion of particulate (sediment-sorbed) contaminant
2. adsorption of dissolved contaminant by both moving (suspended and bed-load sediment) and stationary bottom sediment or desorption from these sediments into water
3. radioactive decay
4. deposition of particulate contaminant to the river or estuary bed or resuspension from the bed
5. contributions of particulate contaminants from tributaries and point and nonpoint sources into the river and estuarine systems.

As in the sediment transport, conservation of contaminant adsorbed by each size fraction of three sediment sizes may be expressed with the help of the equation of continuity as

$$\begin{aligned}
A \frac{\partial G_j}{\partial t} + UA \frac{\partial G_j}{\partial x} = & \frac{\partial}{\partial x} \left( \epsilon_x A \frac{\partial G_j}{\partial x} \right) - \lambda A G_j - Q_l G_j \\
& + B \left( G_{B_j} S_{R_j} - \frac{S_{D_j} G_j}{C_j} \right) + Q_{P_j} + A K_j (K_{d_j} C_j G_w - G_j)
\end{aligned} \tag{2.8}$$

- where
- $G_j$  = the concentration of contaminant associated with the  $j^{\text{th}}$  sediment fraction, becquerels (Bq) or kg per cubic meter
  - $\lambda$  = the contaminant degradation or radioactive decay rate,  $\text{day}^{-1}$
  - $G_{B_j}$  = the contaminant concentration in bed sediments of the  $j^{\text{th}}$  fraction, Bq (or kg) per kilogram
  - $Q_{P_j}$  = the contribution of contaminant associated with the  $j^{\text{th}}$  sediment size fraction from tributary and lateral inflow, Bq (or kg) per meter per day
  - $K_j$  = the mass transfer rate for dissolved contaminant adsorption to and desorption from suspended sediment of the  $j^{\text{th}}$  fraction,  $\text{day}^{-1}$
  - $K_{d_j}$  = the distribution coefficient between dissolved contaminant and sediment-associated contaminant in the  $j^{\text{th}}$  sediment fraction (both suspended and bed), cubic meters per kilogram
  - $G_w$  = the dissolved contaminant concentration, Bq (or kg) per cubic meter.

TODAM simulates the transport of contaminant associated with three separate sediment size classes using Equation (2.8).

## 2.3 Dissolved Contaminant Transport

The dissolved contaminant transport submodel includes the following mechanisms:

1. advection and dispersion of dissolved contaminant
2. adsorption of dissolved contaminant by each size fraction of moving (suspended and bed-load sediments) and stationary bottom sediment, or desorption from these sediments into water
3. degradation of dissolved contaminant due to hydrolysis, oxidation, photolysis, and microbial activities
4. volatilization
5. radioactive decay
6. contributions from tributaries and point and nonpoint sources into the river and estuarine systems.

Effects of water quality (for example, pH, water temperature, salinity) and clay minerals on contaminant adsorption and desorption are taken into account through changes in the distribution coefficients for adsorption and desorption,  $K_{d_j}$ .

Conservation of dissolved contaminant in a control volume may expressed as

$$\begin{aligned}
 A \frac{\partial G_w}{\partial t} + UA \frac{\partial G_w}{\partial x} &= \frac{\partial}{\partial x} \left( \varepsilon_x A \frac{\partial G_w}{\partial x} \right) \\
 &- \lambda A G_w - \sum_{i=1}^5 K_{C_i} A G_w - Q_l G_w + Q_w \\
 &- \sum_{j=1}^{N_f} A K_j (K_{d_j} C_j G_w - G_j) \\
 &- \sum_{j=1}^{N_f} B \gamma_j (1-n) d_j K_{b_j} (K_{d_j} G_w - G_{B_j})
 \end{aligned} \tag{2.9}$$

where

- $K_{C_i}$  = first-order reaction rates of dissolved contaminant degradation from causes other than radioactive decay, days<sup>-1</sup>
- $Q_w$  = the contribution of dissolved contaminant from tributary and lateral inflow, Bq (or kg) per meter per day
- $\gamma_j$  = the solids density of the  $j^{\text{th}}$  sediment size fraction, kilograms per cubic meter
- $n$  = bed sediment porosity
- $d_j$  = (median) particle diameter of the  $j^{\text{th}}$  sediment fraction, meters
- $K_{b_j}$  = mass transfer rate for dissolved contaminant adsorption to and desorption from the  $j^{\text{th}}$  bed sediment fraction, days<sup>-1</sup>.

The  $K_{C_i}$  rate constants are used in Equation (2.9) to account for volatilization and for chemical and biological degradation due to

- hydrolysis
- oxidation
- photolysis
- microbial activities.

## 2.4 Discretization and Solution

TODAM uses the Galerkin finite-element method to estimate solutions to the sediment and contaminant transport equations (Equations (2.1), (2.8) and (2.9)) in space. In the Galerkin method, the problem domain is divided into smaller “elements” or “segments.” Each segment is considered to have a “node” at each end. A set of equations is computed for each segment in the domain. These have the form

$$[P^{(e)}] \left\{ \frac{da^{(e)}}{dt} \right\} + [S^{(e)}] \{a^{(e)}\} = \{R^{(e)}\} \tag{2.10}$$

where vector  $\{a\}$  is the approximation of concentration at the nodes, and matrices  $[P^{(e)}]$ ,  $[S^{(e)}]$  and vector  $\{R^{(e)}\}$  are the coefficient matrices and vector of the  $e$ -th segment, respectively. These equations are called

the typical or local element equations. Once computed, the local element equations are assembled (by linear combinations) into a system of equations for the entire domain. These have the form

$$[P] \left\{ \frac{da}{dt} \right\} + [S] \{a\} = \{R\} \quad (2.11)$$

where the vector  $\{a\}$  is the approximation of concentration at all nodes in the domain. In TODAM, it is assumed that

$$a = \theta a^t + (1-\theta) a^{t+\Delta t}$$

where  $\theta$  is between 0 and 1. Substituting this into Equation (2.11) produces

$$[P] \frac{\{a\}^{t+\Delta t} - \{a\}^t}{\Delta t} = -[S] \{\theta \{a\}^t + (1-\theta) \{a\}^{t+\Delta t}\} + \{R\}$$

Solving for the future time step,  $t + \Delta t$ , the above equation becomes

$$[P] \{a\}^{t+\Delta t} = [S] \{a\}^t + \{R\} \quad (2.12)$$

where the new coefficient matrices are

$$[P] = [P] + (1-\theta) \Delta t [S] \quad (2.13)$$

$$[S] = [P] - \theta \Delta t [S] \quad (2.14)$$

and

$$\{R\} = \Delta t \{R\} \quad (2.15)$$

Certain equations in the system of Equation (2.12) are replaced with boundary conditions and junction mass-balance equations. The system is then solved for the concentrations at each node.

## 2.5 Channel Branching

Although TODAM is a one-dimensional code, it can handle channel branching with the use of “junctions.” A “junction” is a collection of nodes where several rivers merge and/or diverge (Figure 2.1). At a junction, sediment and contaminant mass are balanced by setting the sum of both advective and dispersive fluxes into the junction equal to zero:

$$\sum_{i=1}^{N_j} \left( Q_i C_i - \varepsilon_x A_i \left. \frac{dC}{dx} \right|_i \right) = 0 \quad (2.16)$$

where  $N_j$  is the number of nodes in the junction.

The concentration gradient at a node needs to be estimated. This is performed using the concentration at the nearest node. For example, the concentration gradient for Node 3 in Figure 2.1(a) would be estimated as

$$\left. \frac{dC}{dx} \right|_3 \approx \frac{C_4 - C_3}{L^{(b)}} \quad (2.17)$$

where  $L$  is the length of the segment in meters and  $b$  is the segment designation in Figure 2.1(a).

Applying the mass balance to the confluence situation shown in Figure 2.1(a) results in

$$\begin{aligned} & Q_3 C_3 + \varepsilon_x^{(b)} A_3 \frac{C_4 - C_3}{L^{(b)}} \\ & + Q_5 C_5 + \varepsilon_x^{(c)} A_5 \frac{C_6 - C_5}{L^{(c)}} \\ & - Q_2 C_2 - \varepsilon_x^{(a)} A_2 \frac{C_2 - C_1}{L^{(a)}} = 0 \end{aligned} \quad (2.18)$$

Figure 2.1(b) results in

$$\begin{aligned} & Q_2 C_2 + \varepsilon_x^{(a)} A_2 \frac{C_1 - C_2}{L^{(a)}} \\ & - Q_5 C_5 - \varepsilon_x^{(c)} A_5 \frac{C_5 - C_6}{L^{(c)}} \\ & - Q_3 C_3 - \varepsilon_x^{(b)} A_3 \frac{C_3 - C_4}{L^{(b)}} = 0 \end{aligned} \quad (2.19)$$

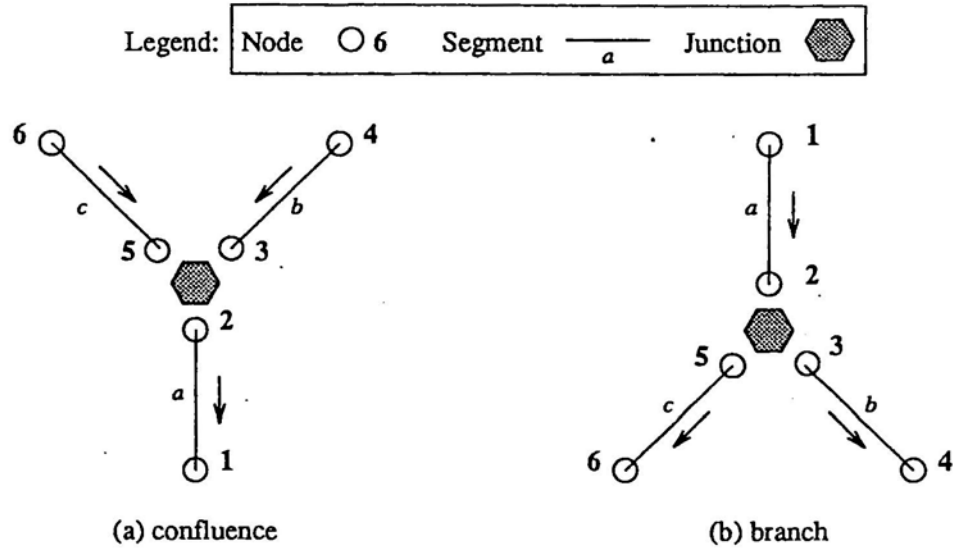


Figure 2.1. Schematics of Two Cases Where Junctions are Used

Additionally, the condition that all outflow node concentrations must be equal for the branch case (b), (in this case  $C_3 - C_5 = 0$ ), is linearly combined with the equation for the remaining outflow nodes (in this case node 5).

## 2.6 Bed Materials Accounting

TODAM maintains an accounting of available bed materials. These materials are affected by erosion/deposition and adsorption/desorption predicted by the sediment and contaminant transport submodels. Bed materials are conceptualized as a series of horizontal material layers, of some “standard” thickness,  $T$ , lying above an unerodable bedrock. The standard layer thickness is constant within a segment, but the bed surface layer thickness can vary depending on the sediment erosion or deposition during a simulation. Depending on suspended-sediment deposition or bed erosion, the number of bed layers can increase or decrease. The materials have a spatially constant (within a segment) porosity which is assumed to be completely filled with water. The accounting performed by TODAM considers the following:

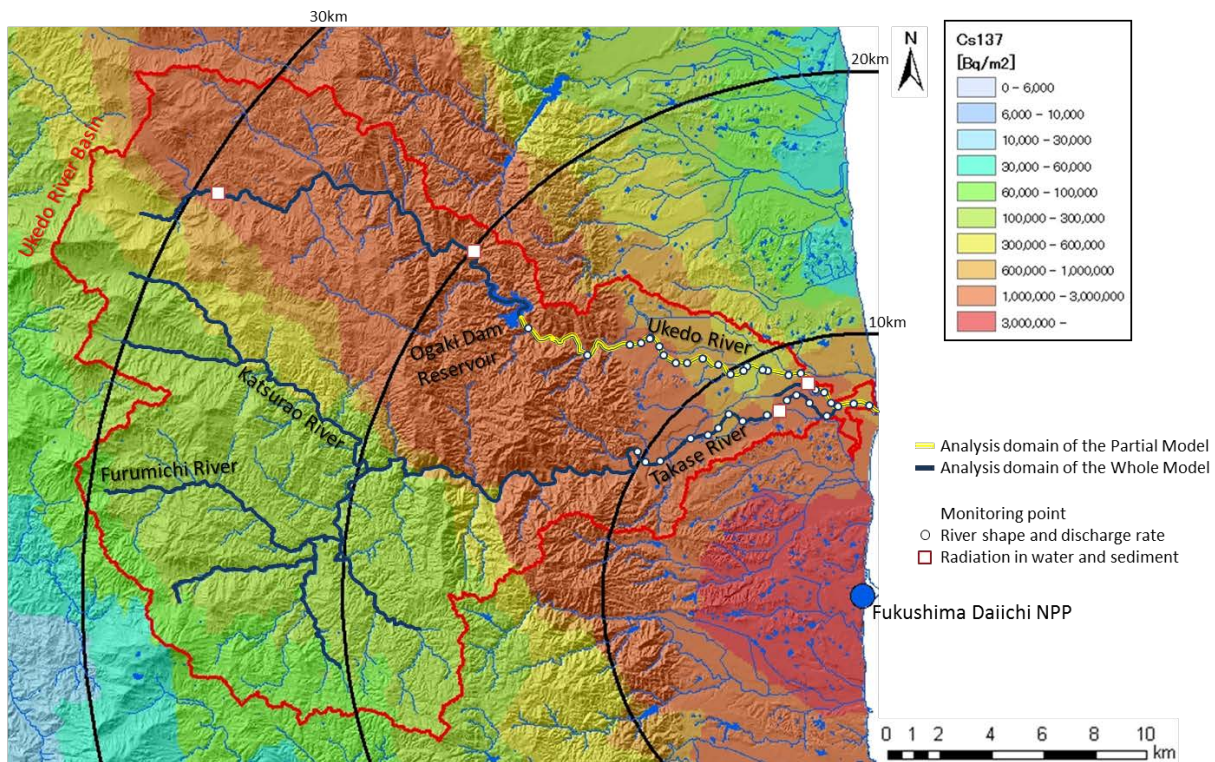
- erosion from and deposition to bed
- contaminant decay within bed
- contaminant movement (diffusion) within bed



## 3.0 Ukedo River Modeling

### 3.1 Description of the Ukedo River

The Ukedo River, whose length is about 50 km, is located northwest of the Fukushima Daiichi NPP (Figure 3.1). It originates in the Abukuma Mountains and flows into the Pacific Ocean. The Ogaki Dam is on the Ukedo River 22 km upstream of the river mouth. The Takase River, whose discharge rate is several times as high as that of the Ukedo River, merges into the Ukedo River around 2 km from the river mouth. After the Takase River merges, the Ukedo River width increases several times. Figure 3.2, Figure 3.3, and Figure 3.4 are photographs of the river in the mountainous area, in the flat area and near the river mouth, respectively. The riverbed is mostly covered by gravels or larger grains in the mountainous area, while sand deposition can be found in the flat area.



The Contamination Map was drawn using Environment Monitoring Database for the Distribution of Radioactive Substances Released by the TEPCO Fukushima Dai-ichi NPP Accident ©2013 Nuclear Regulation Authority. Topography with rivers was drawn using National Land Numerical Information © 1974-2013 National Information Division, National Spatial Planning and Regional Policy Bureau, MLT of Japan.

**Figure 3.1.** Contamination Map around the Fukushima NPP and the Ukedo River with its tributaries

Figure 3.1 also shows the distribution of concentration of cesium-137. The Ukedo River is one of the most contaminated rivers in the area. The upper part, in particular, is highly contaminated. Figure 3.5 shows the evolution of air dose rate distribution along the river obtained by airborne surveys. It can be seen that the air dose rate increases in the floodplain at the lower part that represents the flat area. It reveals that the radionuclides migrate along the river, especially during floods.

The river discharge rate at the river mouth is usually about  $10 \text{ m}^3/\text{s}$ , but it increases significantly after heavy rainfall events. The local government estimates the peak rate is  $3000 \text{ m}^3/\text{s}$  (Fukushima Prefecture 2005).

For the Ukedo River application, the CHARIMA model (Holly et al. 1990) (see the appendix) was used to simulate the river flow, while TODAM was used to model sediment and cesium transport.



**Figure 3.2.** The Ukedo River in the Mountainous Area



**Figure 3.3.** The Ukedo River in the Flat Area



**Figure 3.4.** The Ukedo River near the River Mouth

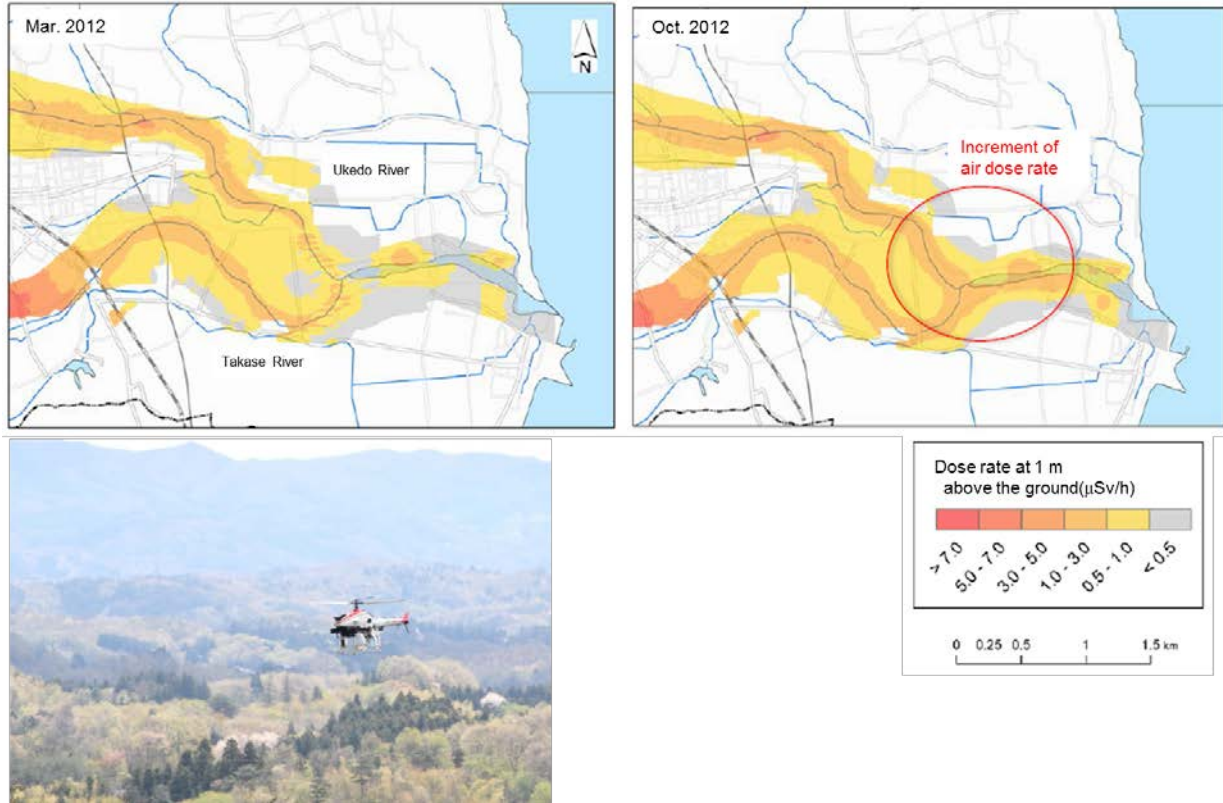


**Figure 3.5.** Evolution of Air Dose Rate Distribution along the Ukedo River (top) Obtained by Airborne Surveys (bottom)

In order to evaluate the impact of rainfall events, two geometry models were developed: the Ukedo Partial Model (UPM, Figure 3.6) for simulation in low and high river discharge conditions and the Ukedo Whole Model (UWM, Figure 3.7) for sequential simulation during and after a rainfall event. In the UPM, the 22 km portion from the Ogaki Dam to the river mouth at the sea was divided into 220 segments. The UWM includes not only the full Ukedo River but also the dam in the middle part and the tributaries including the Takase River. The total length in the UWM was about 130 km and the number of segments was 518.

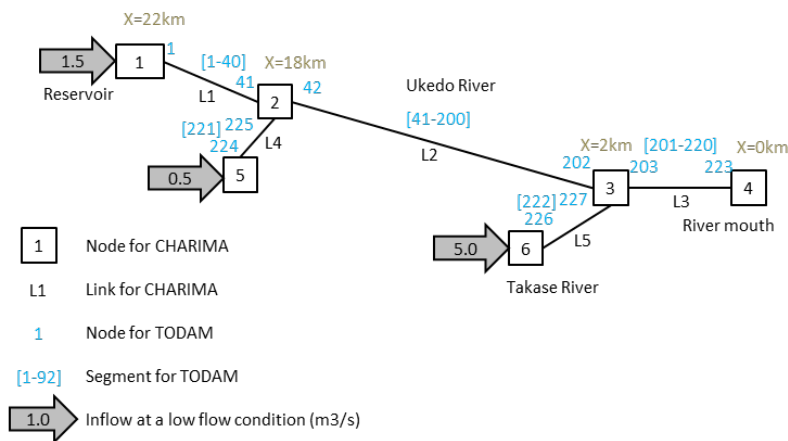


**Figure 3.6.** The Ukedo Partial Model (UPM) Setup

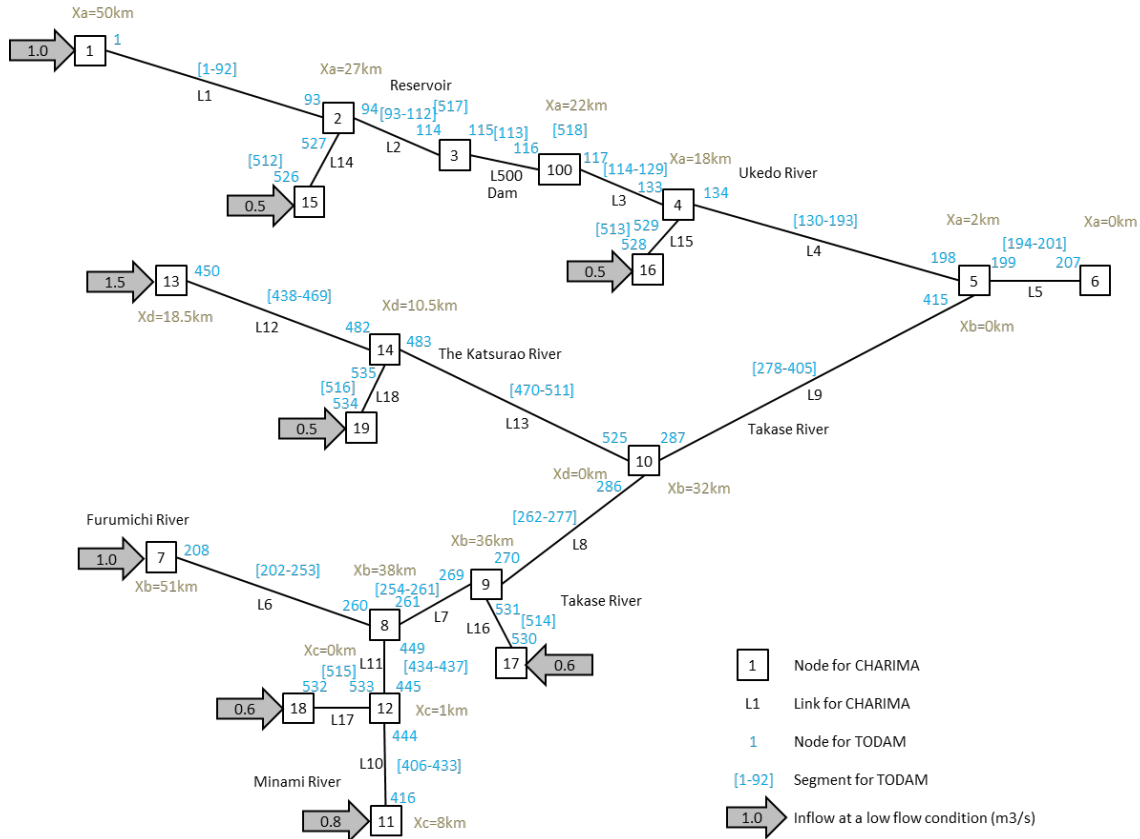


**Figure 3.7.** The Ukedo Whole Model (UWM) Setup

Since the water from the rivers and the dam located in the middle part had been supplied to the rice paddy fields at the lower residential area before the accident, restoration of the rivers is in the interest of the local residents.

## 3.2 Simulation in Low and High River Discharge Conditions using the Ukedo Partial Model (UPM)

### 3.2.1 Analytical Conditions

Using the UPM (Figure 3.6), two cases have been simulated: low and high flow cases. Figure 3.8 shows the conceptual image of cesium transport in low and high river discharge conditions. We assumed that land erosion occurs only during heavy rainfall events. Therefore, the boundary conditions were different between these two cases. In the low flow case, dissolved cesium of  $1000 \text{ Bq/m}^3$  was applied to the upper dam boundary (the applied concentration was assumed from the monitoring data in JAEA 2013b). No sediment and cesium were supplied from overland/catchments. In the high flow case, on the other hand, the discharges of sediment and cesium from overland/catchments that were estimated with the Universal Soil Loss Equation (USLE)-based model (Yamaguchi et al. 2013) were applied as boundary conditions and lateral inflows (Figure 3.9).

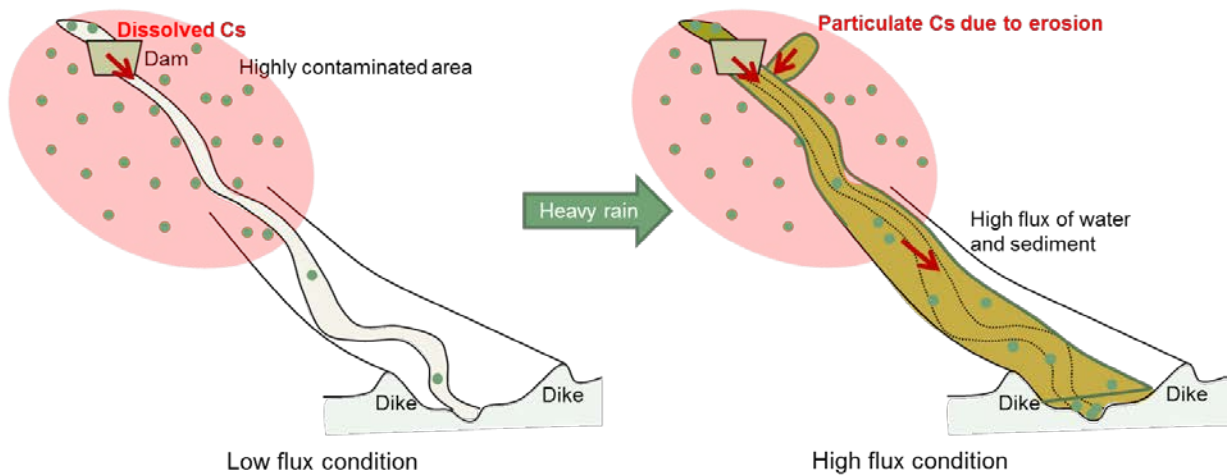


**Figure 3.8.** Conceptual Image of Cesium Transport in the Ukedo River in Low and High River Discharge Conditions

Model geometry (the elevation of the riverbed and the river width) is shown in Figure 3.10 and Figure 3.11. The parameter values such as distribution coefficient and critical stresses for suspension and deposition are shown in Table 3.1.

As stated previously, flow conditions were calculated by the CHARIMA model (Holly et al. 1990) (see the appendix). The flow rates shown in Figure 3.6 were applied to the nodes as boundary conditions for the low flow case. In the high flow case, flow rates 15 times as large as those in the low case were applied. This represents a heavy rainfall event such as the rain from the typhoon in September 2011 (the precipitation was about 230 mm).

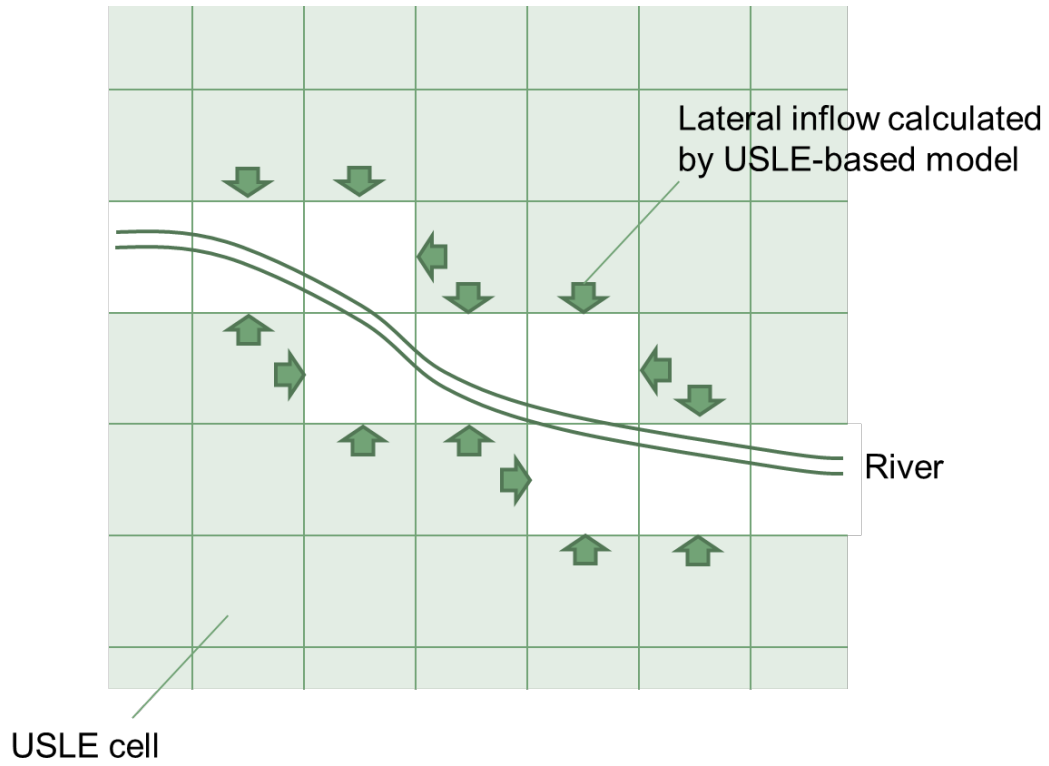


**Figure 3.9.** The USLE Grid and Lateral Inflow Applied to the River Model

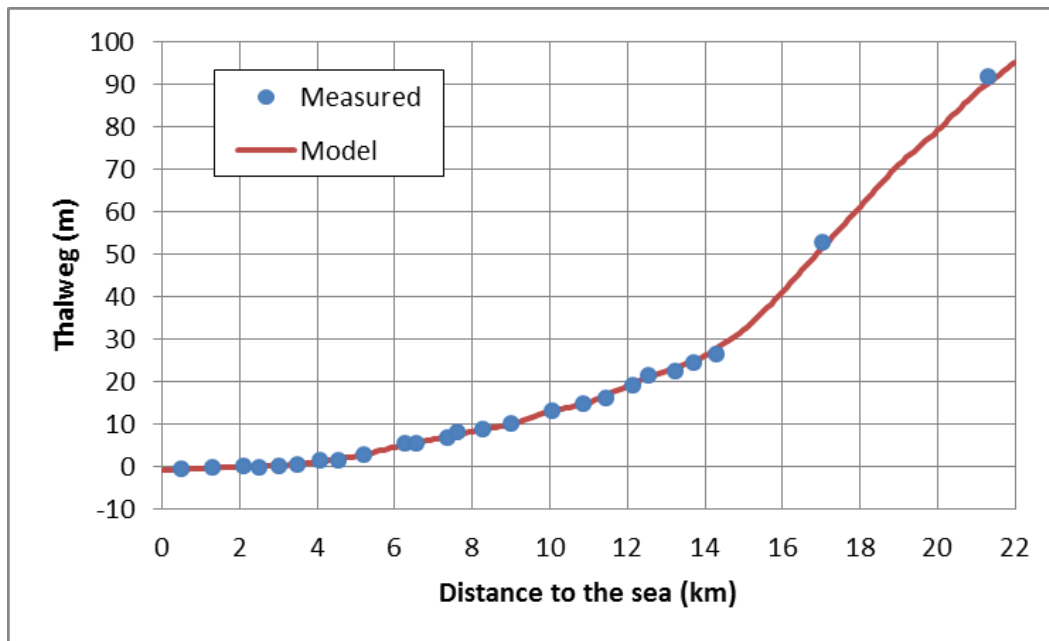


**Figure 3.10.** Elevation of the Riverbed (thalweg)

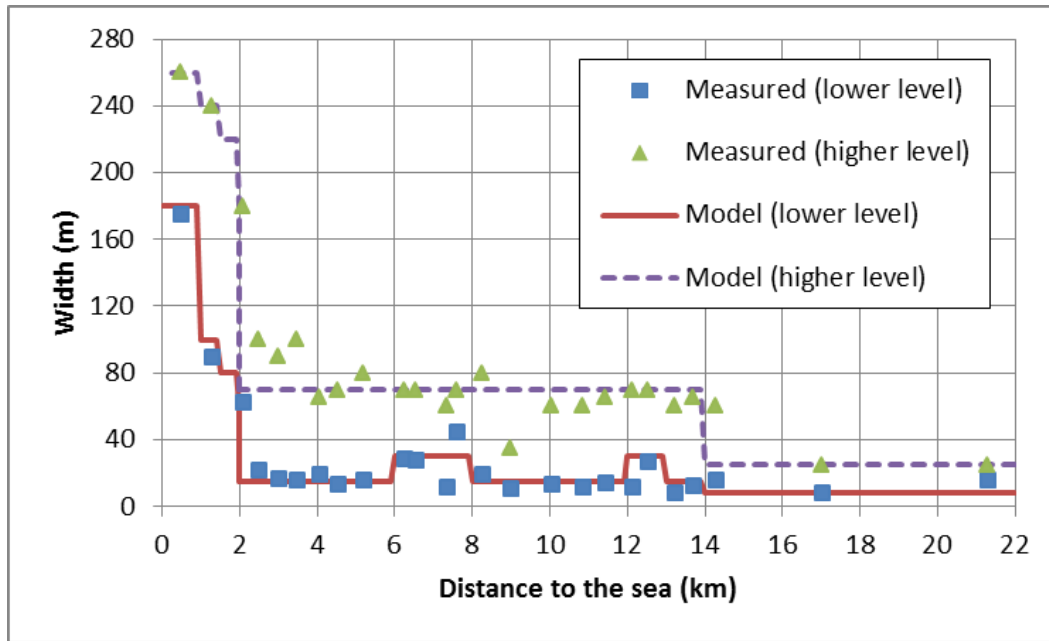


**Figure 3.11.** Longitudinal Distribution of the River Widths under Low and High Flow Conditions

**Table 3.1.** Parameters Used in the Low and High Flow Simulations

Parameters	Values	Basis
Manning's roughness coefficient	0.05 at $x < 14$ km 0.1 at $x \geq 14$ km	Estimated from the photographs
Mass fraction ratio	Sand:Silt:Clay = 2:2:1	Estimated from the literature (Yamaguchi et al. 2013)
Sand transport model	Toffaletti	Vanoni (1975)
Critical shear stress for resuspension	Silt: 2.94 Pa Clay: 4.9 Pa	Estimated from investigation data (JAEA 2013a, 2013b)
Critical shear stress for deposition	Silt: $9.8E-5$ Pa Clay: $9.8E-5$ Pa	Estimated from investigation data (JAEA 2013a, 2013b)
Armoring factor	Sand: 0.002 at $x < 14$ km, 0 at $x > 14$ km Silt and Clay: 0.002	Estimated from investigation data (JAEA 2013a, 2013b)
Erodibility	$4E-6$ kg/m <sup>2</sup> /s	Teeter (1988)
Dispersion coefficient	Estimated from the IAEA's equation	International Atomic Energy Agency (2001)
Distribution coefficient	Sand: $0.68$ m <sup>3</sup> /kg Silt: $4.5$ m <sup>3</sup> /kg Clay: $22.9$ m <sup>3</sup> /kg	Estimated from the literature (Yamaguchi et al. 2013)
Mass transfer rate for dissolved contaminant adsorption to and desorption from suspended sediment	$1E-5$ /s	Assumed
Mass transfer rate for dissolved contaminant adsorption to and desorption from bed sediment	$5E-7$ /s	Assumed

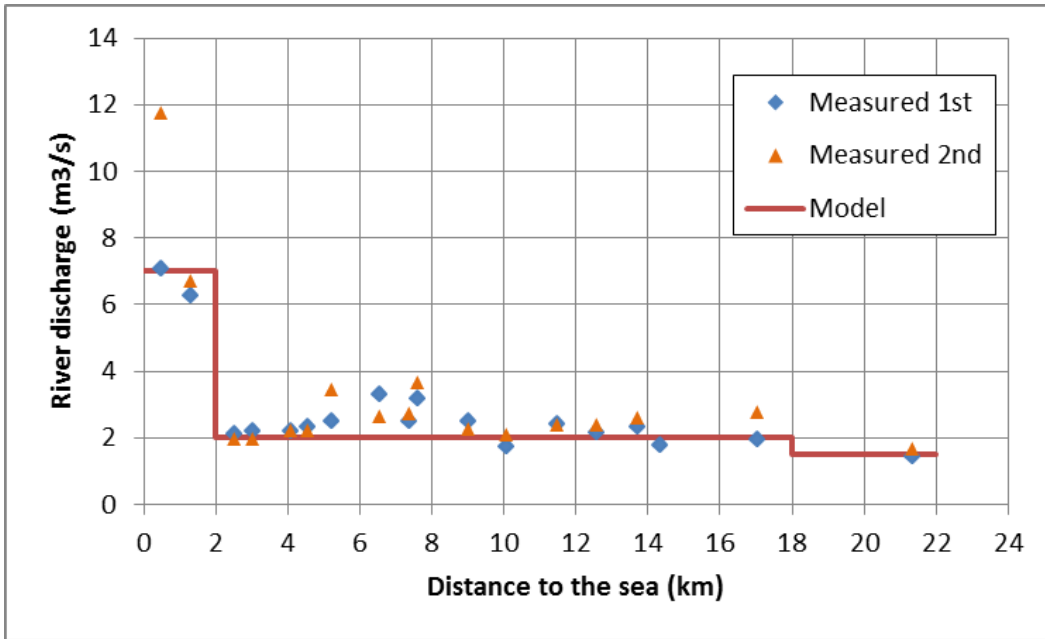
**Table 3.1. (contd)**

Parameters	Values	Basis
Initial bed layer thickness	0.27 m	Assumed
Initial bed contamination	No	Assumed
Initial concentration of suspended sediment	0 kg/m <sup>3</sup>	Assumed
Initial concentration of cesium in water column	0 Bq/kg	Assumed
Settling velocity	Silt: 2.0E-4 m/s Clay: 9.0E-7 m/s	Estimated
Density of sediment	2,650 kg/m <sup>3</sup>	Assumed
Simulation time	Low Flow: 4,000 h High Flow: 40 h	Assumed

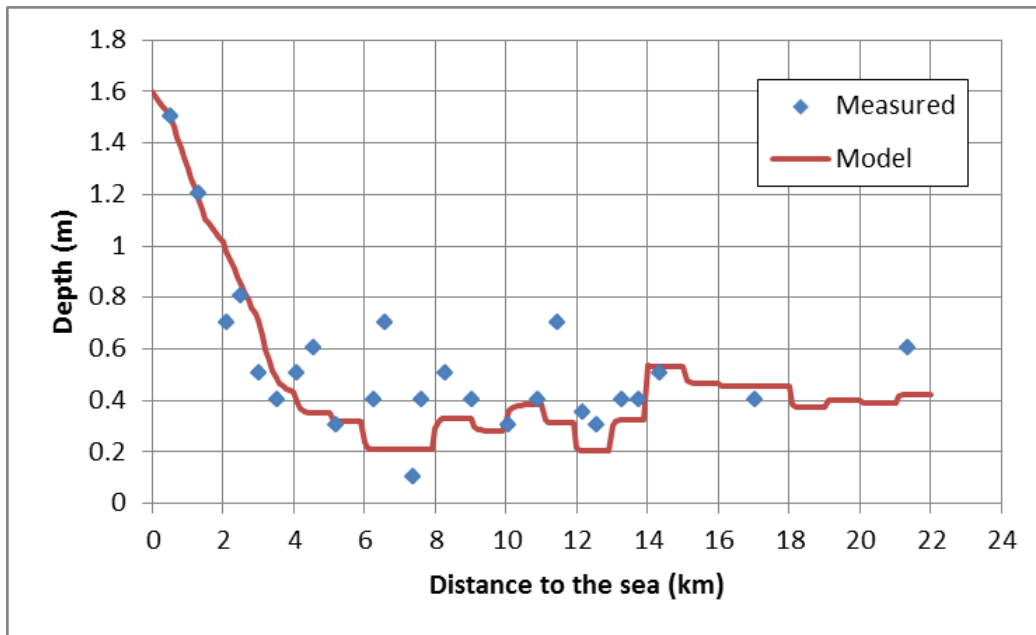
### 3.2.2 Simulation Results

#### 3.2.2.1 Low River Discharge Conditions

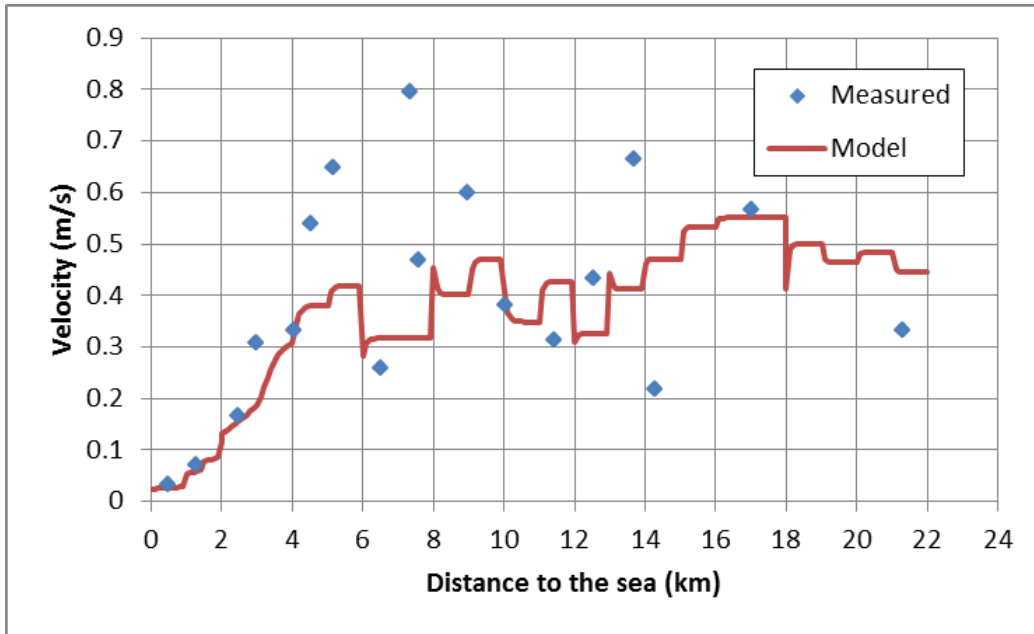
Figure 3.12, Figure 3.13, and Figure 3.14 show the longitudinal distributions of the river discharge rate, the depth, and the velocity, respectively, as the results of the flow simulation by CHARIMA. The river discharge rate increased at 2 km and at 18 km from the river mouth due to the inflows from the tributaries. After the Takase River merged at 2 km, the velocity decreased. This was due to the increases of both the depth and the width shown in Figure 3.11 and Figure 3.13. The simulation results were almost consistent with the measured values. The discrepancy of the simulated and measured flow rates between River kilometers 5 and 9 can be considered errors in measurements, because the both predicted water depth and velocity are lower than measured values, and river discharge rate is not constant (the mass balance is not confirmed) over this river reach, despite the absence of inflow to/outflow from the Ukedo River in this river reach.



**Figure 3.12.** Distribution of the River Discharge Rate during Low River Discharge

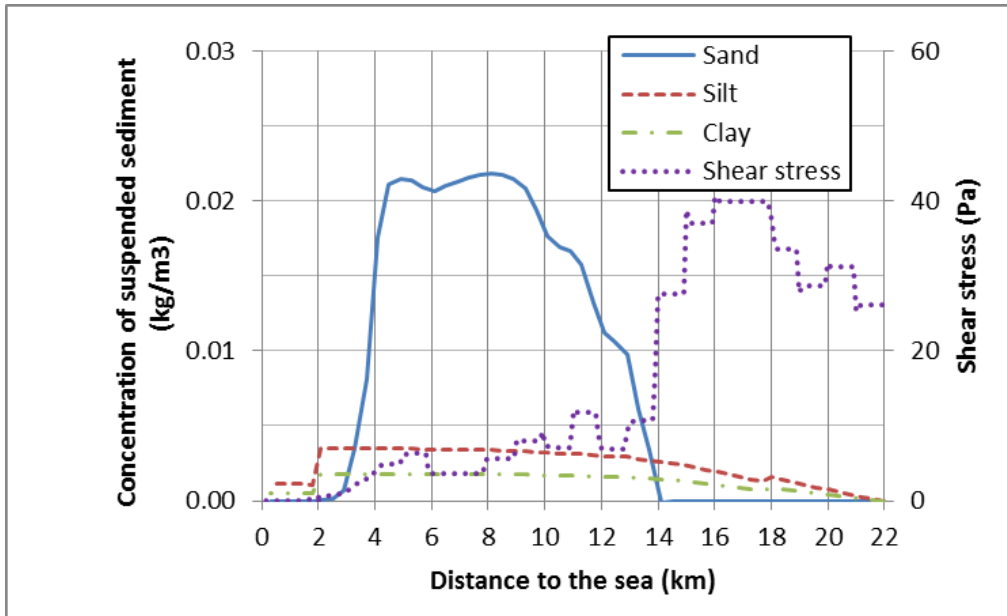


**Figure 3.13.** Distribution of the River Depth during Low River Discharge



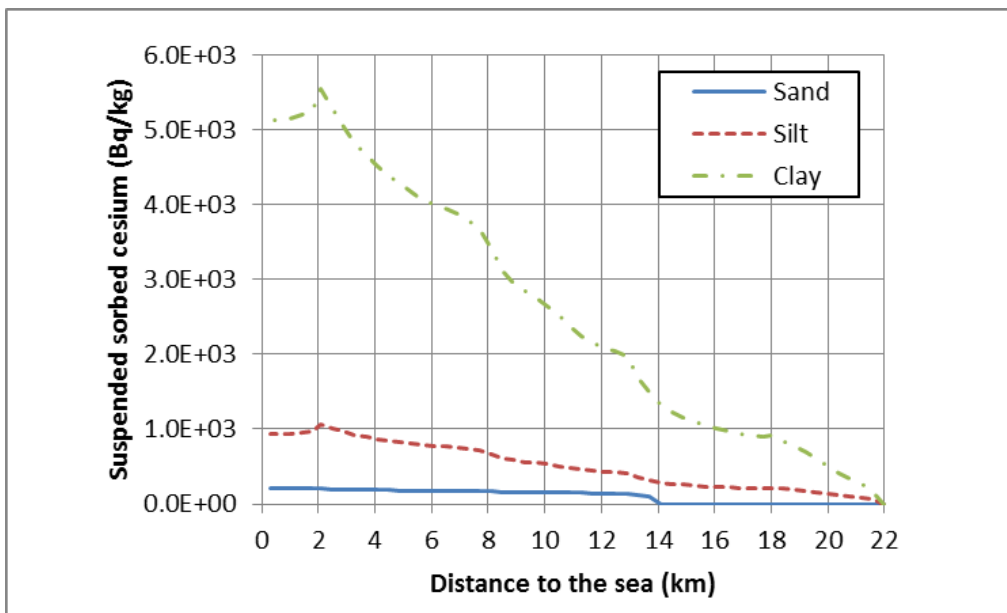
**Figure 3.14.** Distribution of the River Velocity during Low River Discharge

Figure 3.15 represents the spatial distributions of suspended sediment concentrations. As seen in the figure, the concentrations of suspended silt and clay gradually increased in the flow. This was due to the resuspension of sediments from the riverbed. Decreases at 2 km and 18 km were due to dilution by the inflow of water with no suspended sediment from the tributaries. On the other hand, the concentration of suspended sand increased around 9 km to 14 km and decreased around 3 km to 5 km from the sea. The concentrations of sediments correspond to the distribution of shear stress calculated by Equation (2.6). The concentrations tend to increase in areas where shear stress is high, while they tend to increase less or decrease in areas where shear stress is low. In the upstream of 14 km from the river mouth, no suspended sand can be seen. This is because the armoring factor was set to zero based on the photograph of the riverbed totally covered by rocks and bottom sediment larger than sand, thus no supply of sediment come from the river bottom in this area (Figure 3.2).



**Figure 3.15.** Spatial Distributions of Suspended Sediment Concentrations during Low River Discharge

Figure 3.16 and Figure 3.17 show the spatial distributions of sediment-sorbed cesium concentrations and total cesium concentrations in dissolved and particulate forms, respectively. It can be seen in the figures that dissolved cesium was gradually sorbed by suspended sediments and that silt and clay play more important roles in cesium migration than sand. This is because the cesium distribution coefficients with clay and silt are greater than that with sand.



**Figure 3.16.** Spatial Distributions of Sediment-Sorbed Cesium Concentrations during Low River Discharge

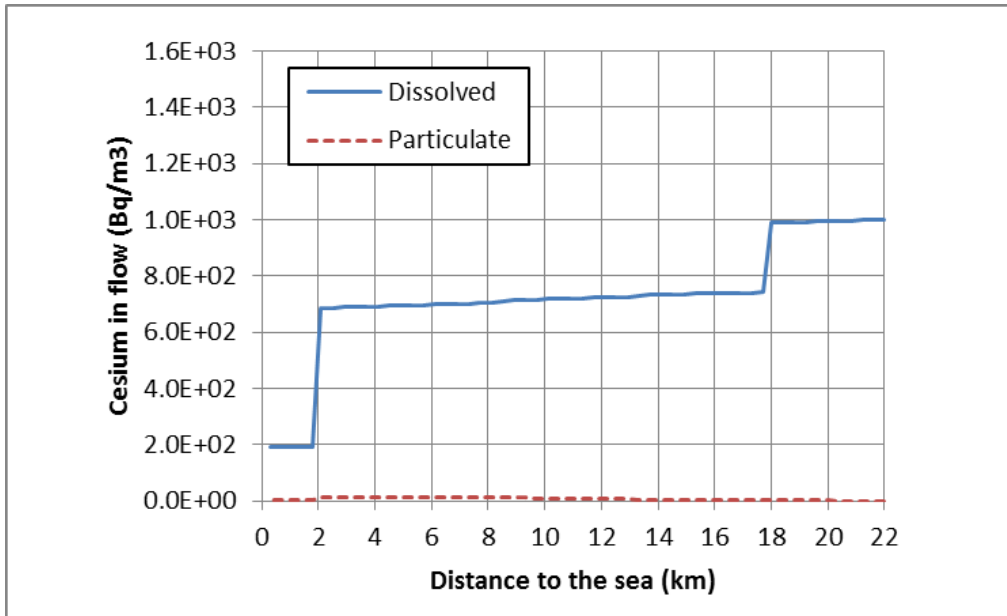


**Figure 3.17.** Spatial Distributions of the Total Cesium Concentrations in the Flow during Low River Discharge

The distributions of riverbed thickness and of cesium in the riverbed are shown in Figure 3.18 and Figure 3.19. The contamination peak can be seen from 2 km to 4 km from the river mouth and it is consistent with the peak of the bed thickness. Furthermore, it is the area where suspended sand drastically decreased (see Figure 3.15). This means that the bed contamination was caused mainly by deposition of contaminated sand.

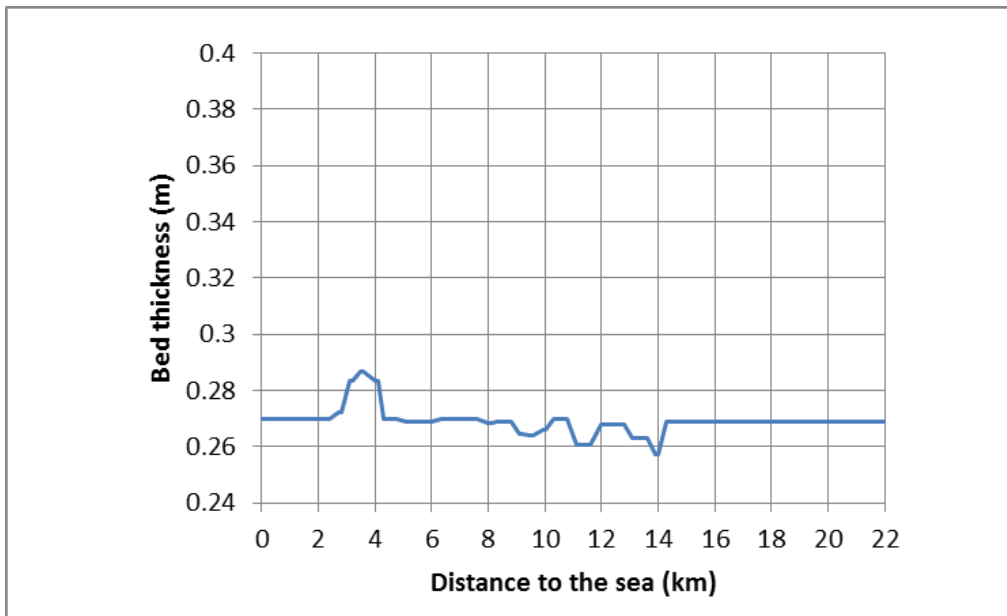


**Figure 3.18.** Distribution of the Bed Layer Thickness during Low River Discharge

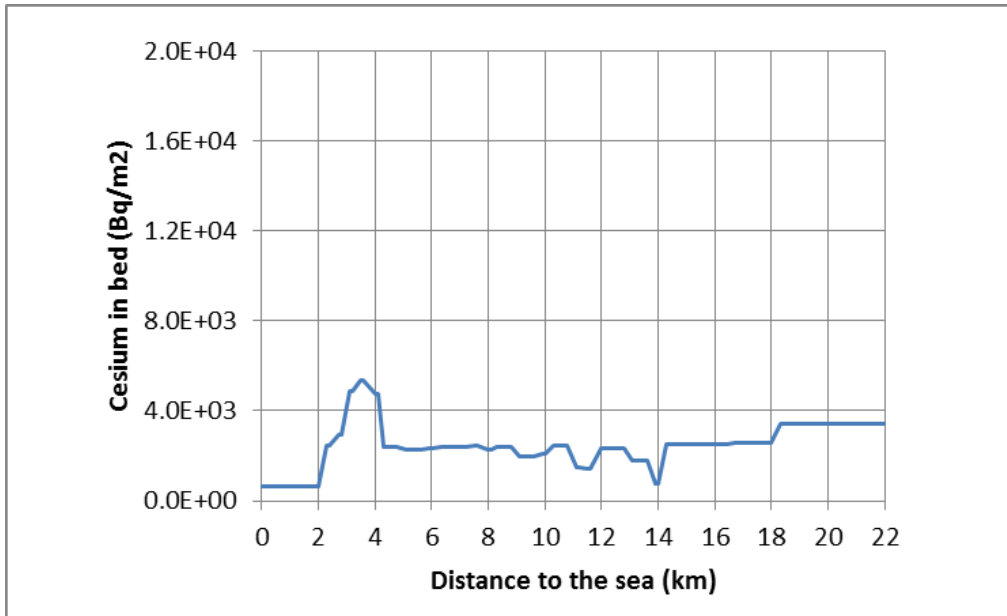


Figure 3.19. Distribution of Cesium in the Riverbed during Low River Discharge

### 3.2.2.2 High River Discharge Conditions

The results of the flow simulation in the high flow case are shown in Figure 3.20, Figure 3.21, and Figure 3.22. The figures also include the results of the low flow case described above. Measured data is not available for high river discharge conditions.

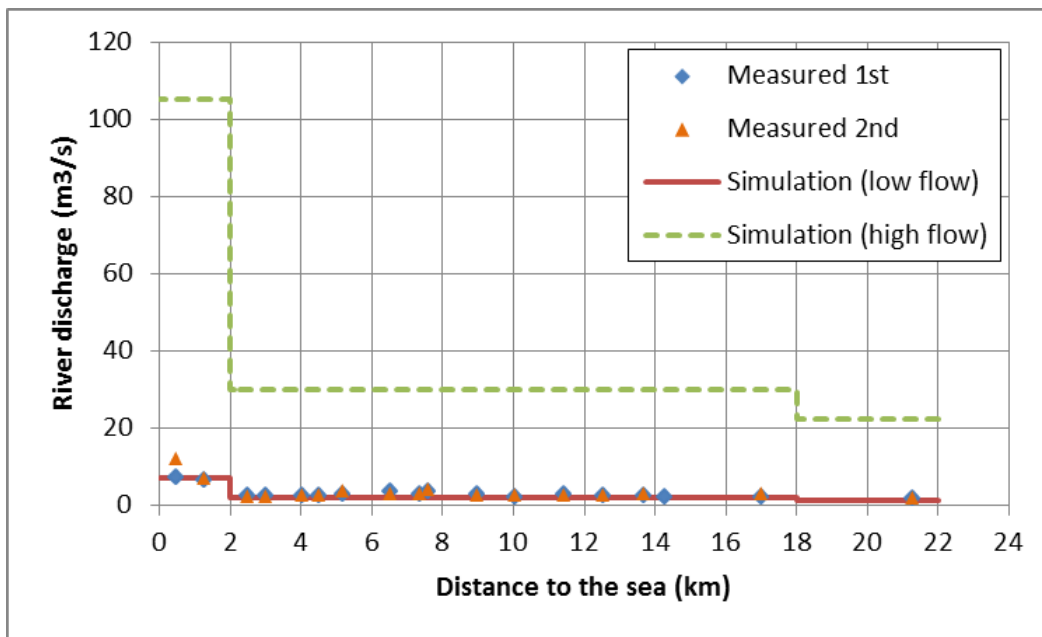
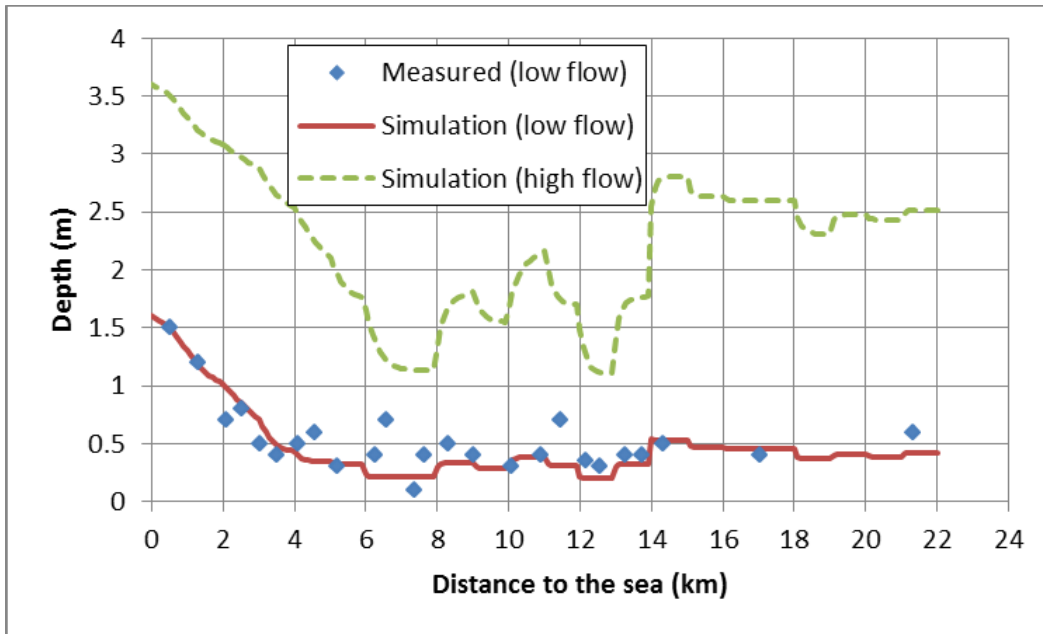
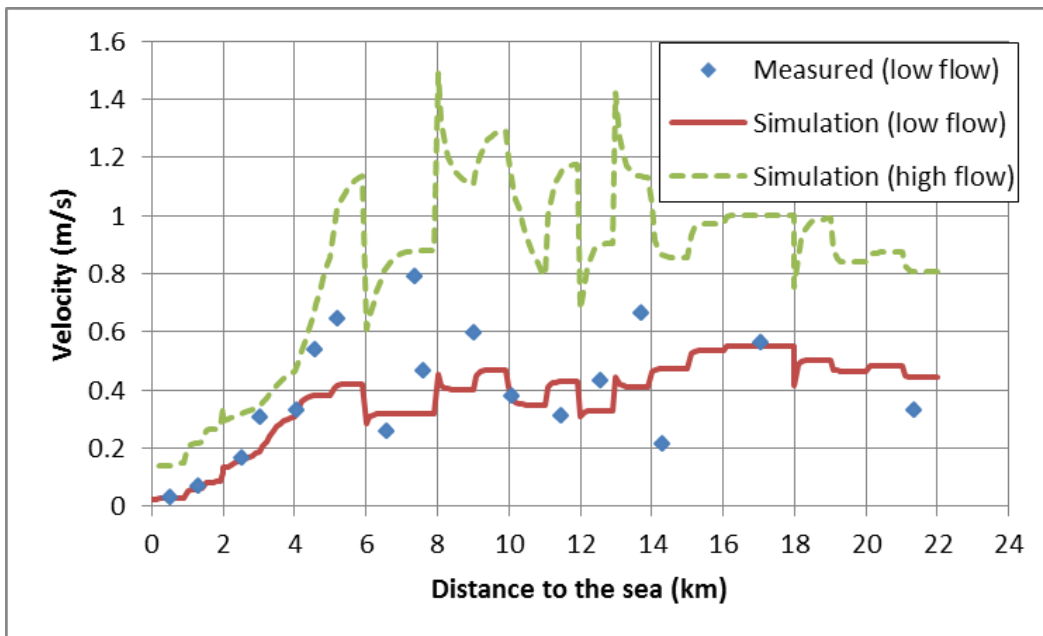


Figure 3.20. River Discharge Rate in the High Flow Case Compared with that in the Low Flow Case



**Figure 3.21.** Distributions of the Water Depth in the Low and High Flow Cases



**Figure 3.22.** Distributions of the Velocity in the Low and High Flow Cases

Figure 3.23 shows the distributions of suspended sediment concentrations. Since sediments were supplied as the upper dam boundary condition and as lateral inlfuxes based on the results of the USLE-based, SACT model (Yamaguchi et al. 2013), the concentrations of suspended sediments were much higher than those in the low flow case shown in Figure 3.15. Some amounts of suspended sediments originated in bed sediment but most amounts were attributed to sediment inlfuxes to the river due to overland erosion. Even in the high flow case, the concentration of suspended sand decreased near the

river mouth. This means that most of the suspended sand is deposited on the river bottom. Very little suspended silt and clay, on the other hand, are deposited in the river, even in low flow conditions.

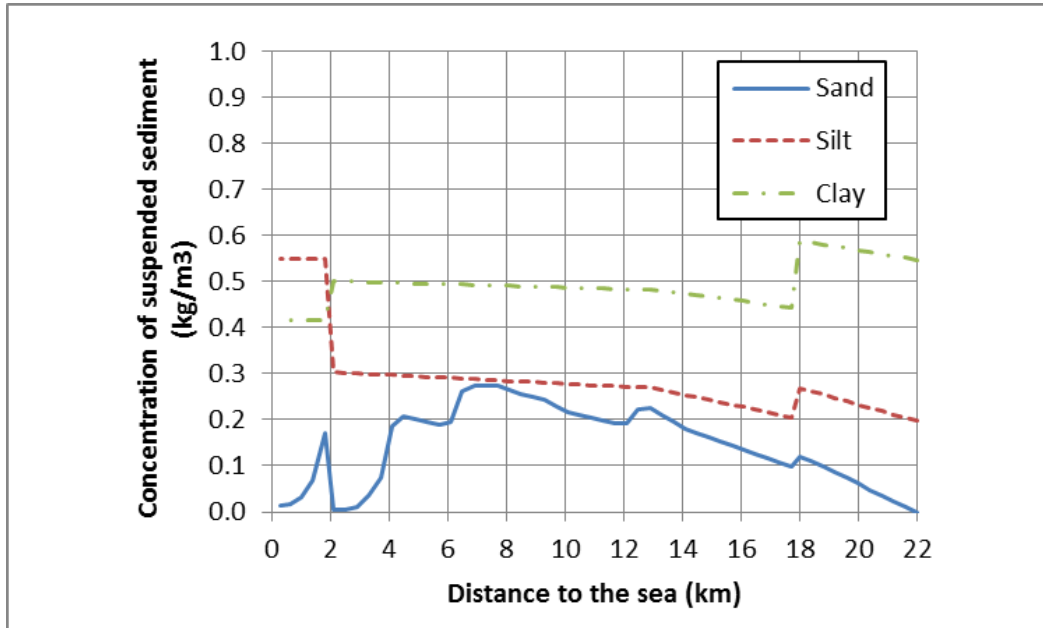


**Figure 3.23.** Distributions of Suspended Sediment Concentrations during High Flow Conditions

Figure 3.24 and Figure 3.25 present the distributions of cesium concentrations in dissolved and particulate forms. As shown in the figures, suspended sediments, especially silt and clay, were the main carriers of cesium, in contrast with the low flow case where a dissolved form was more important. In addition, the amount of cesium carried to the sea in the high river flow was much higher than that in the low river flow. The measured values of the concentrations of cesium shown in Figure 3.25 were from samples of the floodplain sediment. Because the water surface elevation during the high flow corresponds to the height of the floodplain, we assumed that the floodplain sediment represented suspended sediment in high river discharge conditions. Although we need grain size distributions of the measured samples to compare the measured values with the simulation results more accurately, the simulation results agreed fairly well with the measured values.

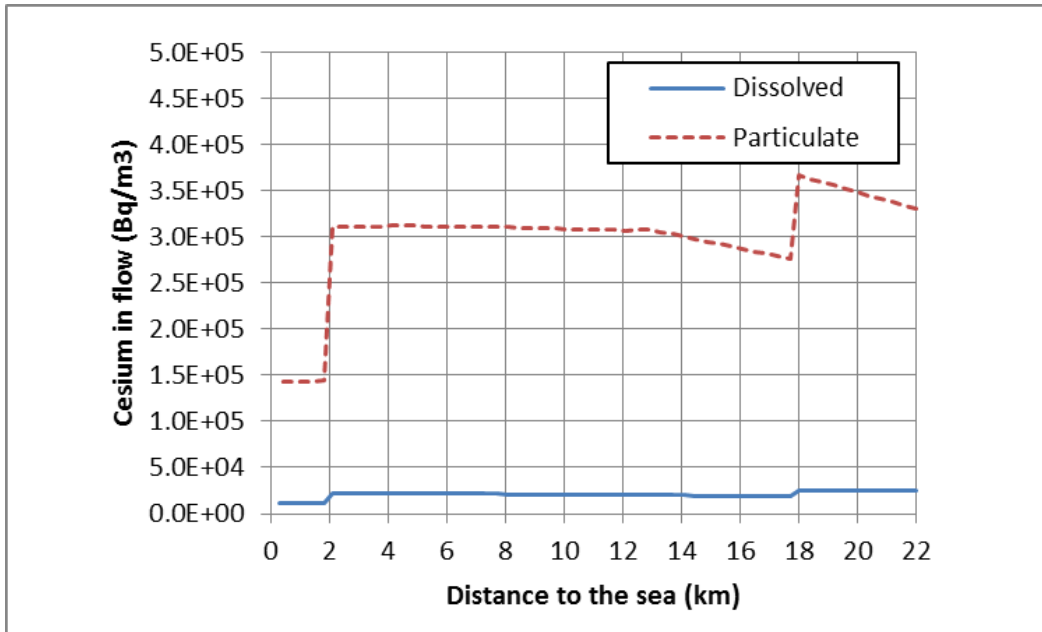


**Figure 3.24.** Distributions of the Total Cesium Concentrations in the Flow during High Flow Conditions

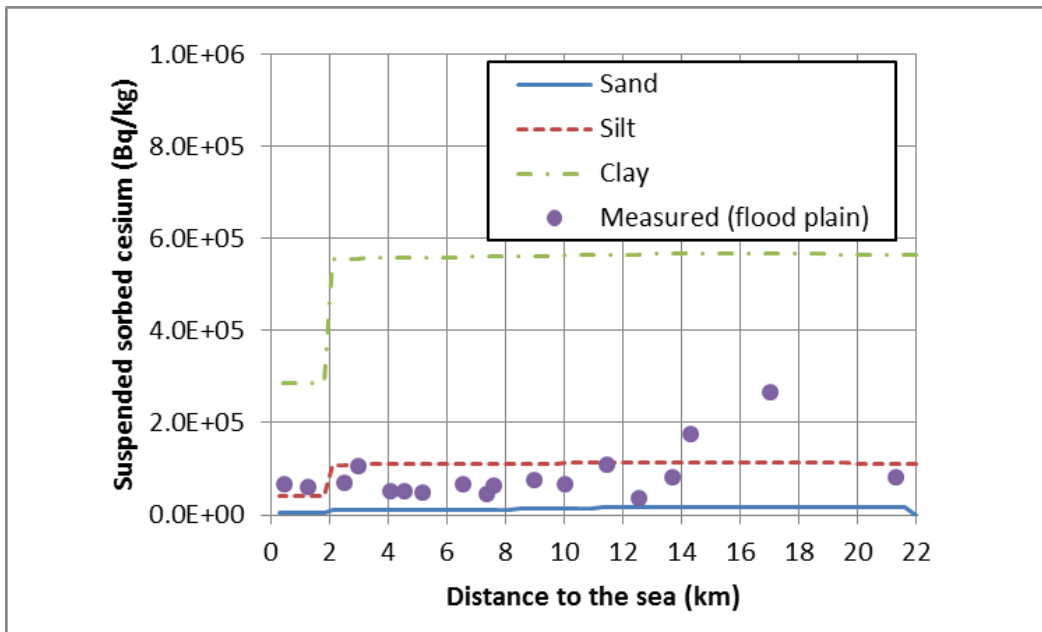


**Figure 3.25.** Distributions of Sediment-Sorbed Cesium Concentrations during High Flow Conditions

The bed conditions are shown in Figure 3.26 and Figure 3.27. The figures suggest that the bed contamination was due to deposition of contaminated sand as in the low flow case.

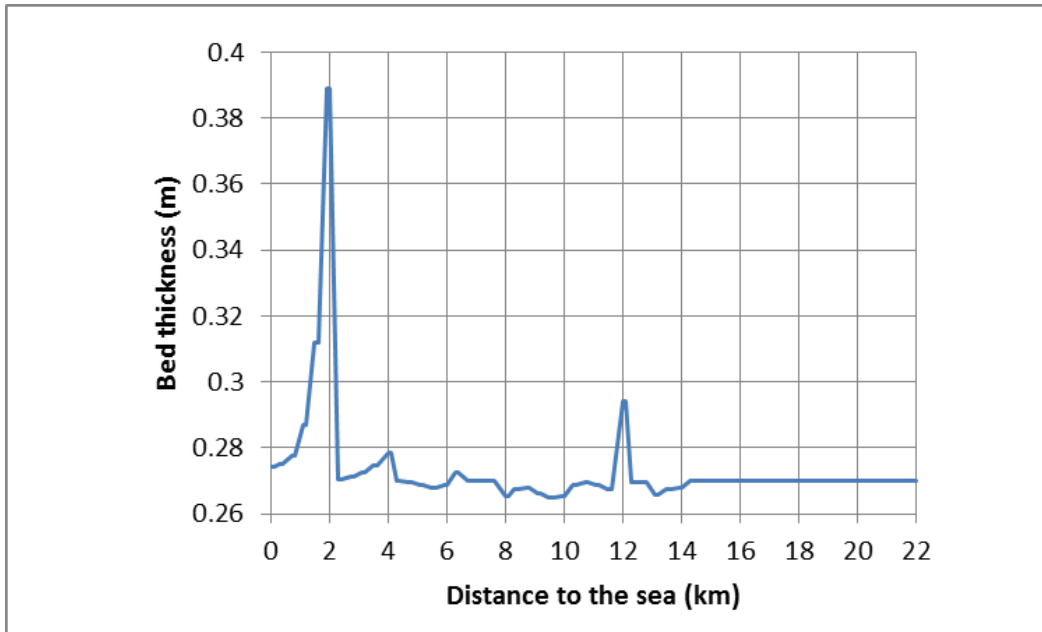


**Figure 3.26.** Distribution of the Bed Layer Thickness during High Flow Conditions

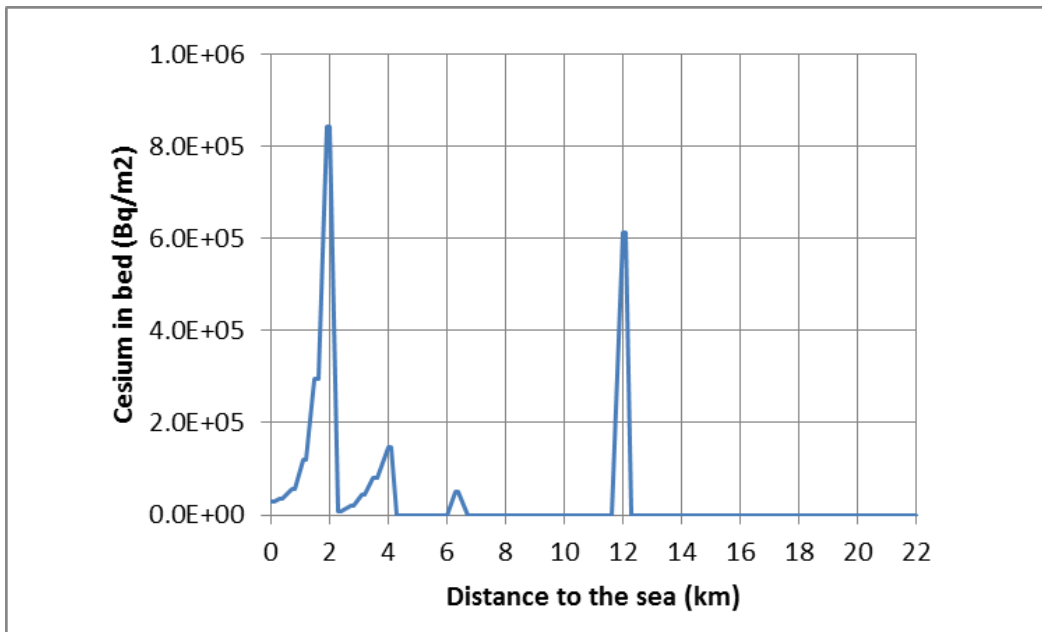


**Figure 3.27.** Distribution of the Cesium in the Riverbed during High Flow Conditions

### **3.3 Sequential Simulation during a Rainfall Event using the Ukedo Whole Model (UWM)**

#### **3.3.1 Analytical Conditions**

This section presents a sequential analysis of during and after heavy rainfall events by using the UWM (Figure 3.7). A high discharge rate was applied during the first 40 hours followed by a low discharge rate for a year; this cycle was repeated twice, for a total of three cycles. The purpose of the simulation was to examine the time dependencies of the transport behaviors of sediment and cesium during and after rainfall events.

The model geometry is shown in Figure 3.28 and Figure 3.29. Since the measured values were available only below 22 km, the model upstream of 22 km was developed according to the database published by the National and Regional Policy Bureau.<sup>1</sup> The Ogaki Dam reservoir extends from 22 km to 27 km from the river mouth.

The discharges of sediment and cesium from the USLE-based model, SACT were applied as lateral inflows for the first 40 hours of each cycle. After 40 hours, neither sediment nor cesium was supplied to the river.

The applied parameters are shown in Table 3.2. They are consistent with those used in the UPM. The flow rate is shown in Figure 3.7.

---

<sup>1</sup> National and Regional Policy Bureau (Ministry of Land, Infrastructure, Transport and Tourism). National Land Numerical Information. Accessed February 20, 2014 at <http://nlftp.mlit.go.jp/ksj-e/index.html>.

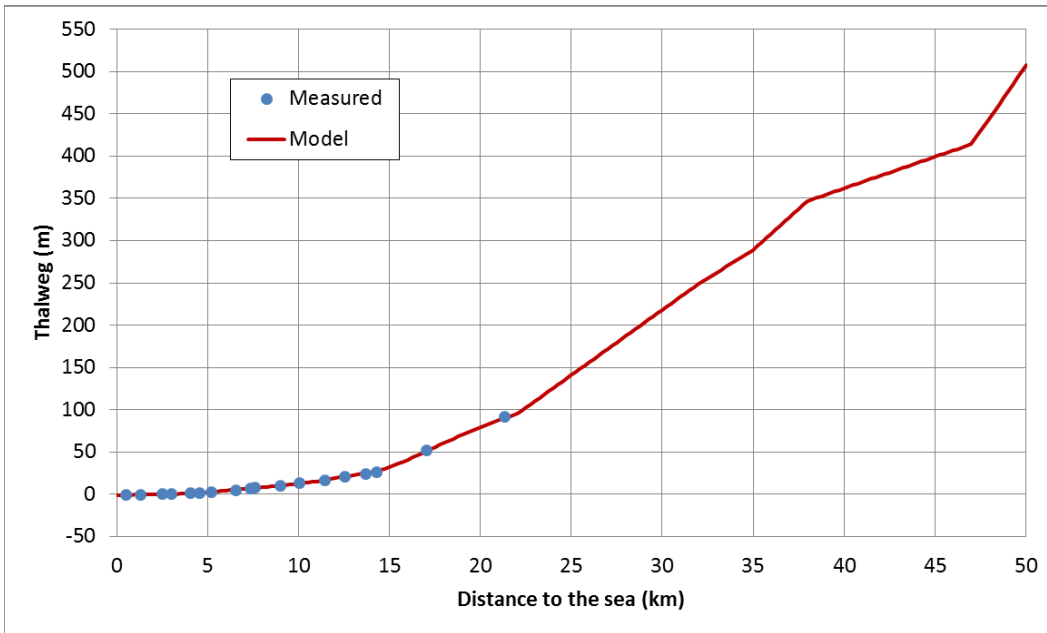


**Figure 3.28.** Elevation of the Riverbed along the Ukedo River

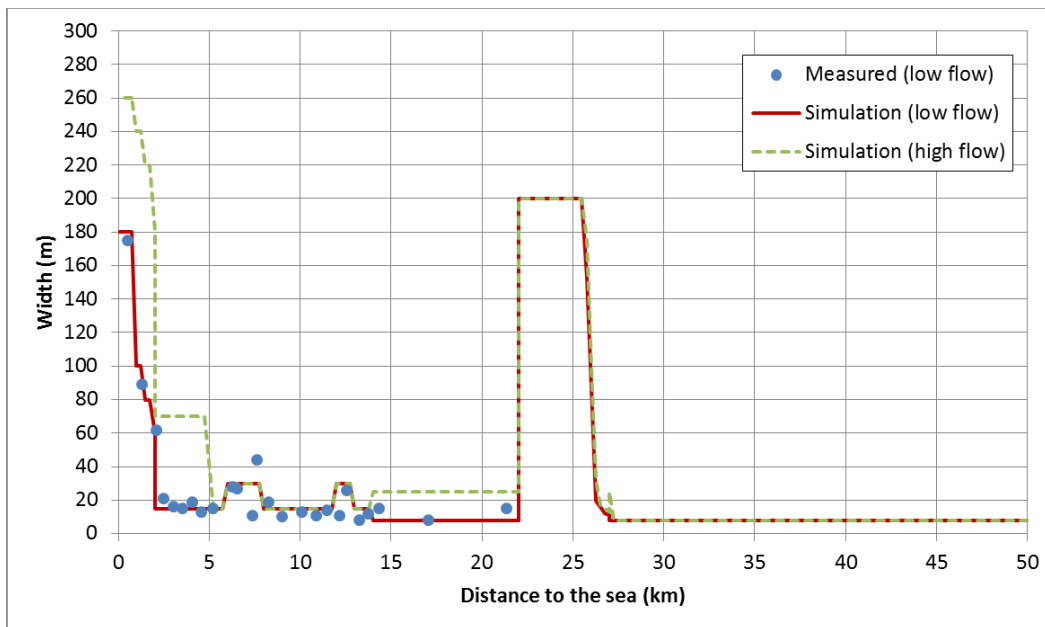


**Figure 3.29.** Distribution of the River Width along the Ukedo River

**Table 3.2.** Parameters Used in the Simulations during a Rainfall Event

Parameters	Values	Basis
Manning's roughness coefficient	Ukedo River: 0.05 at $x_a < 14$ km, 0.1 at $x_a > 14$ km Takase River: 0.05 at $x_b < 20$ km, 0.1 at $x_b > 20$ km ( $x_a$ and $x_b$ are the coordinates along the Ukedo River and the Takase River, respectively. See Figure 3.7)	Estimated from the photographs
Mass fraction ratio	Sand:Silt:Clay = 2:2:1	Estimated from the literature (Yamaguchi et al. 2013)
Sand transport model	Toffaletti	Vanoni (1975)
Critical shear stress for resuspension	Silt: 2.94 Pa Clay: 4.9 Pa	Estimated from investigation data (JAEA 2013a, 2013b)
Critical shear stress for deposition	Silt: $9.8E-5$ Pa Clay: $9.8E-5$ Pa	Estimated from investigation data (JAEA 2013a, 2013b)
Armoring factor	Ukedo River: Sand: 0.002 at $x_a < 14$ km, 0 at $x_a > 14$ km Silt and Clay: 0.002 The other rivers: 0.002	Estimated from investigation data (JAEA 2013a, 2013b)
Erodibility	$4E-6$ kg/m <sup>2</sup> /s	Teeter (1988)
Dispersion coefficient	Estimated from the IAEA's equation	International Atomic Energy Agency (2001)
Distribution coefficient	Sand: $0.68$ m <sup>3</sup> /kg Silt: $4.5$ m <sup>3</sup> /kg Clay: $22.9$ m <sup>3</sup> /kg	Estimated from the literature (Yamaguchi et al. 2013)
Mass transfer rate for dissolved contaminant adsorption to and desorption from suspended sediment	$1E-5$ /s	Assumed
Mass transfer rate for dissolved contaminant adsorption to and desorption from bed sediment	$5E-7$ /s	Assumed
Initial bed layer thickness	0.27 m	Assumed
Initial bed contamination	No	Assumed
Initial concentration of suspended sediment	0 kg/m <sup>3</sup>	Assumed
Initial concentration of cesium in water column	0 Bq/kg	Assumed
Settling velocity	Silt: $2.0E-4$ m/s Clay: $9.0E-7$ m/s	Estimated
Density of sediment	2650 kg/m <sup>3</sup>	Assumed
Simulation time	Three cycles of 40-hour high flow followed by one year of low flow	Assumed

### 3.3.2 Simulation Results

Figure 3.30, Figure 3.31, and Figure 3.32 show the distributions of the computed river discharge rates, the depth and the velocity, respectively, during and after the rainfall event along the Ukedo River obtained by CHARIMA. Here, the flow was assumed to be steady in each condition. In the dam reservoir between 22 km and 27 km, the velocity was extremely low.

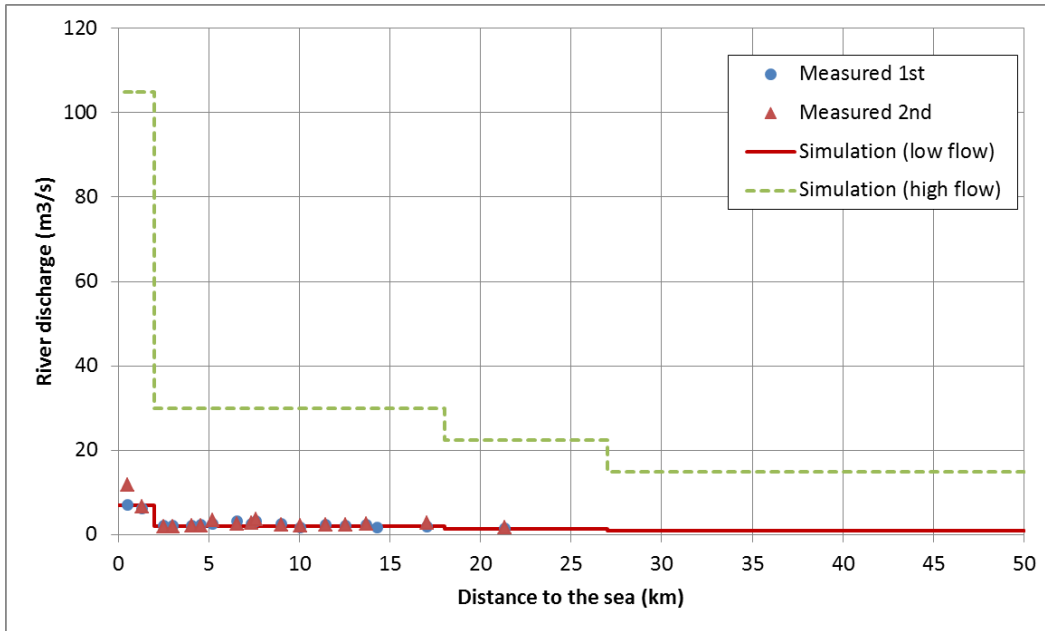


**Figure 3.30.** River Discharge Rate in the High Flow Condition during the Rainfall Event and in the Low Flow Condition after the Rainfall Event

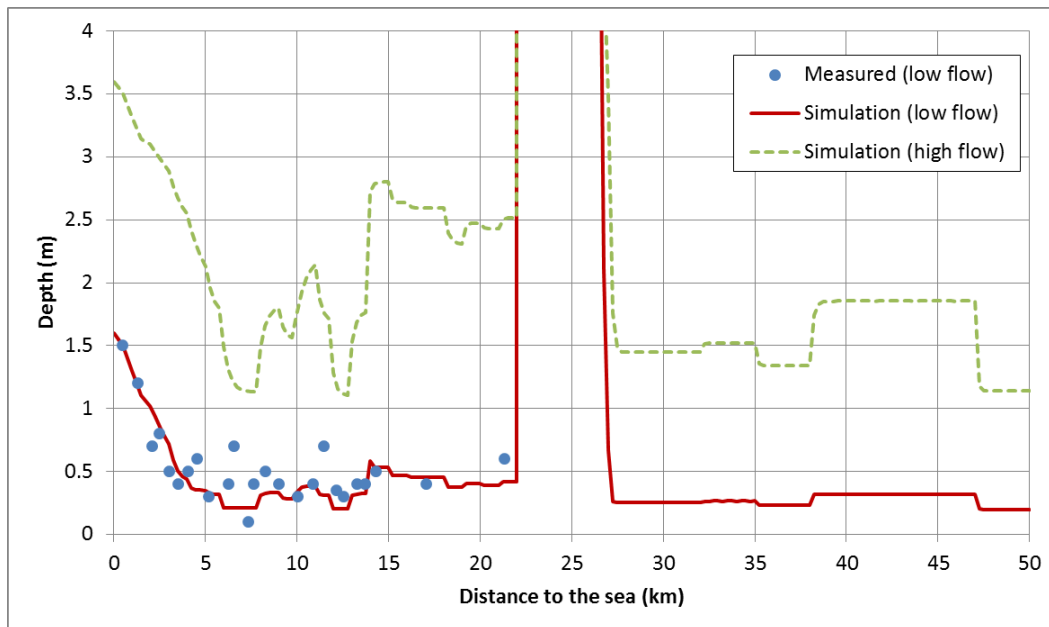


**Figure 3.31.** Distributions of Depth in the Low and the High River Discharge Conditions along the Ukedo River

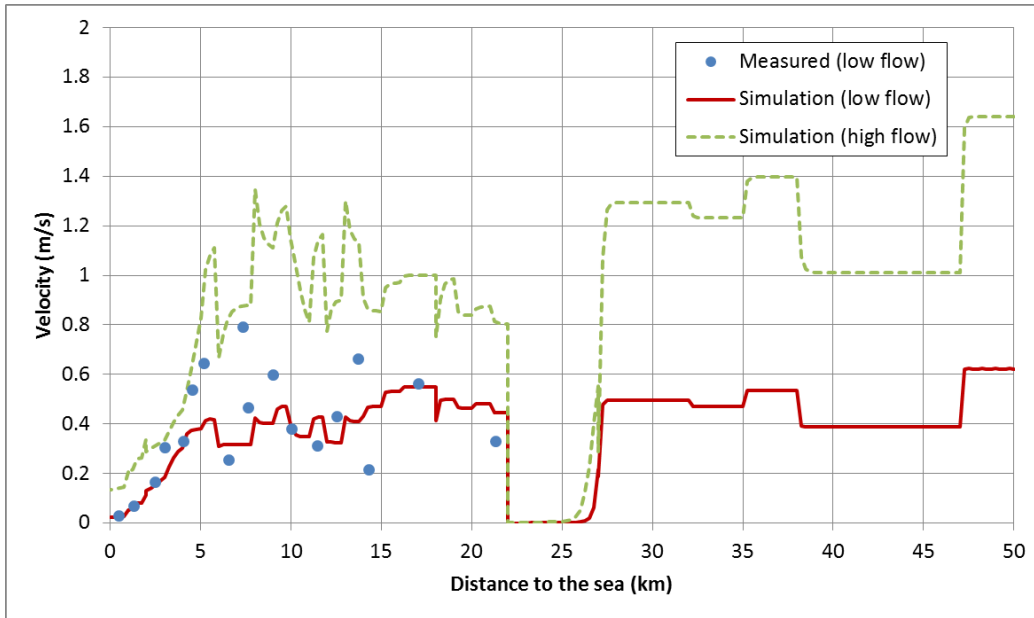


**Figure 3.32.** Distributions of Velocity in the Low and the High River Discharge Conditions along the Ukedo River

Figure 3.33, Figure 3.34, and Figure 3.35 show the distributions of computed concentrations of suspended sand, silt and clay, respectively, at 40 hours, 60 hours and 1,000 hours. Figure 3.36 focuses on the concentrations at 1000 hours. Suspended sand and silt deposited a short time after 40 hours, while some amount of suspended clay remained in water column even after 1,000 hours. It can be seen from Figure 3.36 that some amount of suspended clay in the reservoir reached the exit of the reservoir and affected the concentration below the dam. On the other hand, no influence of the high flow on the sand and silt concentrations at 1,000 hours can be seen.

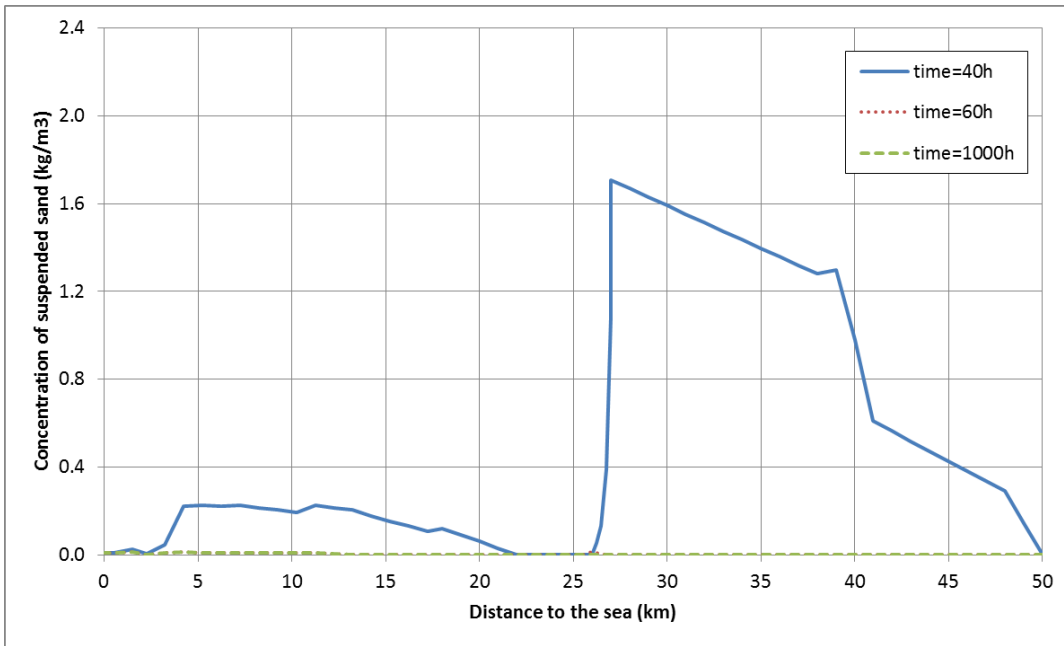


Figure 3.33. Distributions of Concentrations of Suspended Sand at 40 Hours, 60 Hours, and 1000 Hours

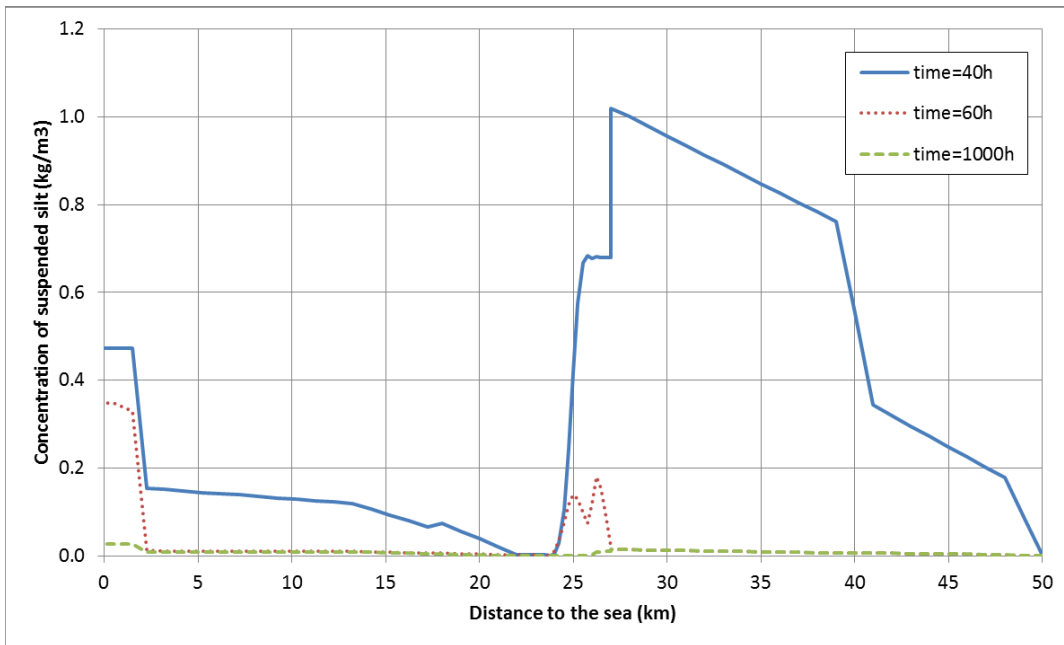
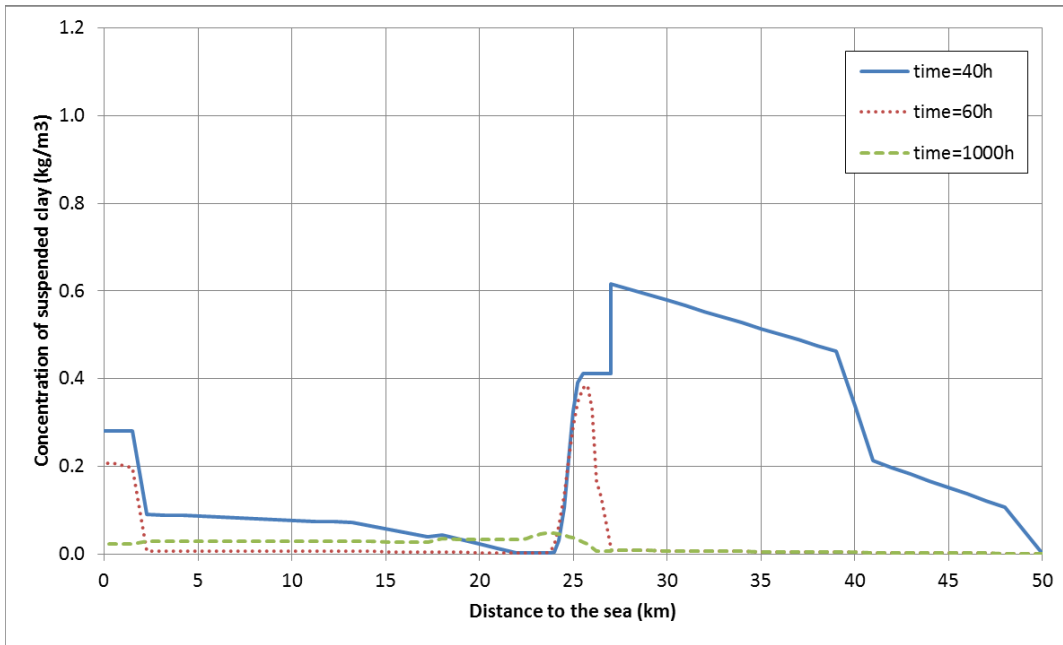
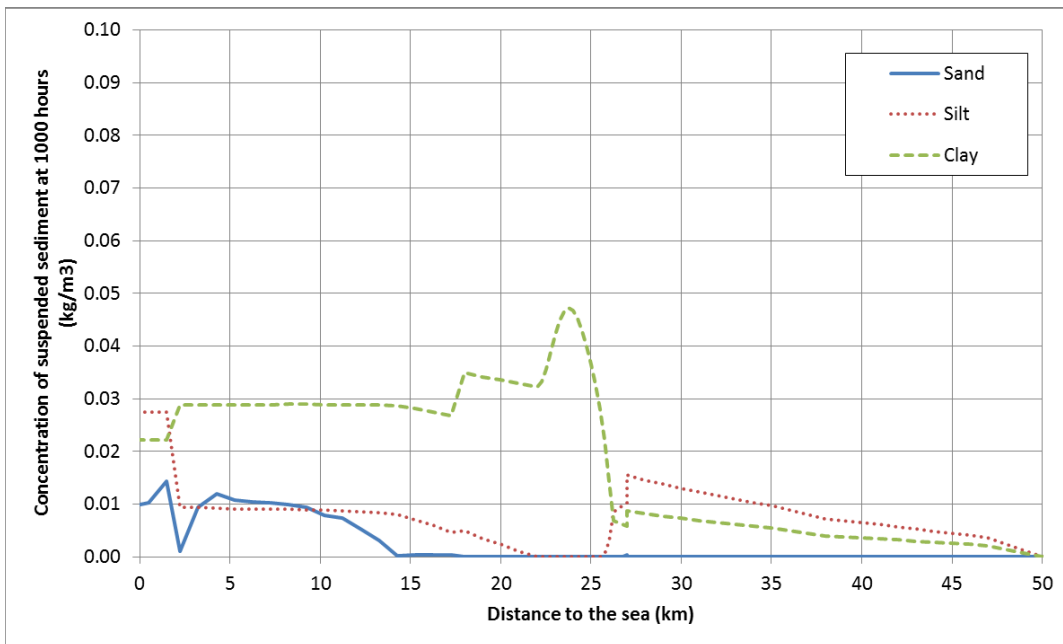


Figure 3.34. Distributions of Concentrations of Suspended Silt at 40 Hours, 60 Hours, and 1000 Hours

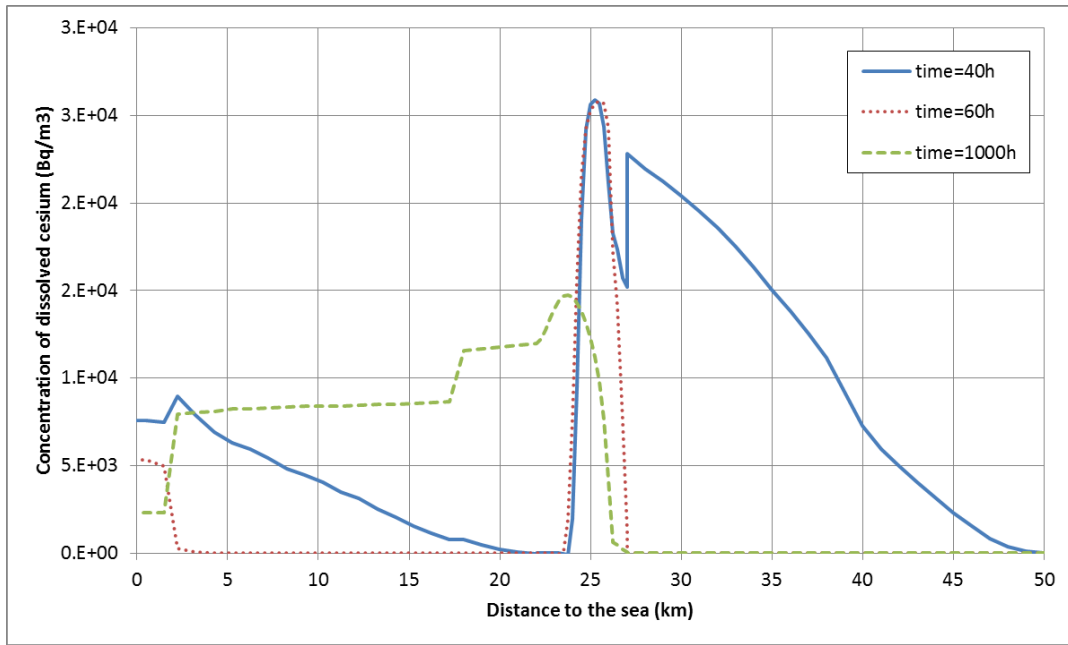


**Figure 3.35.** Distributions of Concentrations of Suspended Clay at 40 Hours, 60 Hours, and 1000 Hours

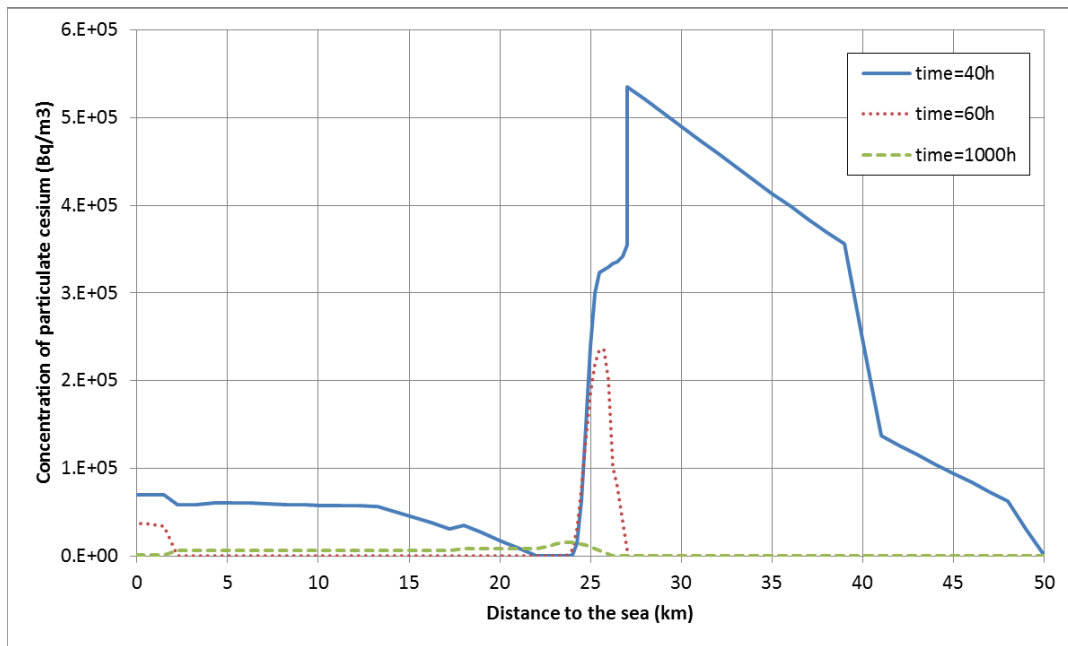


**Figure 3.36.** Distributions of Suspended Sediment Concentrations at 1000 Hours

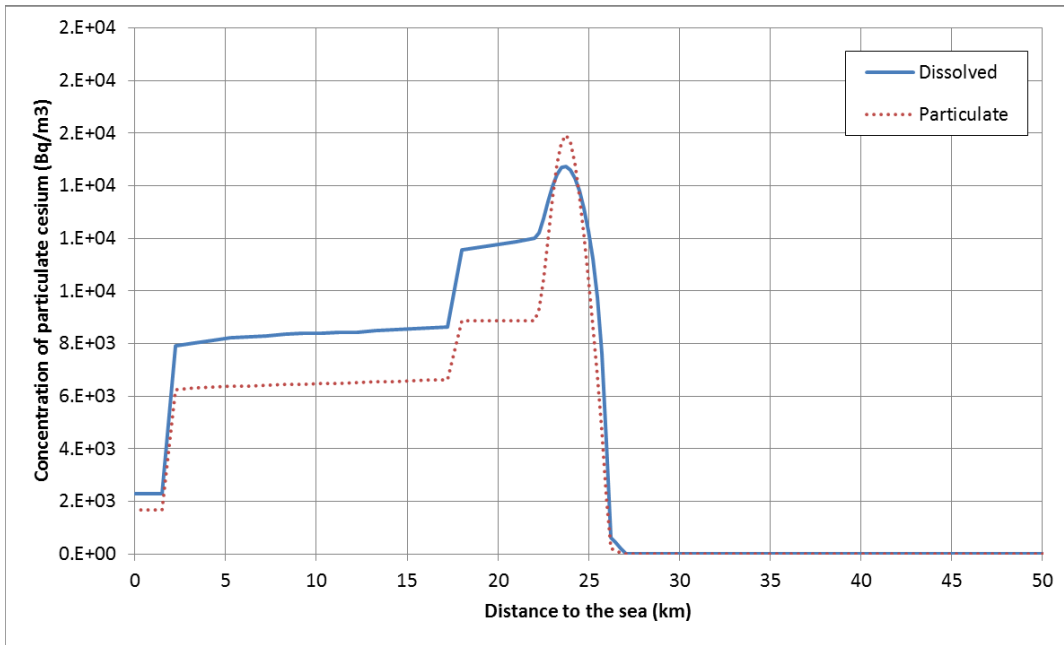
Figure 3.37 and Figure 3.38 show the distributions of computed dissolved and particulate cesium concentrations, respectively, and Figure 3.39 shows their distributions at 1,000 hours. Most of the cesium was prevented from moving beyond the dam by the reservoir, but some reached the exit in dissolved and clay-sorbed forms.



**Figure 3.37.** Distributions of Concentrations of Dissolved Cesium at 40 Hours, 60 Hours, and 1000 Hours

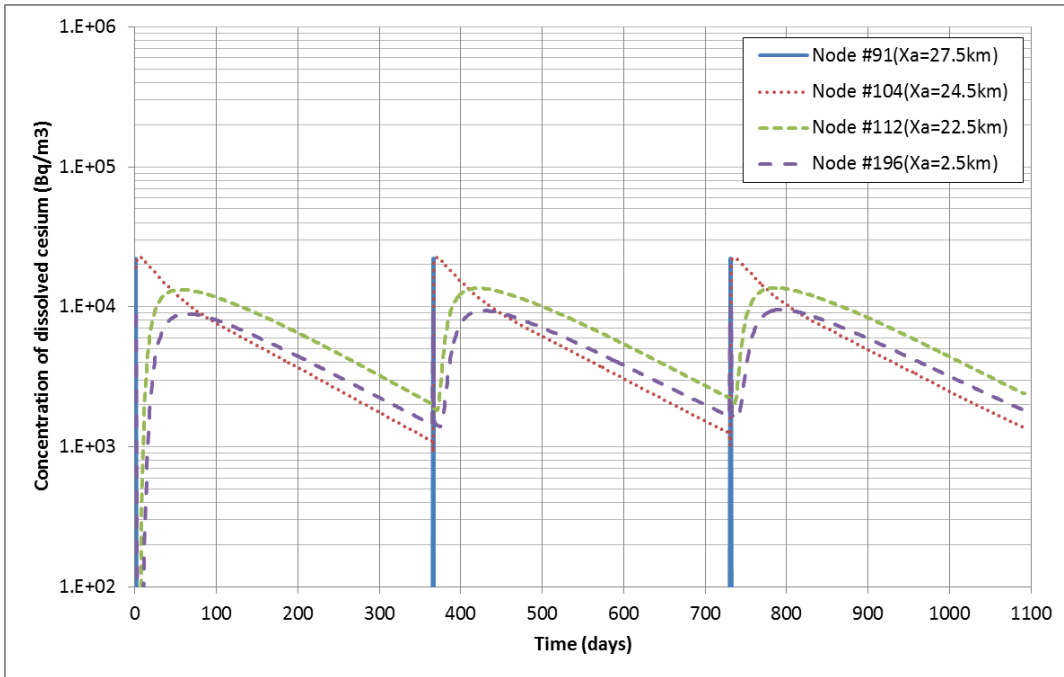


**Figure 3.38.** Distributions of Concentrations of Particulate Cesium at 40 Hours, 60 Hours, and 1000 Hours

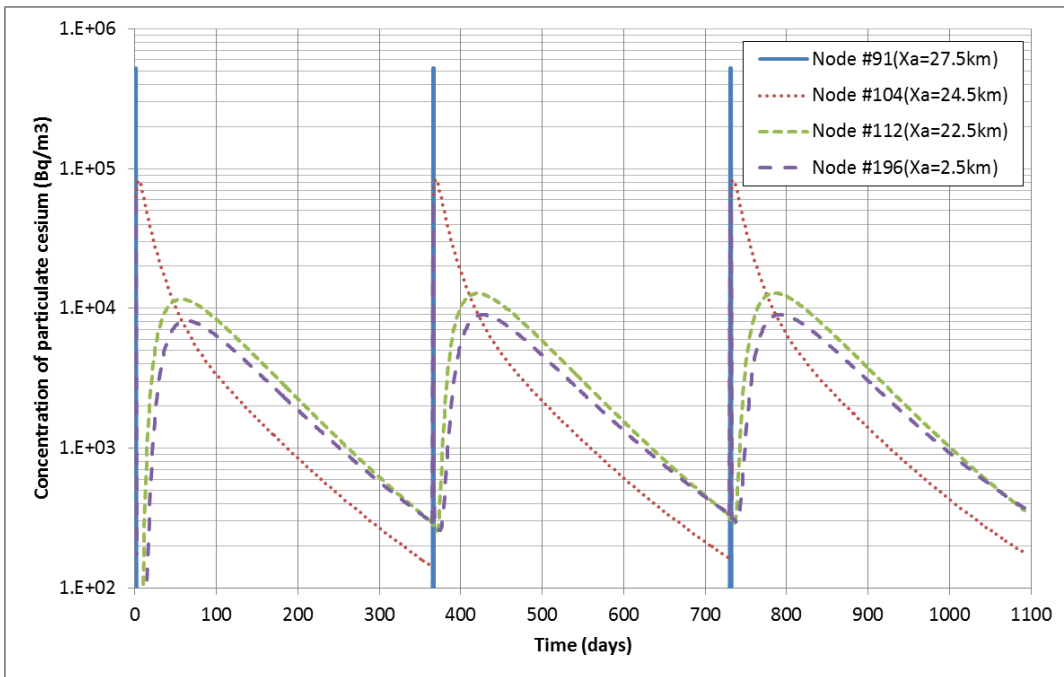


**Figure 3.39.** Distributions of Cesium Concentrations in the Flow at 1000 Hours

Figure 3.40 and Figure 3.41 show time histories of the predicted concentrations of dissolved and particulate cesium at Node #91 (near the entrance of the reservoir), #104 (the middle part of the reservoir), #112 (near the exit of the reservoir) and #196 (before the Takase River merges). The peaks in the downstream area were delayed and the contamination of water in the reservoir and in the river below the dam continued for months. This suggests that continuous monitoring is important to understand the effects of the reservoir on the cesium transport. In this simulation, the previous rainfall event did not affect the concentrations in the next cycle very much.



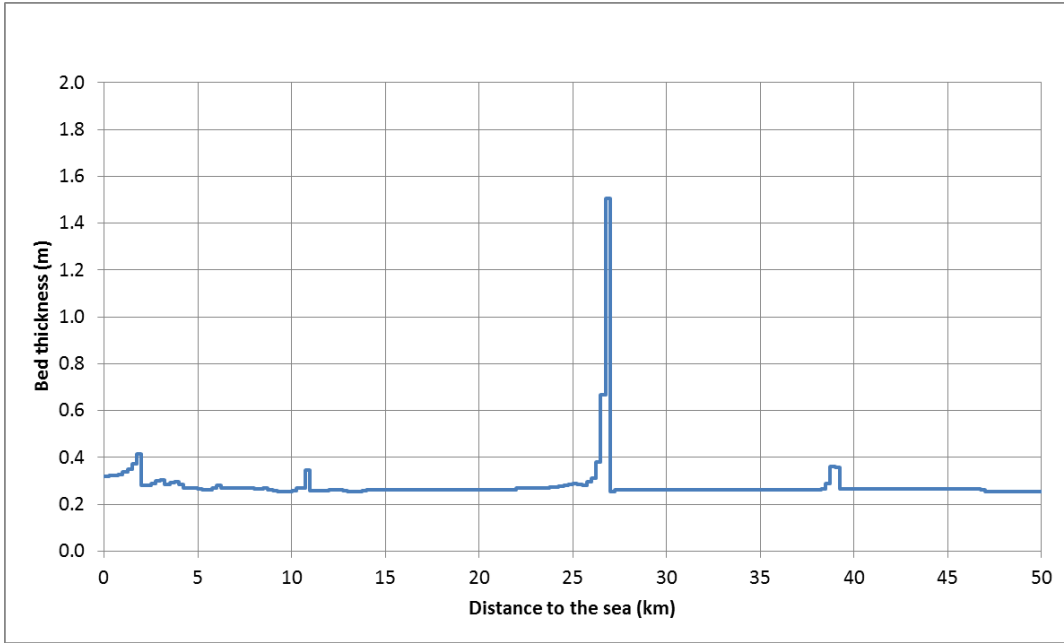
**Figure 3.40.** Time Histories of Concentrations of Dissolved Cesium



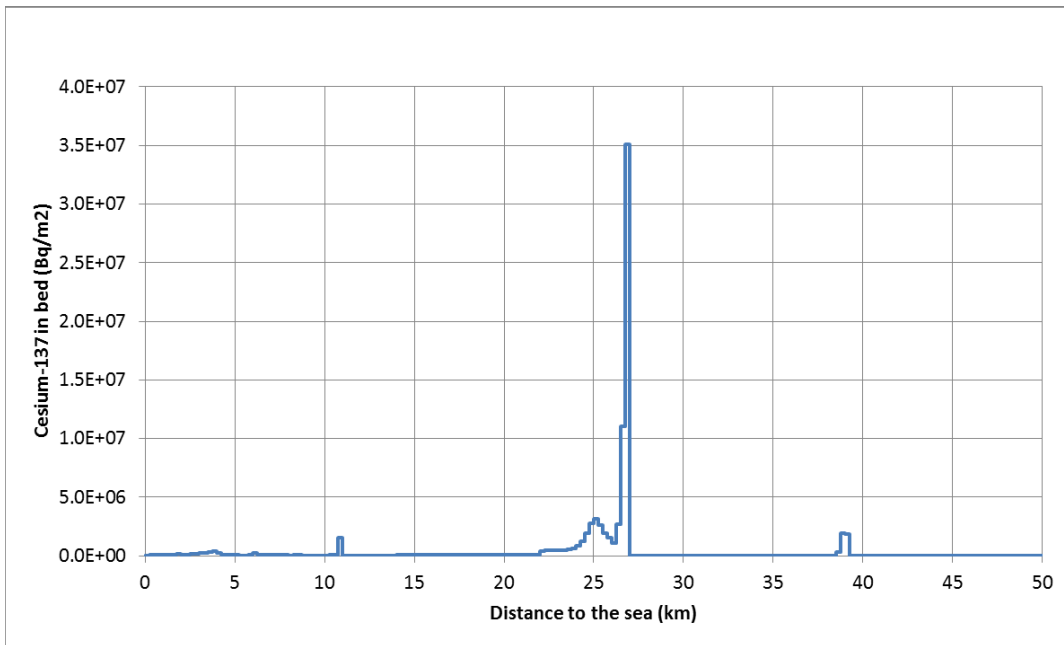
**Figure 3.41.** Time Histories of Concentrations of Particulate Cesium

Figure 3.42, Figure 3.43, and Figure 3.44 present the river bed conditions. It can be seen that deposition of sediment resulted in the contamination of the bed. In the reservoir, deposition of silt may be also important.

The sequential simulation suggests that the reservoir plays a role mainly as a sink of sediment and cesium, but some amounts of sediment and cesium pass through it.



**Figure 3.42.** Distribution of Riverbed Thickness



**Figure 3.43.** Distribution of Riverbed Contamination

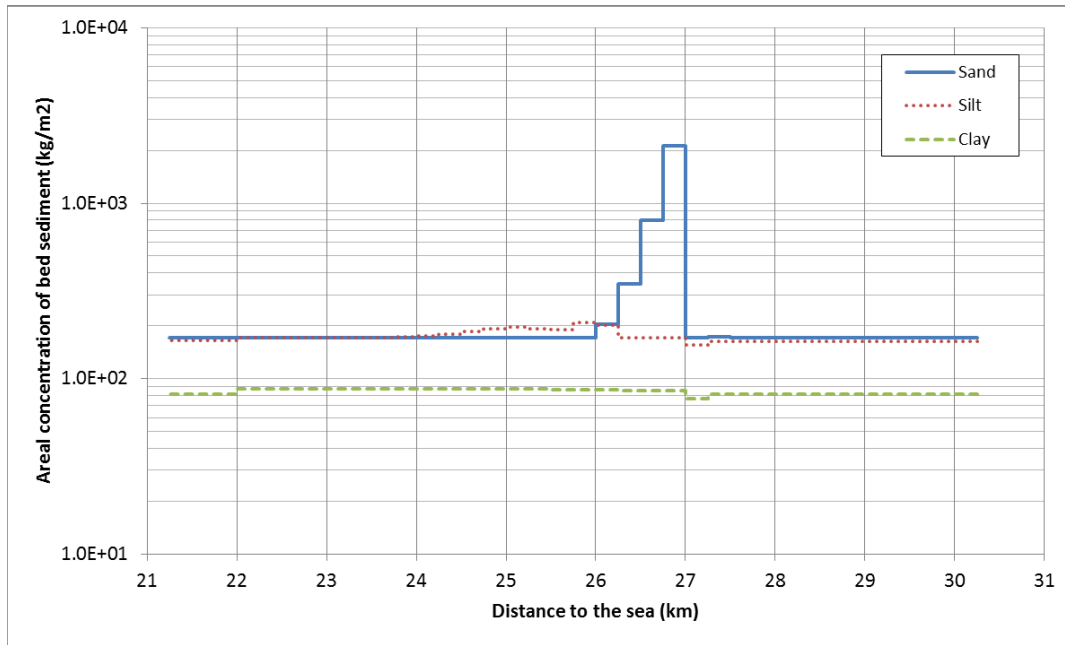


**Figure 3.44.** Distribution of Sediments in the Bed of the Ogaki Dam Reservoir

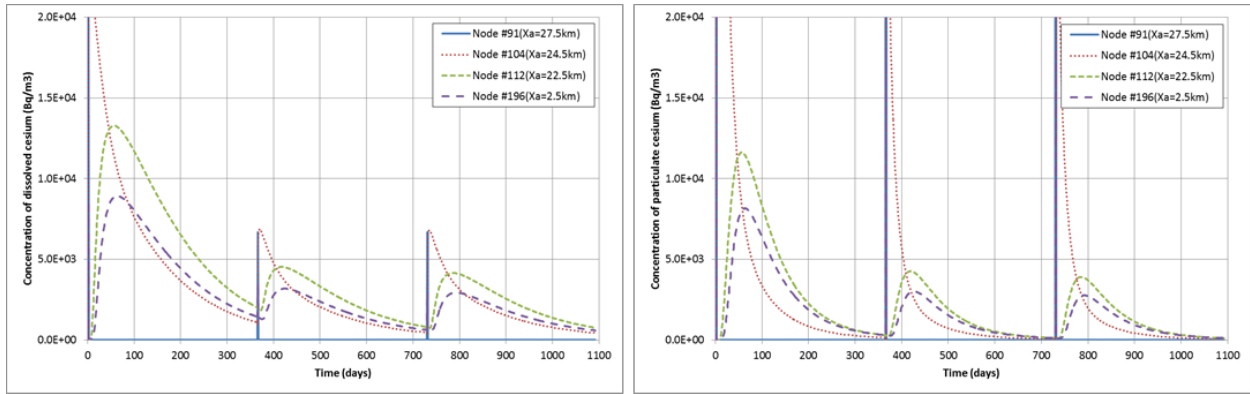
### 3.3.3 Effects of Countermeasures

In this section, countermeasures against the contaminant migration are discussed using some tentative simulations. The water that had been used for irrigation before the Fukushima nuclear accident was mainly from the Ogaki Dam Reservoir and the river below the dam. Therefore, water in the reservoir and in the river below the dam is the main targets.

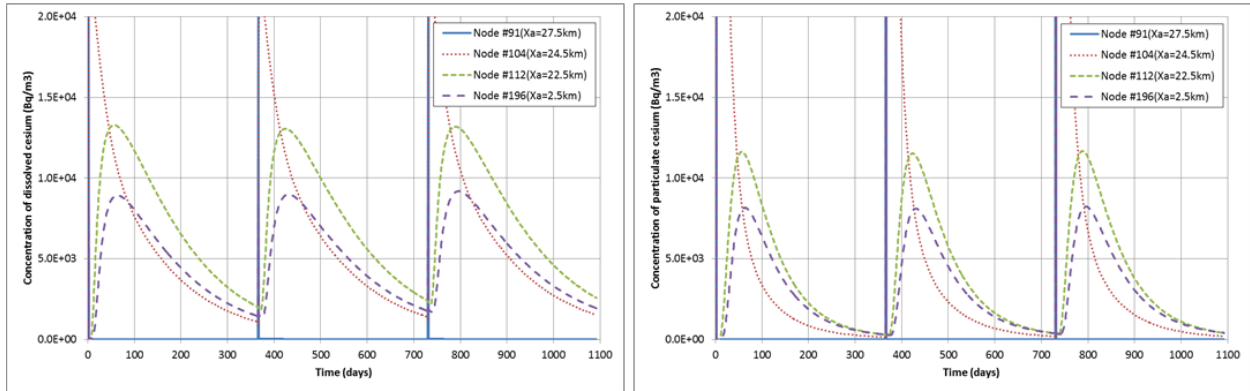
As shown in Figure 3.40 and Figure 3.41, the water contamination may continue for months after heavy rainfall events. In order to decrease tails of the contamination, three cases of simulation were applied: a case of decontamination of land surface, a case of dam control and a case of sorbent injection.

Figure 3.45 shows the results. In the case of land surface decontamination, inflow of cesium from the overland was assumed to be decreased by two-thirds after the first cycle. As a result, the concentrations of both dissolved and particulate cesium decreased by about two-thirds in the second and third cycles. In the case of dam control, the water level of the reservoir was increased by two meters after the first cycle to decrease the outflow from the Ogaki Dam. In this case, almost no effect could be seen. This is because the transport behavior within the reservoir was dispersion-dominant rather than advection-dominant. In the case of sorbent injection, silt-size sorbent was injected at 1.0 kg/s at the entrance of the reservoir during the high flow periods in the second and the third cycles, where the distribution coefficient of the sorbent was set to 100 m<sup>3</sup>/kg. This reduced the concentrations of cesium by 60–90 %.

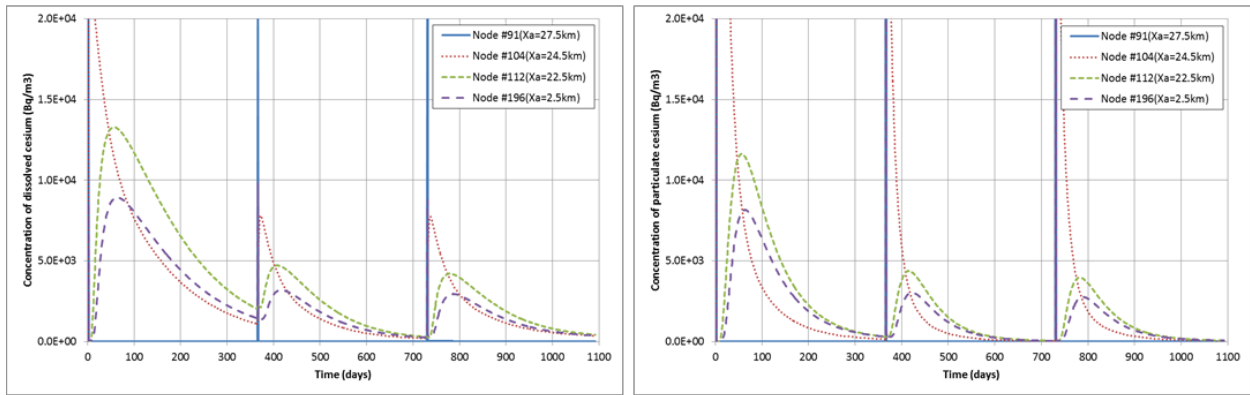
Although the simulations were preliminary and the parameters should be more realistically defined based on the investigations, land decontamination and sorbent injection may be effective countermeasures to decrease the contamination in the water.



(a) Concentrations of Dissolved and Particulate Cesium for the Case of Overland Decontamination



(b) Concentrations of Dissolved and Particulate Cesium for the Case of Dam Control



(c) Concentrations of Dissolved and Particulate Cesium for the Case of Sorbent Injection

**Figure 3.45.** Results of Countermeasure Simulations



## 4.0 Ogi Dam Modeling

### 4.1 Description of the Ogi Dam Reservoir

The Ogi Dam in the Oginosawa River is located in a mountainous area near Kawauchi Village about 15 km southwest of the Fukushima Daiichi NPP (Figure 4.1). Its water had been used for irrigation before the Fukushima nuclear accident, as with the Ogaki Dam Reservoir on the Ukedo River, but it is much smaller than the Ogaki Dam Reservoir. Figure 4.2 shows the contours of the reservoir bed elevation measured by Funaki et al. (2013). Figure 4.3 and Figure 4.4 show the bed elevation and the width along the thalweg starting from the Ogi Dam at the end of the reservoir. The length of the reservoir along the thalweg is about 580 m and the width varies from 20 m to 140 m. The water level was 362 m above sea level before the Fukushima accident, but it was lowered to 358 m after the accident to avoid collapse of the dam structure due to any aftershocks because it is located in an evacuation area and cannot be managed.

The main entrance of the river water is at the southwestern end. The rate of inflow is about  $0.01 \text{ m}^3/\text{s}$ .



**Figure 4.1.** Location of the Ogi Dam and Images of the Area

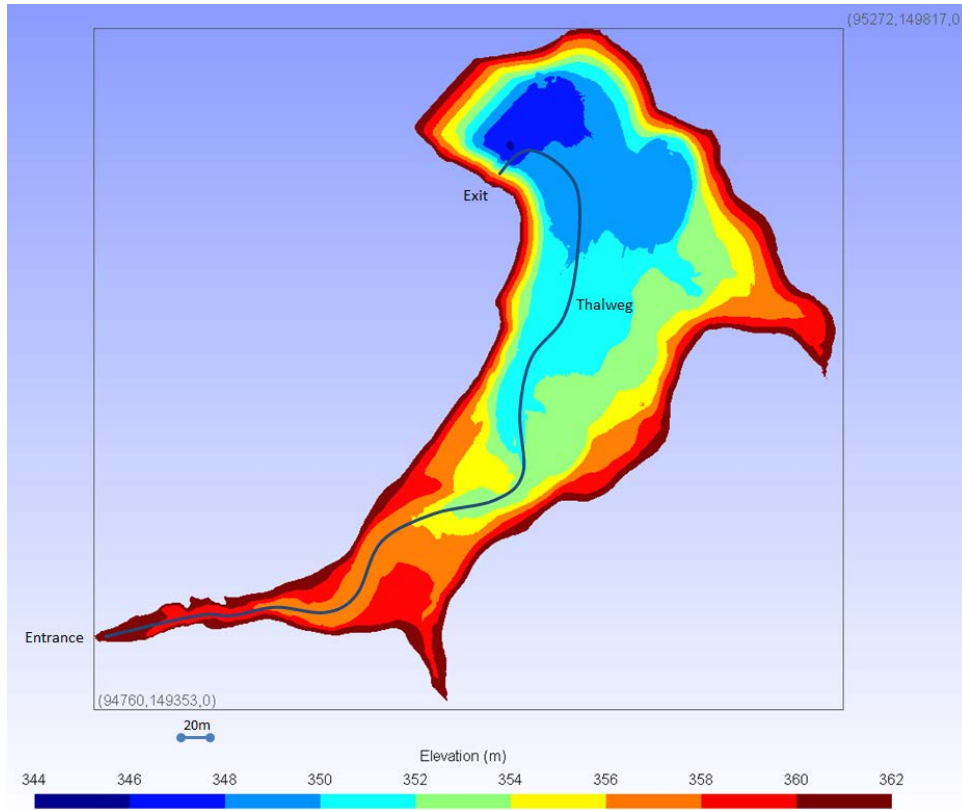


**Figure 4.2.** Contours of the Bed Elevation in the Ogi Dam Reservoir

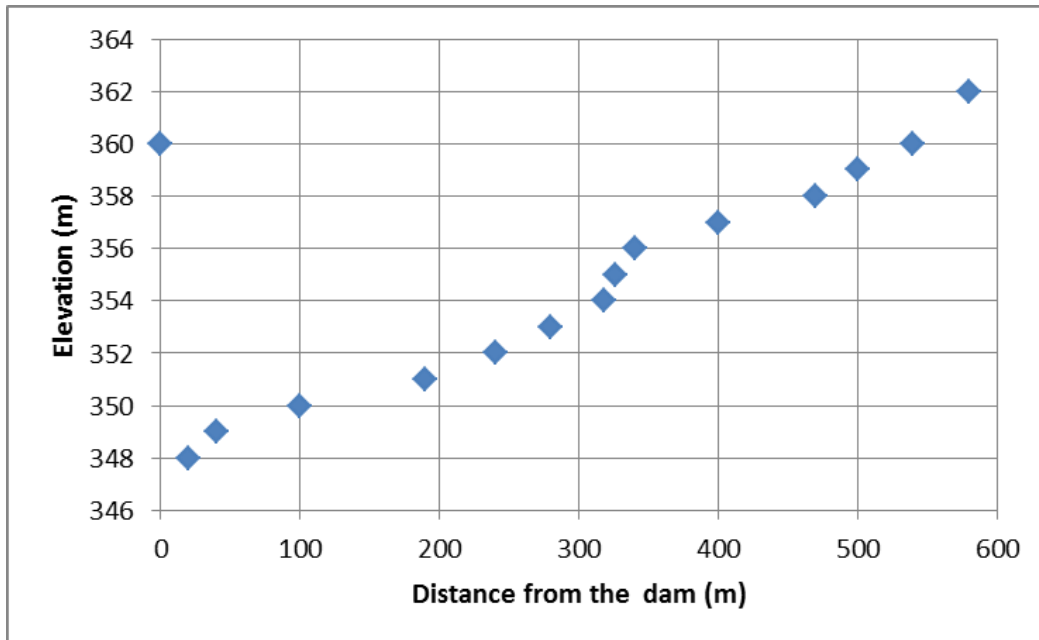


**Figure 4.3.** Bed Elevation of the Ogi Dam Reservoir along the Thalweg

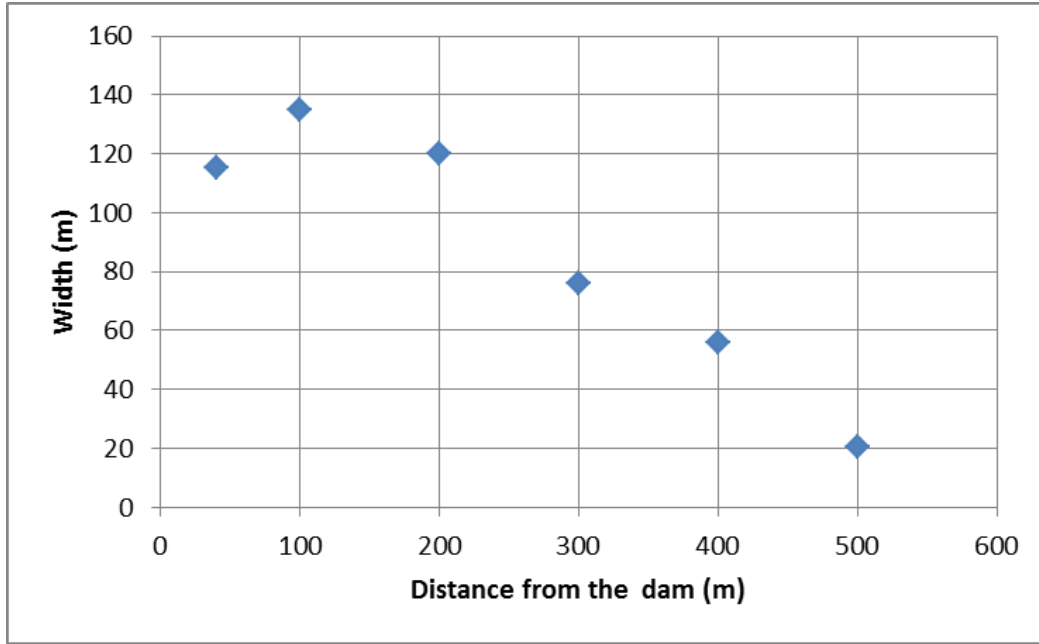


Figure 4.4. Width of the Ogi Dam Reservoir along the Thalweg

## 4.2 Simulation Results

### 4.2.1 Analytical Conditions

Prior to the simulation by the TODAM code, a jet mixing effect was calculated by using the theory described by Wiegel (1964) to check applicability of the one-dimensional code. In the theory, the longitudinal velocity  $u$  is obtained by the following equations for the case of a circular orifice of the three-dimensional round jet injected to the infinite space of homogeneous fluid.

For the zone of flow establishment,

$$\frac{u}{u_0} = \exp\left[-\frac{\left(r + C_2x - \frac{1}{2}D_0\right)^2}{2C_2^2x^2}\right] \text{ for } r > \frac{D_0}{2} - C_2x \quad (4.1)$$

$$\frac{u}{u_0} = 1 \text{ for } r < \frac{D_0}{2} - C_2x \quad (4.2)$$

For the zone of established flow,

$$\frac{u}{u_0} = \frac{1}{2C_2} \frac{D_0}{x} \exp\left[-\frac{1}{2C_2^2} \frac{r^2}{x^2}\right] \quad (4.3)$$

Here,  $u_0$  is the velocity at the orifice,  $x$  is the distance from the outlet,  $r$  is the radial coordinate,  $D_0$  is the diameter of the orifice, and  $C_2$  is a constant.

The results shown in Figure 4.5 and Figure 4.6 suggest that the river water into the reservoir is well enough mixed within 200 m from the entrance and the one-dimensional analysis by TODAM is reasonable.

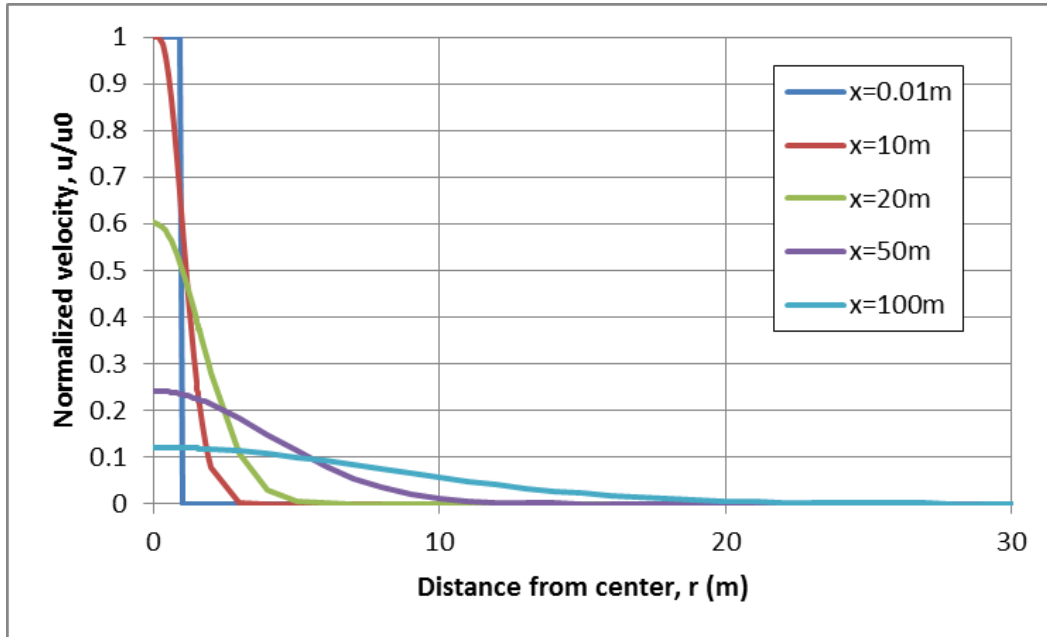


Figure 4.5. Velocity Distributions Estimated by the Jet Mixing Theory for  $x = 0.1\text{--}100\text{ m}$

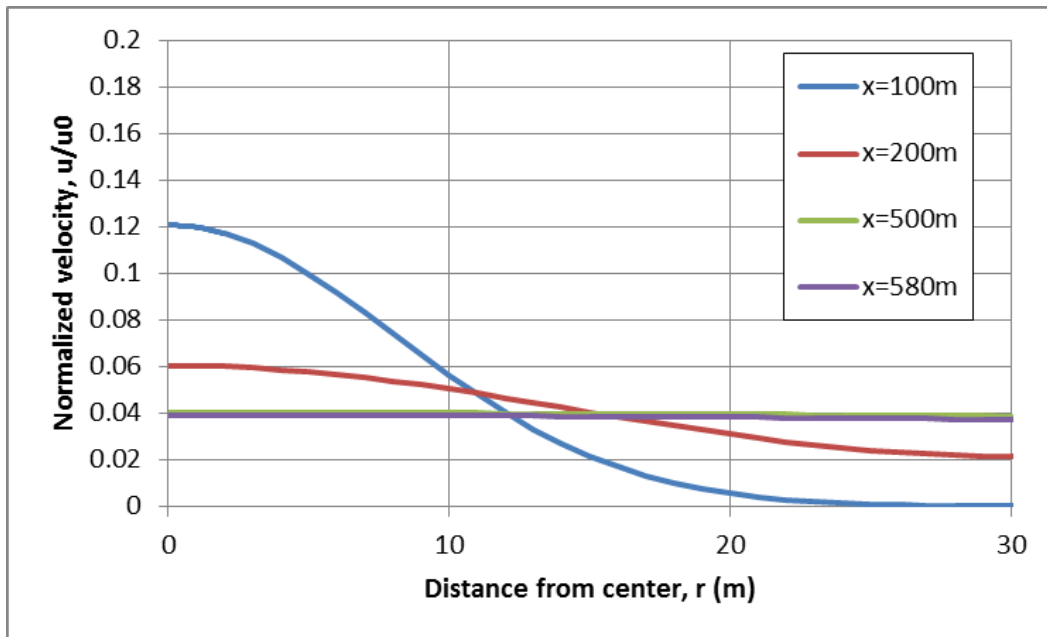
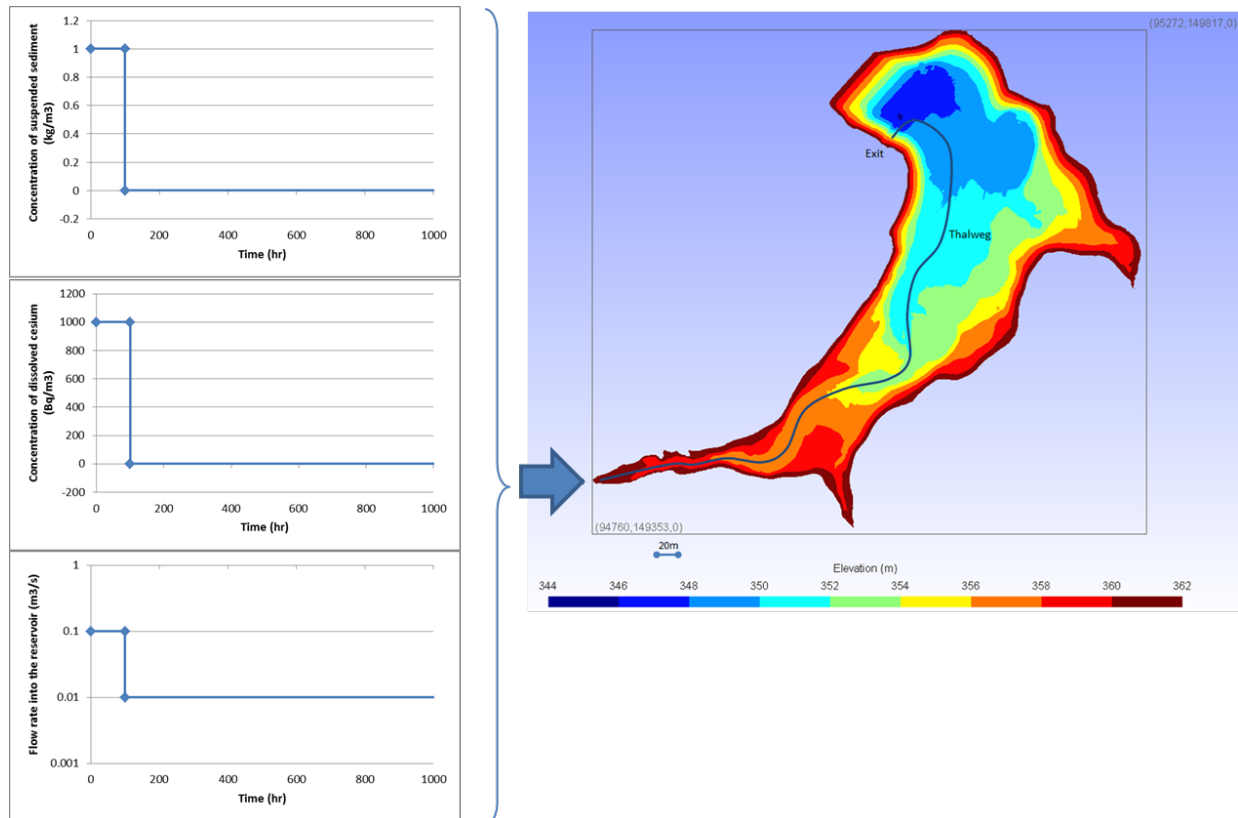


Figure 4.6. Velocity Distributions Estimated by the Jet Mixing Theory for  $x = 100\text{--}580\text{ m}$

The reservoir was divided into 58 model segments of 10-m length for the TODAM simulation. No tributary was considered.

The boundary conditions are shown in Figure 4.7. High rates of water flow, sediments and dissolved cesium were given at the entrance of the reservoir during the first 100 hours, followed by a low flow rate without sediment or cesium. The purpose of the simulation was to roughly evaluate whether the reservoir plays the role of sink or source of sediments and cesium. The dispersion coefficient was assumed to be  $0.01 \text{ m}^2/\text{s}$ , and the  $K_d$  values of sand, silt, and clay were assumed to be 0.68, 4.50, 22.9  $\text{m}^3/\text{kg}$ , respectively. The other parameters were same as for the Ukedo River simulations.



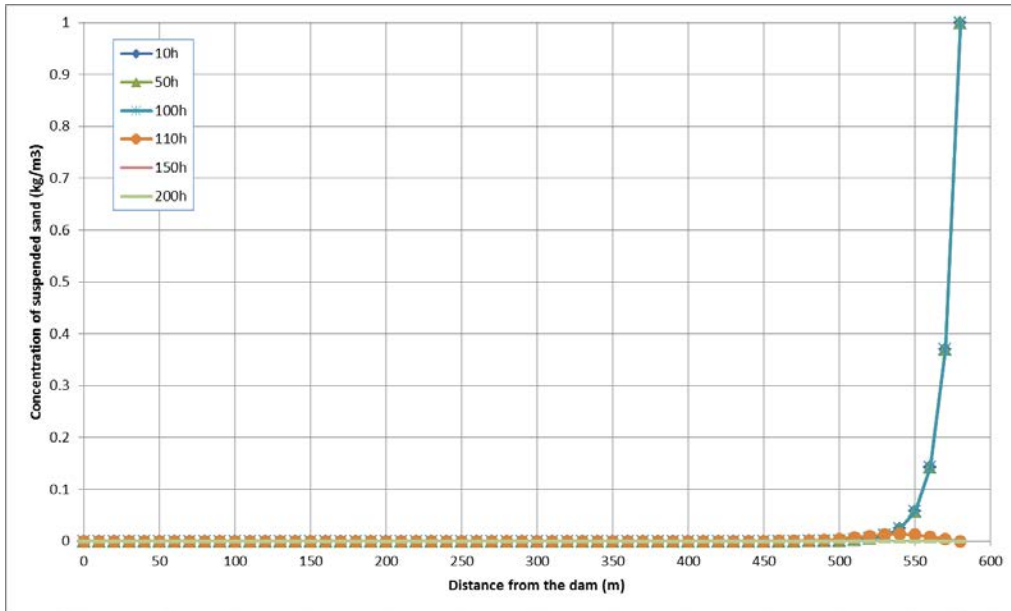
**Figure 4.7.** Boundary Conditions for Simulation of the Ogi Dam Reservoir

## 4.2.2 Simulation Results

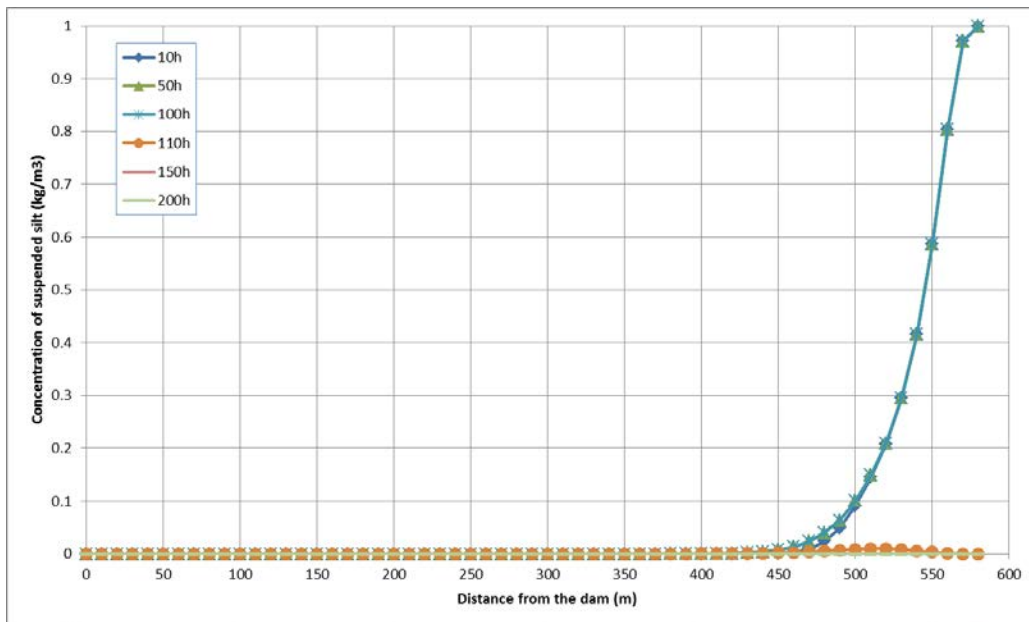
Figure 4.8, Figure 4.9, and Figure 4.10 show the simulated distributions of concentrations of suspended sand, silt, and clay, respectively, at various times. It can be seen that suspended sand and silt deposited early after the end of the high inflow. On the other hand, suspended clay was gradually transported downstream by advection and dispersion and some amount reached the exit. Figure 4.11 shows the simulated distributions of bed sediment. The smaller the sediment particle is, the farther it is transported from the reservoir entrance.

Figure 4.12, Figure 4.13, and Figure 4.14 show the simulated concentrations of dissolved and clay-sorbed cesium. Some amount reached the reservoir exit.

Table 4.1 and Table 4.2 summarize the mass balances of the sediments and the cesium at the end of the simulation; 100% of the sand and silt that entered the reservoir deposited, while 13% of the clay went out of the reservoir and 13% remained suspended within the reservoir. Regarding the cesium, 13% exited the reservoir in clay-sorbed and dissolved forms, and 62% was stored in the bed. The numerical error was less than 10%.



**Figure 4.8.** Distributions of Concentrations of Suspended Sand in the Ogi Dam Reservoir



**Figure 4.9.** Distributions of Concentrations of Suspended Silt in the Ogi Dam Reservoir

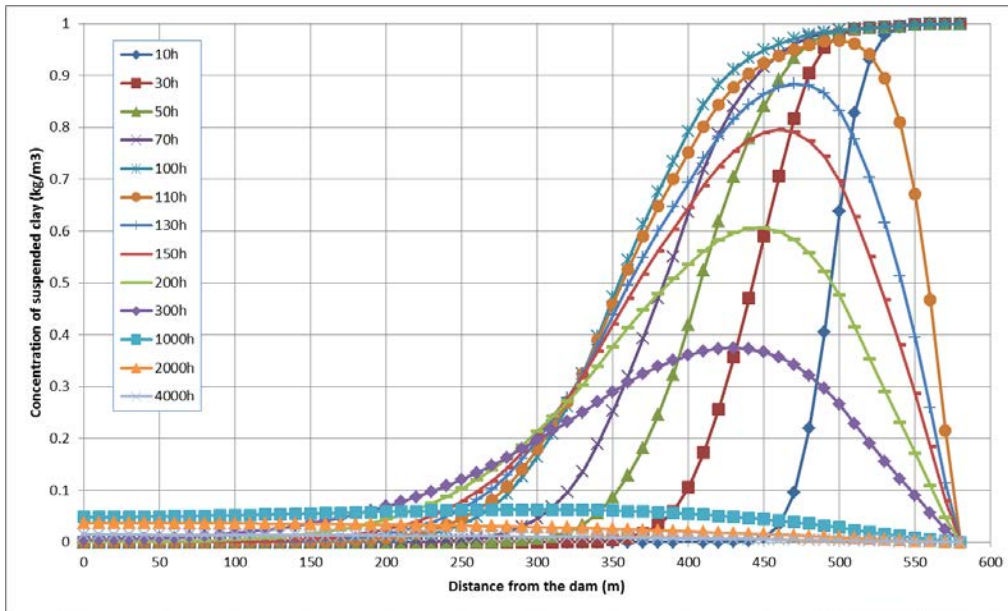


**Figure 4.10.** Distributions of Concentrations of Suspended Clay in the Ogi Dam Reservoir

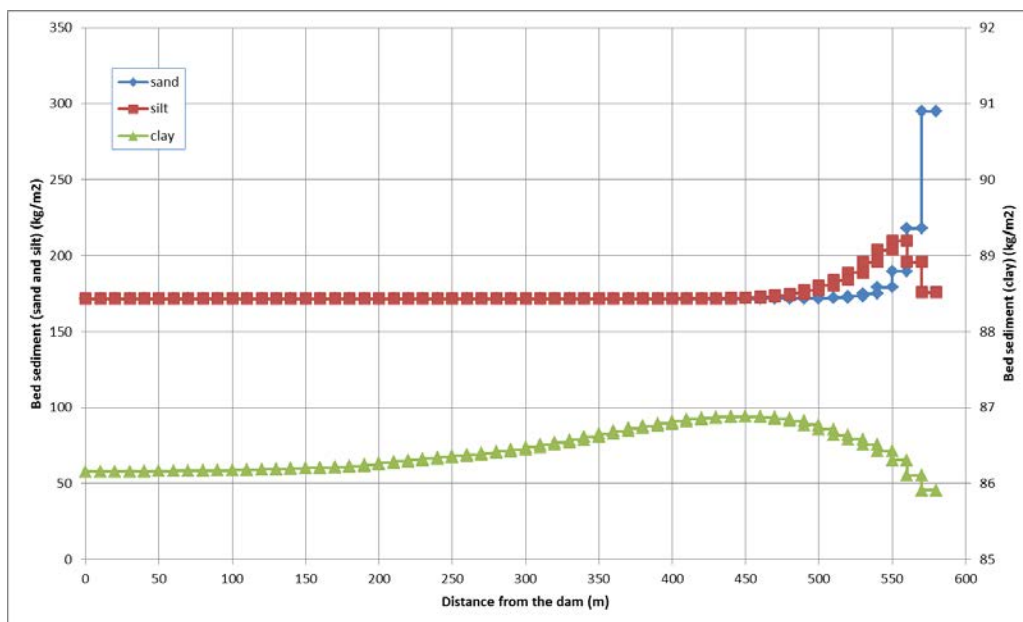


**Figure 4.11.** Distributions of Sediment in the Ogi Dam Reservoir Bed

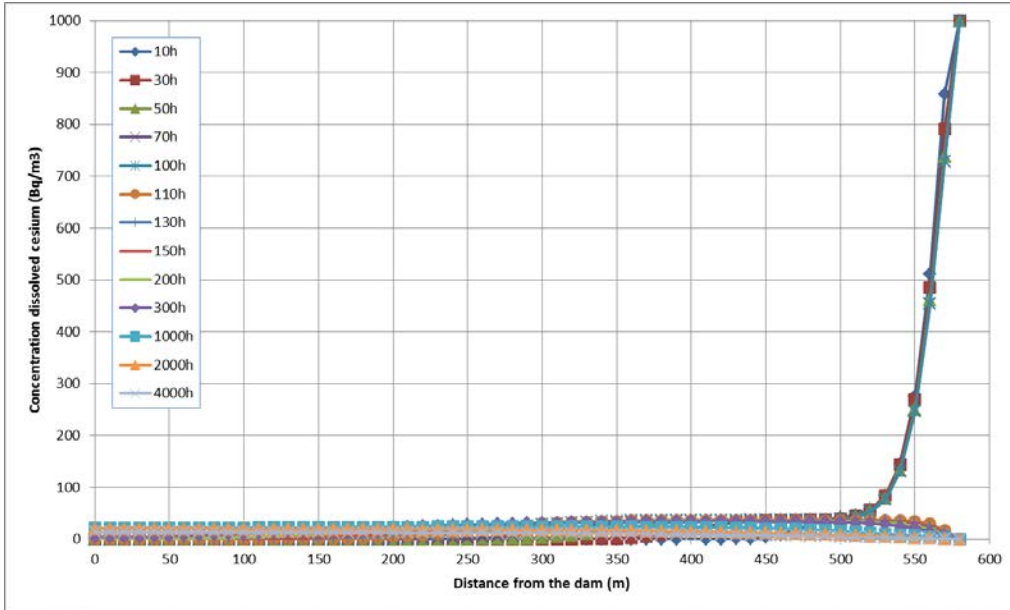


**Figure 4.12.** Distributions of Dissolved Cesium Concentration in the Ogi Dam Reservoir

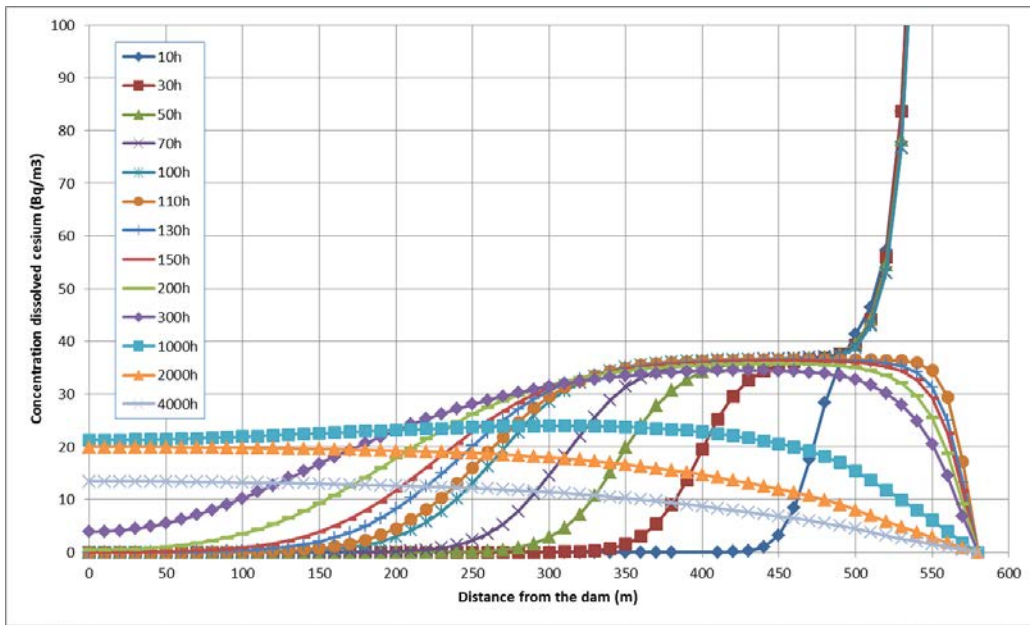


**Figure 4.13.** Distributions of Dissolved Cesium Concentration in the Ogi Dam Reservoir (magnified)

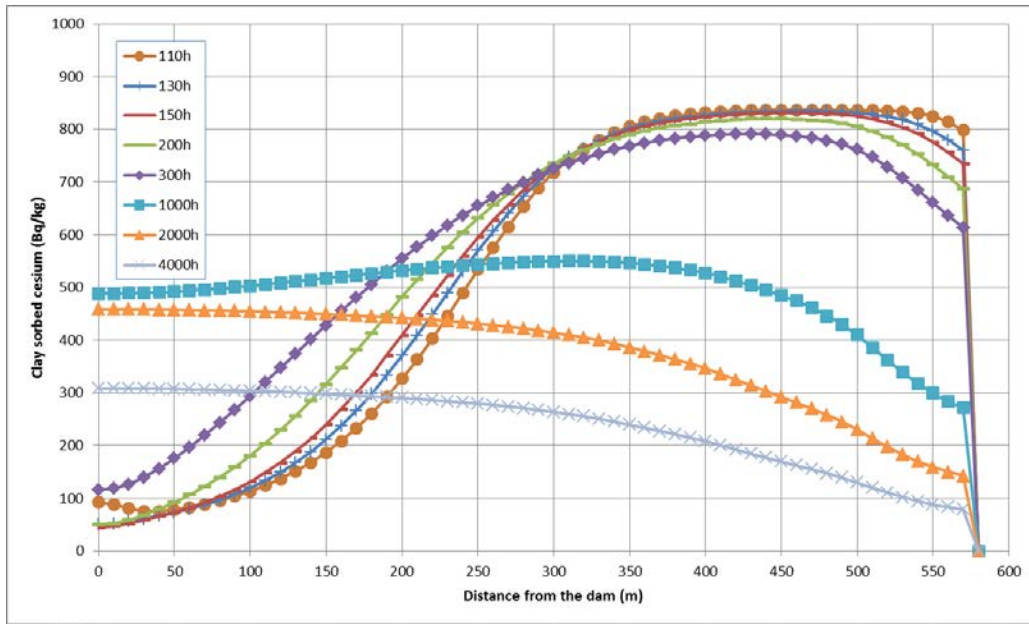


**Figure 4.14.** Distributions of Clay-Sorbed Cesium Concentration in the Ogi Dam Reservoir

**Table 4.1.** Mass Balances of Sediments in the Ogi Dam Reservoir

Sediment (kg)	Inflow	Outflow	Storage (Suspended)	Storage (Bed)
Sand	3.81E+4 (100%)	0 (0%)	0 (0%)	4.01E+4 (105%)
Silt	3.61E+4 (100%)	0 (0%)	0 (0%)	3.65E+4 (101%)
Clay	3.58E+4 (100%)	0.45E+4 (13%)	0.48E+4 (13%)	2.68E+4 (75%)

**Table 4.2.** Mass Balance of Cesium in the Ogi Dam Reservoir

Cesium (Bq)	Inflow	Outflow	Storage (Suspended)	Storage (Bed)
Sand sorbed	0	0	0	0.02E+7
Silt sorbed	-0.01E+7	0	0	0.42E+7
Clay sorbed	-0.08E+7	0.20E+7	0.14E+7	1.49E+7
Dissolved	3.67E+7	0.25E+7	0.47E+7	0.28E+7
<b>Total</b>	<b>3.58E+7</b> <b>(100%)</b>	<b>0.45E+7</b> <b>(13%)</b>	<b>0.61E+7</b> <b>(17%)</b>	<b>2.21E+7</b> <b>(62%)</b>



## 5.0 Conclusions

We simulated the sediment and cesium transport in the Ukedo River with its tributaries and the Ogi Dam Reservoir during and after heavy rainfall events using the TODAM code. The main outcomes were the following:

- Suspended sand is mostly deposited on the river bottom. Suspended silt and clay, on the other hand, are hardly deposited in the Ukedo River and its tributaries except in the Ogaki Dam Reservoir in the Ukedo River even in low river discharge conditions.
- Cesium migrates mainly during high river discharge periods during heavy rainfall events. Silt and clay play more important roles in cesium transport to the sea than sand does.
- The simulation results explain variations in the field data on cesium distributions in the river. Additional field data currently being collected and further modeling with these data may shed more light on the cesium distribution variations.
- Effects of 40-hour heavy rainfall events on clay and cesium transport continue for more than a month. This is because these reservoirs slow down the storm-induced high flow moving through these reservoirs.
- The reservoirs play a major role as a sink of sediment and cesium in the river systems. Some amounts of sediment pass through them along with cesium in dissolved and clay-sorbed cesium forms.
- Effects of countermeasures such as overland decontamination, dam control and sorbent injection in the reservoir were tentatively estimated. The simulation suggested that overland decontamination and sorbent injection would be effective to decrease the contamination of water in the reservoir and in the river below the dam.



## 6.0 References

- Chow VT. 1959. *Open Channel Hydraulics*. McGraw-Hill. Inc., New York.
- Colby BR. 1964. *Discharge of Sands and Mean Velocity Relationships in Sand-Bed Streams*. Geological Survey Professional Paper 462-A, U.S. Geological Survey, Washington, D.C.
- Du Boys P. 1879. *Le Rohne et les Riveieres a Lit Affouillable, Annales des Ponts et Chaussees*. Series 5, Vol. 18, pp. 141–195.
- Fukushima Prefecture. 2005. 請戸川水系河川整備基本方針.
- Funaki H, H Hagiwara, and T Tsuruta. 2013. “The Behaviour of Radiocaesium Deposited in an Upland Reservoir after the Fukushima Nuclear Power Plant Accident.” *Proceedings of the International Symposium “Scientific Basis for Nuclear Waste Management” (MRS 2013)*, in Press, September 30–October 4, 2013, Barcelona, Spain.
- Graf WH. 1971. *Hydraulics of Sediment Transport*. McGraw-Hill Book Co., New York.
- Holly Jr. FM, JC Yang, P Schwarz, J Schaefer, SH Hsu, and R Einhellig. 1990. *Numerical Simulation of Unsteady Water and Sediment Movement in Multiply Connected Networks of Mobile-Bed Channels*. IHR Report No. 343, Iowa Institute of Hydraulic Research, The University of Iowa, Iowa City.
- Iijima K, T Niizato, A Kitamura, H Sato and M Yui. 2013. *Long-term Assessment of Transport of Radioactive Contaminant in the Environment of Fukushima (F-TRACE)*. Japan Atomic Energy Agency, Fukushima, Japan. Accessed February 17, 2014 at [http://fukushima.jaea.go.jp/initiatives/cat01/pdf00/20\\_\\_Iijima.pdf](http://fukushima.jaea.go.jp/initiatives/cat01/pdf00/20__Iijima.pdf)
- International Atomic Energy Agency. 2001. *Generic Models for Use in Assessing the Impact of Discharges of Radioactive Substances to the Environment*. Safety Reports Series No. 19, Vienna, Austria.
- Japan Atomic Energy Agency (JAEA). 2013a. 平成 23 年度放射能測定調査委託事業「福島第一原子力発電所事故に伴う放射性物質の第二次分布状況等に関する調査研究」成果報告書.
- Japan Atomic Energy Agency (JAEA). 2013b. 平成 24 年度放射能測定調査委託事業「福島第一原子力発電所事故に伴う放射性物質の長期的影響把握手法の確立」成果報告書.
- Japan Atomic Energy Agency (JAEA). 福島県における放射性核種の環境中移動調査・研究～福島長期環境動態研究 (F-TRACE) プロジェクト～. Accessed January 29, 2014 at <http://fukushima.jaea.go.jp/initiatives/cat01/pdf/project.pdf>.
- Krone RB. 1962. *Flume Studies of the Transport of Sediment in Estuarial Shoaling Processes*. Hydraulic Engineering and Sanitary Engineering Research Laboratory, University of California, Berkeley.

Kurikami H, A Kitamura, M Yamaguchi, and Y Onishi. 2013. “Preliminary Calculation of Sediment and <sup>137</sup>Cs Transport in the Ukedo River of Fukushima.” In *Transactions of the American Nuclear Society*, vol. 109, pp. 149–152, 2013 Winter Meeting, Washington, D.C., November 10–14, 2013.

National and Regional Policy Bureau (Ministry of Land, Infrastructure, Transport and Tourism). National Land Numerical Information, available at <http://nlftp.mlit.go.jp/ksj-e/index.html>.

Onishi Y, OV Voitshkovich, and MJ Zheleznyak (eds.). 2007. *Chernobyl – What Have We learned? The Successes and Failures to Mitigate Water Contamination Over 20 Years*. Springer Publishers, Dordrecht, The Netherlands.

Onishi Y and ST Yokuda. 2013. *2012 Annual Report: Simulate and Evaluate the Cesium Transport and Accumulation in Fukushima-Area Rivers by the TODAM Code*. PNNL-22364, Pacific Northwest National Laboratory, Richland, Washington.

Partheniades E. 1962. *A Study of Erosion and Deposition of Cohesive Soils in Salt Water*. Ph.D. Thesis, University of California, Berkeley.

Teeter AM. 1988. *New Bedford Harbor Superfund Project, Acushnet River Estuary Engineering Feasibility Study of Dredging and Dredged Material Disposal Alternatives, Report 2 Sediment and Contaminant Hydraulic Transport Investigations*. Technical Report EL-88-15, U.S. Army Corps of Engineers, Vicksburg, Mississippi.

Toffaleti FB. 1969. “Definitive Computations of Sand Discharge in Rivers.” *Journal of the Hydraulics Division*, American Society of Civil Engineers, Vol. 95, No. 1 Proceeding Paper 6350, pp. 225–248.

Vanoni VA (ed.). 1975. *Sedimentation Engineering*. ASCE Manuals and Report on Engineering Practice, American Society of Civil Engineers, New York.

Wiegel RL. 1964. *Oceanographical Engineering*. Prentice-Hall Inc./Englewood Cliffs, N.J.

Yamaguchi M, K Maekawa, S Takeuchi, A Kitamura, and Y Onishi. 2013. “Development of a Model to Predict a Radionuclide Distribution Based on Soil Migration after Fukushima Dai-ichi Nuclear Power Plant Accident.” *Journal of Nuclear Fuel Cycle and Environment*, Vol. 20, No. 2, pp. 53–69.

## **Appendix**

### **CHARIMA Description**

**CHARIMA**

**NUMERICAL SIMULATION OF UNSTEADY  
WATER AND SEDIMENT MOVEMENT IN  
MULTIPLY CONNECTED NETWORKS OF  
MOBILE-BED CHANNELS**

by F.M. Holly Jr., J.C. Yang, P. Schwarz,  
J. Schaefer, S.H. Hsu, and R. Einhellig

IIHR Report No. 343

Iowa Institute of Hydraulic Research  
The University of Iowa  
Iowa City, Iowa 52242 USA

July 1990

## I. INTRODUCTION

Analysis of the long-term effects of river-development schemes on alluvial-channel morphology has become an essential element of planning and feasibility studies for river engineering projects. Despite the present weaknesses in understanding of the extremely complex mechanisms of sediment deposition onto the river-bed and reentrainment into the flow, engineers are nonetheless called upon to make their best possible predictions of bed-level changes over extended periods of time. These predictions are commonly based on the use of numerical simulation techniques.

Virtually all developmental efforts consecrated to the bed-evolution simulation problem have dealt with simple systems of a single river channel, branched channel systems, or systems having a few isolated multiply-connected flow paths. But when a river carries an extremely high sediment load imposed upon it by a tributary, it tends to form a braided system of multiply connected channels, thus increasing overall sediment-transport capacity. Existing bed-evolution computational techniques are inadequate for treatment of this multi-channel problem.

In 1984 the Harza-Ebasco Susitna Joint Venture requested the Iowa Institute of Hydraulic Research (IIHR) to develop and furnish a computational code for the prediction of the long-term bed evolution in a portion of the Susitna River, Alaska. As can be seen in Figure I.1, this 14-mile reach of the Susitna (from near Talkeetna to the Sunshine Bridge, RM 98.1 to RM 83.9), is highly braided due to the heavy sediment inflows coming from the Chulitna and Talkeetna tributaries. During preliminary review of existing data, it became apparent that it would be impossible to perform reliable long-term simulation through assimilation of the multiple braided channels into a single equivalent channel. Indeed, in the vicinity of the Chulitna-Talkeetna confluence, the channel evolution patterns must be considered as at least quasi-two-dimensional. The Chulitna water and sediment inflows enter primarily the right-bank channel, whereas the Talkeetna inflows enter primarily the left-bank channel. It would have been impossible to study the detailed interactions among water and sediment from the three sources (Susitna, Chulitna, Talkeetna) in this zone without explicit recognition of the multiple flow paths. Therefore the needs of the Susitna project required that a new technique for treatment of multiply-connected alluvial systems be developed. The BRALLUVIAL and CHARIMA codes, the latter of whose description is the primary purpose of this report, are the results of the developmental efforts.

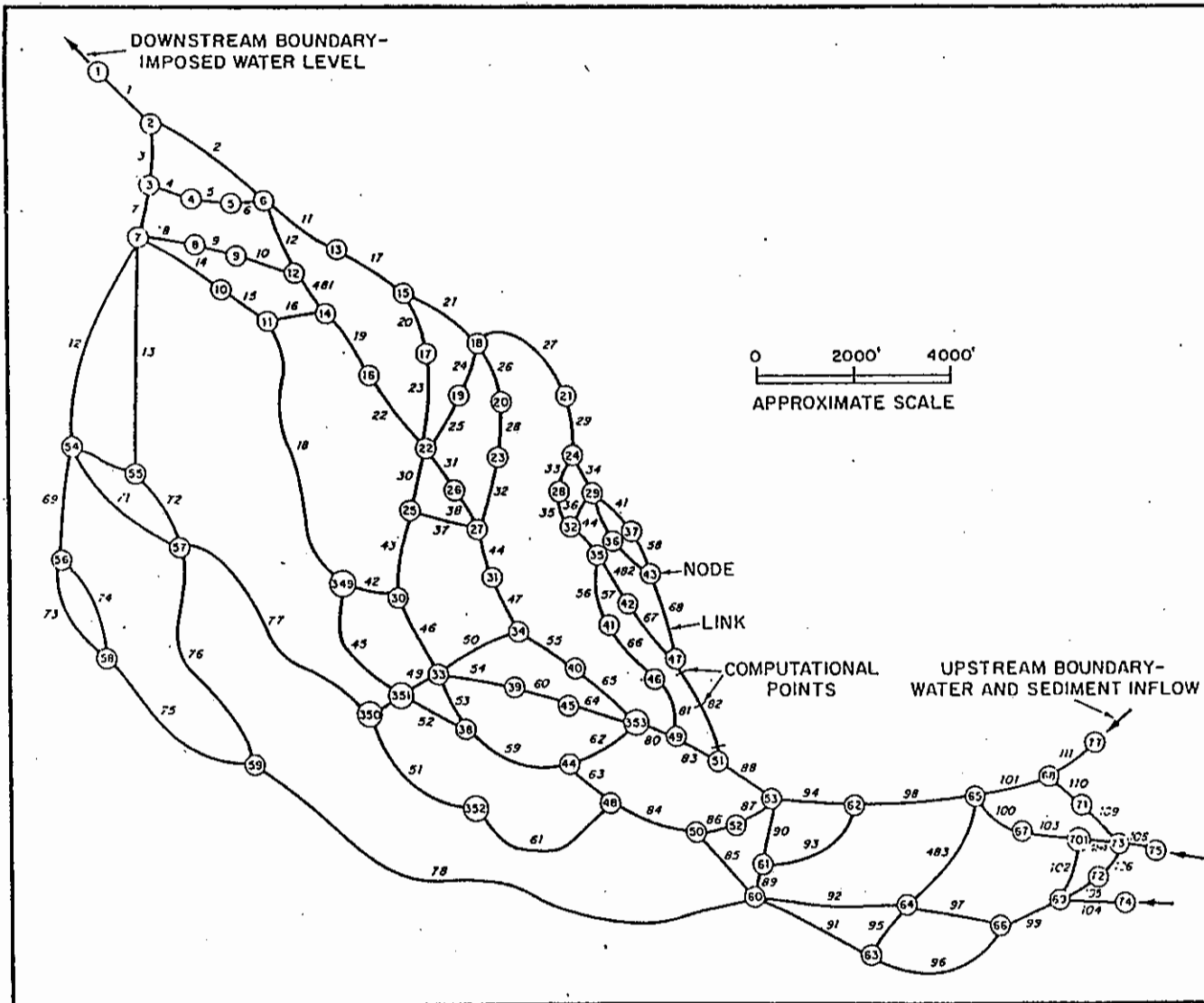


Figure I.1. Schematic diagram of a portion of the Susitna multi-connected network.

The BRALLUVIAL and CHARIMA programs stand on the shoulders of two existing state-of-the-art codes. The first one is IIHR's IALLUVIAL program, which computes quasi-steady water and sediment movement, and bed evolution, in a single channel having non-uniform bed sediments and subject to bed armoring and sorting processes. (Karim and Kennedy, 1982; Karim and Holly, 1983; Holly and Karim, 1983; Karim, Holly, and Kennedy, 1983; Holly, Yang, and Karim, 1984). The second code is SOGREAH's CARIMA program for unsteady flow computation in branched and looped fixed-bed channel systems (Holly and Cunge, 1978).

The remainder of this report is devoted to a detailed description of the formulations and procedures employed in CHARIMA. A complete description of the Susitna application can be found in the Harza-Ebasco companion report (Lin, 1985). The BRALLUVIAL code is fully documented by Holly et al. (1985). Additional analysis of CHARIMA can be found in the thesis of Yang (1986). Most of the material in this report originally appeared in one or the other of these latter two documents.

## II. THEORETICAL BASIS AND SOLUTION STRATEGY

### II.1. Governing Equations and Hypotheses

The basic one-dimensional governing equations for unsteady water flow and nonuniform sediment transport in a channel are:

Water-Continuity Equation

$$\frac{\partial A}{\partial t} + \frac{\partial Q}{\partial x} = 0 \quad (\text{II.1})$$

Momentum Equation

$$\frac{\partial Q}{\partial t} + \frac{\partial}{\partial x} \left( \alpha \frac{Q^2}{A} \right) + gA \frac{\partial y}{\partial x} + gA \frac{Q|Q|}{K^2} = 0 \quad (\text{II.2})$$

Sediment-Discharge Predictor

$$F_1(Q_s, D_{50}, Q, A, d, S_f, ACF) = 0 \quad (\text{II.3})$$

Friction-Factor Predictor

$$F_2(Q, A, D_{50}, S_f, d, ACF) = 0 \quad (\text{II.4})$$

Sediment Continuity Equation

$$(1-p) B \frac{\partial z}{\partial t} + \frac{\partial Q_s}{\partial x} = 0 \quad (\text{II.5})$$

Channel Geometry

$$A = A(d; x) \quad (\text{II.6})$$

$$B = B(d; x) \quad (\text{II.7})$$

## Hydraulic Sorting of Bed Material

$$D_{50}^n \rightarrow D_{50}^{n+1} \quad (\text{II.8})$$

## Armoring of Bed Surface

$$\text{ACF}^n \rightarrow \text{ACF}^{n+1} \quad (\text{II.9})$$

where,

Q	=	water discharge;
A	=	cross-sectional area;
y	=	water surface elevation;
S <sub>f</sub>	=	energy slope;
g	=	gravitational acceleration;
α	=	momentum correction factor;
z	=	bed elevation;
Q <sub>s</sub>	=	sediment discharge;
D <sub>50</sub>	=	median size of bed material;
B	=	water surface width;
ACF	=	armoring factor (proportion to the bed surface covered by the immovable particles);
p	=	porosity;
K	=	conveyance;
d	=	flow depth.

The two independent variables are x, the longitudinal coordinate; and t, time. The gravitational acceleration g, the sediment porosity p, and many other physical quantities which are independent of the bed evolution process appear in the functions F<sub>1</sub> and F<sub>2</sub>. Eq. (II.8) symbolizes the accounting operations which simulate the sorting, n and n+1 representing successive points in time. Eq. (II.9) symbolizes the additional accounting operations which simulate development and destruction of a stable armor layer. Continuous lateral inflow is not considered in the above formulations, but it can be added with no algorithm complication.

For water flow, the de St Venant (1871) hypotheses are essentially taken into account in the above equations:

- 1) the flow is one-dimensional, i.e., the velocity is uniform over the cross section and the water level across the section is horizontal;
- 2) hydrostatic pressure distribution prevails at any point in the channel;
- 3) the resistance laws for steady-state flow are applicable to unsteady flow;
- 4) the channel bed slope is small.

In addition to the above assumptions, when looped-channel formulations are applied, the channel network pattern must be assumed unchanged during the simulation. Channels may be dried out at low flow or flooded and indistinguishable one from another at high flow, but the total number of channels in the network and their interconnections must remain the same.

Furthermore, since only one-dimensional phenomena are considered, one has to assume something about how the section changes as a consequence of bed evolution. In this study, the cross section is assumed to rise or fall without changing its shape. Again, due to the one-dimensional restriction, the effect of river meanders on sediment transport, which may be considered as a dominant factor for a study reach with many small-curvature bends, cannot be covered in the above formulations. Many other restrictions associated with sediment-routing processes have also to be imposed, for example, those required for sorting and armoring processes, and sediment discharge and friction-factor predictors as described in subsequent sections. Finally, a basic assumption is that the sediment transport at a given time and location is a function only of local hydraulic and bed-sediment conditions.

## **II.2. Iterative Coupled Approach**

At any instant, the entire system of equations (II.1) to (II.7) must be simultaneously satisfied and consistent with the sorting and armoring processes of Eqs. (II.8) and (II.9). Were it possible to obtain an analytical solution to the entire system, this requirement of simultaneity would naturally be satisfied. But of course such an analytical solution cannot be obtained, due to the inherent nonlinearities; the tabular nature of Eqs. (II.6) and (II.7) for natural channels; the ad-hoc procedures (as opposed to mathematical relationships) of Eqs. (II.8) and (II.9); and the need to solve Eq. (II.5) for each size fraction, followed by a reconstitution of the total change in bed elevation,  $z$ .

Since no analytical solution is possible, a numerical method whose central feature is Preissmann's finite-difference approximation to Eqs. (II.1), (II.2), and (II.5) is used. The scheme replaces a continuous function, e.g.,  $Q$ , its time derivative and its space derivative by the following formulae:

$$Q = \theta \left[ \phi Q_{i+1}^{n+1} + (1-\phi) Q_i^{n+1} \right] + (1-\theta) \left[ \phi Q_{i+1}^n + (1-\phi) Q_i^n \right] \quad (\text{II.10})$$

$$\frac{\partial Q}{\partial t} = \frac{1}{\Delta t} \left[ \phi \left( Q_{i+1}^{n+1} - Q_{i+1}^n \right) + (1-\phi) \left( Q_i^{n+1} - Q_i^n \right) \right] \quad (\text{II.11})$$

$$\frac{\partial Q}{\partial x} = \frac{1}{\Delta x} \left[ \theta \left( Q_{i+1}^{n+1} - Q_i^{n+1} \right) + (1-\theta) \left( Q_{i+1}^n - Q_i^n \right) \right] \quad (\text{II.12})$$

in which the superscript  $n$  denotes the time level, the subscript  $i$  denotes the computational section;  $\Delta t$  is the computational time step;  $\Delta x$  is the distance between points  $i$  and  $i+1$  (not necessarily constant); and  $\theta$  and  $\phi$  are weighting factors between 0 and 1. In CHARIMA,  $\phi = 1/2$  is adopted throughout. Therefore, Eqs. (II.1), (II.2), and (II.5) take the following algebraic forms, after use of the Preissmann discretizations:

$$\begin{aligned} & \frac{1}{2\Delta t} \left( A_{i+1}^{n+1} - A_{i+1}^n \right) + \frac{1}{2\Delta t} \left( A_i^{n+1} - A_i^n \right) \\ & + \frac{\theta}{\Delta x} \left( Q_{i+1}^{n+1} - Q_i^{n+1} \right) + \frac{1-\theta}{\Delta x} \left( Q_{i+1}^n - Q_i^n \right) = 0 \quad (\text{II.13}) \\ & \frac{1}{2\Delta t} \left( Q_{i+1}^{n+1} - Q_{i+1}^n \right) + \frac{1}{2\Delta t} \left( Q_i^{n+1} - Q_i^n \right) \\ & + \left[ \alpha \theta \left( \frac{Q_i^{n+1}}{A_i^{n+1}} + \frac{Q_{i+1}^{n+1}}{A_{i+1}^{n+1}} \right) + \alpha(1-\theta) \left( \frac{Q_i^n}{A_i^n} + \frac{Q_{i+1}^n}{A_{i+1}^n} \right) \right] \\ & \left[ \frac{\theta}{\Delta x} \left( Q_{i+1}^{n+1} - Q_i^{n+1} \right) + \frac{1-\theta}{\Delta x} \left( Q_{i+1}^n - Q_i^n \right) \right] \end{aligned}$$

$$\begin{aligned}
& -\alpha \left[ \frac{\theta}{4} \left( \frac{Q_i^{n+1}}{A_i^{n+1}} + \frac{Q_{i+1}^{n+1}}{A_{i+1}^{n+1}} \right)^2 + \frac{1-\theta}{4} \left( \frac{Q_i^n}{A_i^n} + \frac{Q_{i+1}^n}{A_{i+1}^n} \right)^2 \right] \\
& \left[ \frac{\theta}{\Delta x} \left( A_{i+1}^{n+1} - A_i^{n+1} \right) + \frac{1-\theta}{\Delta x} \left( A_{i+1}^n - A_i^n \right) \right] \\
& + g \left[ \frac{\theta}{2} \left( A_i^{n+1} + A_{i+1}^{n+1} \right) + \frac{1-\theta}{2} \left( A_i^n + A_{i+1}^n \right) \right] \\
& \left[ \frac{\theta}{\Delta x} \left( y_{i+1}^{n+1} - y_i^{n+1} \right) + \frac{1-\theta}{\Delta x} \left( y_{i+1}^n - y_i^n \right) \right] \\
& + g \left[ \frac{\theta}{2} \left( A_i^{n+1} + A_{i+1}^{n+1} \right) + \frac{1-\theta}{2} \left( A_i^n + A_{i+1}^n \right) \right] \\
& \left\{ \theta \left[ \beta \frac{Q_i^{n+1} |Q_i^{n+1}|}{(K_i^{n+1})^2} + (1-\beta) \frac{Q_{i+1}^{n+1} |Q_{i+1}^{n+1}|}{(K_{i+1}^{n+1})^2} \right] \right. \\
& \left. + (1-\theta) \left[ \beta \frac{Q_i^n |Q_i^n|}{(K_i^n)^2} + (1-\beta) \frac{Q_{i+1}^n |Q_{i+1}^n|}{(K_{i+1}^n)^2} \right] \right\} = 0 \tag{II.14}
\end{aligned}$$

$$\frac{z_i^{n+1} - z_i^n + z_{i+1}^{n+1} - z_{i+1}^n}{\Delta t} = \frac{4\theta \left( Q_{S_i}^{n+1} - Q_{S_{i+1}}^{n+1} \right)}{(1-p)(B_i^{n+1} + B_{i+1}^{n+1}) \Delta x}$$

$$+ \frac{4(1-\theta) \left( Q_{S_i}^n - Q_{S_{i+1}}^n \right)}{(1-p)(B_i^n + B_{i+1}^n) \Delta x} \tag{II.15}$$

Since all needed values are known at time level  $n$  (from the initial condition or from the results of the previous time step), the problem becomes one of solving the nonlinear algebraic system of Eqs. (II.3), (II.4), (II.6-II.9), and (II.13-II.15) in which the nine unknowns would be understood to be at time level  $n+1$ . But even this formal approach is not feasible, since Eqs. (II.8) and (II.9) are non-analytical accounting procedures which have not been expressed as closed-form mathematical expressions.

This apparent impossibility of obtaining a simultaneous solution to even the algebraic equivalent of the original differential system leads to the adoption of a decoupling technique. The solution proceeds in three stages:

1) Equations (II.3, II.4, II.6, II.7, and II.13-II.14) are solved in a "hydraulic sweep". During this sweep, the bed elevation  $z$ , median diameter  $D_{50}$ , and armoring factor ACF are held constant, as if the bed were temporarily frozen. The essential result of this sweep is a calculation of the sediment transport capacity, and associated hydraulic parameters, at every point  $i$  and for every size fraction of bed material.

2) Equation (II.15) is solved in a "downstream sweep" from the upstream to the downstream boundaries to yield the new bed elevations  $z_i^{n+1}$  at each point  $i$ . This sweep treats the  $Q_{si}^{n+1}$  values as constant, as if the sediment transport capacity were temporarily unaffected by bed elevation, armoring, or median sediment size changes.

3) The accounting processes of Eqs. (II.8) and (II.9) are finally executed using the degradation or aggradation computed in step (2) above.

This methodology is referred to as "uncoupled", since it assumes that the three processes occur sequentially, and not concurrently, within a given time step. This apparent blatant violation of the principle of simultaneity of all mechanisms involved is rendered necessary by the practical difficulties associated with the lack of a closed-form representation of the armoring and sorting processes.

Most numerical models of physical processes use such a decoupling procedure, whose validity rests on the assumption that the change in any one variable during a time step is small enough that its effect on the other variables (during the time step) can be ignored. The objective of the iterative coupling procedure is to obtain, through iterative repetition within one time step, a genuine simultaneous solution of Eqs. (II.3, II.4, II.6-

II.9, II.13-II.15). The required sequence of iteration operations within one time step can be expressed as follows:

1) Load imposed boundary conditions (mainstem and tributary water and sediment inflows, downstream water surface elevation).

2) Using a fixed-bed elevation  $z$  (latest estimate), and the latest estimates of  $D_{50}$  and ACF, compute the depth  $d$ , flow area  $A$ , energy slope  $S_f$ , water surface width  $B$ , water discharge  $Q$ , and sediment-discharge capacity  $Q_s$  at each computational point through simultaneous solution of Eqs. (II.3, II.4, II.6, II.7, II.13, and II.14).

3) Using the values of  $Q_s$  and  $B$  computed in step 2) above, compute the new estimates of bed surface elevation  $z$  from Eq. (II.15).

4) Using the change in bed surface elevations computed in 3) above, compute the new estimates of armoring factor ACF and median sediment diameter  $D_{50}$  from Eqs. (II.8) and (II.9).

Steps (2)-(4) are repeated iteratively until successive estimates of  $z_i^{n+1}$  no longer change. When this convergence is reached, one is assured that the values of  $Q_s$  and  $B$  in Eq. (II.15) result from simultaneous solution of Eqs. (II.3, II.4, II.6-II.9, II.13-II.14) at each time level  $n$  and  $n+1$ . A flow chart for the above-mentioned solution strategy within one-time step is shown in Figure II.1.

### II.3 Supplementary Empirical Relations

**II.3.1. Sediment-Discharge Capacity.** Morphological computations for streams having nonuniform sediment requires that the sediment discharge be computed for each particle-size fraction. Many investigations have been focused on extending uniform-sediment transport models to the nonuniform sediment transport problem. A well-known example in which the sediment transport is separated for each particle size fraction is Einstein's bed-load concept (1950). The dimensionless transport of fraction  $j$  per Einstein's bed-load formula can be written as



$$\frac{q_{sj}}{\sqrt{(s-1)gD_j^3}} = \frac{Pt_j}{A_*} \frac{P}{1-P} \quad (\text{II.16})$$

in which  $A_*$  is a universal constant;  $P$  is the probability of erosion;  $q_{sj}$  is the sediment discharge for particle size  $j$ ;  $D_j$  is the diameter of particle size  $j$ ;  $Pt_j$  is the proportion of the size fraction  $j$  in the mixture;  $g$  is the gravitational constant; and,  $s$  is the specific gravity of sediment. The parameter  $P$  contains a hiding factor which is used to take into account the sheltering effect of smaller particles hiding behind larger ones.

Based on Einstein's concept, Meyer-Peter and Mueller (1948) developed a classical formula for transport of each size fraction:

$$\frac{q_{sj}(1-p)}{\sqrt{(s-1)gD_j^3}} = 13.3 Pt_j \left( \frac{C_f R_b S}{(s-1)D_j} - 0.047 \right)^{3/2} \quad (\text{II.17})$$

where  $C_f$  is a function of the bed roughness;  $p$  is the porosity of the bed material;  $R_b$  is the hydraulic radius with the wall effect correction; and  $S$  is the bed slope.

Ashida and Michine (1973) considered a hiding effect appearing in the calculation of critical shear stress, and introduced this effect in a transport predictor as follows:

$$\frac{q_{sj}}{\sqrt{(s-1)gD_j^3}} = 17 Pt_j \tau_*^{3/2} \left( 1 - \frac{\tau_{c*j}}{\tau_*} \right) \left( 1 - \frac{u_{c*j}}{u_*} \right) \quad (\text{II.18})$$

where  $u_*$  is the shear velocity;  $u_{c*j}$  is the critical shear velocity;  $\tau_*$  is the dimensionless shear stress; and  $\tau_{c*j}$  is the dimensionless critical shear stress developed by Egizoroff (1965):

$$\tau_{c*j} = \frac{\tau_{cj}}{(\gamma_s - \gamma_f) D_j} = \frac{0.1}{\log \left( 19 \frac{D_j}{D_m} \right)} \quad (\text{II.19})$$

with

$$D_m = \sum_{j=1}^n P_t_j D_j \quad (\text{II.20})$$

where  $\gamma_s$  is the specific weight of sediment, and  $\gamma_f$  is the specific weight of fluid.

The above-mentioned methods were developed on the basis of bed-load transport formulae. There are a few methods which were developed on the basis of the total-load (bed plus suspended) formulae. The most commonly used are the modified TLTM method (Karim, 1985), the modified Ackers-White method (Proffitt and Sutherland, 1983), and the Laursen formulation (1958).

TLTM was developed by Karim and Kennedy (1982) to compute sediment discharge based on a representative particle size but coupled with the dependence of friction factor on the sediment discharge. In the original development, the size distribution of the transported material can be predicted, but the procedure requires the separation of suspended load and bed load. In addition, the size-distribution relations used for bed load and suspended load are not identical; therefore an accurate separation procedure for suspended load and bed load is required. This has been modified to a simplified form (i.e., the modified TLTM method, Karim, 1985) in which the sediment discharge for each particle size can be computed directly, as discussed in the following section.

The Ackers-White (1973) formula is a total-load predictor, and was extended by Proffitt and Sutherland (1983) to compute nonuniform sediment transport but limited to bed-load transport. A verification with the use of flume data was carried out.

Laursen's formula can also be used to compute the sediment discharge for each particle size fraction, but due to its complexity it is not appropriate for numerical modelling.

Engelund-Hansen's formula is also coded in CHARIMA, but not evaluated herein. It has been pointed out (Garde et al., 1977) that the mechanism conceived by Engelund and Hansen does not describe the phenomenon of suspended-load transport adequately. In addition, no specific formulation has been developed yet to use this formula for computing sediment discharge by size fraction.

The four total-load predictors adopted for use in CHARIMA are the modified TLTM method, the modified Ackers-White method, the Engelund-Hansen method, and a power-law predictor.

#### Modified TLTM Method:

In reference to Karim's development (1985) the dependence of friction factor on sediment transport can be decoupled from the full system of equations. The sediment discharge predictor used is:

$$\text{Log} \left( \frac{q_s}{\sqrt{g(s-1)D_{50}^3}} \right) = a_0 + a_1 \log V_1 + a_2 \log V_1 \log V_3 + a_3 \log V_2 \log V_3 \quad (\text{II.21})$$

in which

$$V_1 = \frac{U}{\sqrt{g(s-1)D_{50}}}; \quad V_2 = \frac{d}{D_{50}}; \quad V_3 = \frac{u_* - u_{*c}}{\sqrt{g(s-1)D_{50}}}$$

where  $q_s$  is the total sediment discharge per unit width;  $U$  is mean velocity;  $d$  is mean depth of flow; and  $a_0, a_1, a_2, a_3$  are the coefficients determined from regression analysis ( $a_0 = -2.278$ ;  $a_1 = 2.972$ ;  $a_2 = 1.06$ ; and  $a_3 = 0.299$  for the 615 flows analyzed by Karim and Kennedy (1982)). The relation proposed for the sediment discharge by size fraction is:

$$q_{s_j} = q_s(D_j) W_j P_{t_j} \quad (\text{II.22})$$

where  $q_{sj}$  is the sediment discharge for particle size  $j$ ;  $q_s(D_j)$  is the sediment discharge computed from Eq. (II.21) by the use of  $D_j$  instead of  $D_{50}$ ;  $P_{tj}$  is the proportion of size fraction  $j$  in the bed material; and,  $W_j$  is a correction factor. In Karim's original approach (i.e., TLTM, 1982), the sediment discharge is computed by the use of median size  $D_{50}$  and then distributed to each size fraction by a distribution relation developed by Karim and Kennedy (1982). This original method requires the total load to be separated into suspended and bed loads.

Karim's proposed relation for  $W_j$  is as follows:

$$W_j = b_1 \left( \frac{D_j}{D_u} \right)^{b_2} \quad (\text{II.23})$$

where  $b_1$  and  $b_2$  are coefficients which may have to be calibrated for particular models; and,  $D_u$  is the representative size of the bed material. Usually  $D_{50}$  is taken as the representative size, in this and other studies.  $W_j$  can be recognized as a hiding factor, which reflects the fact that smaller particles seem to "hide" behind larger ones. Although no definitive relation for  $W_j$  has yet been found, a successful application of Eq. (II.23) to the schematized Missouri-River model has been performed by Karim (1985):

#### Modified Ackers-White Method:

The formula developed by Ackers and White for uniform bed material is:

$$\bar{C}_T = \frac{\gamma_s D c_2 \left( \frac{F_0}{c_3} - 1 \right)^{c_4}}{(u_* / U)^{c_1} \gamma_f d} \quad (\text{II.24})$$

in which

$$F_o = \left( \frac{u_*^{c_1}}{\sqrt{(s-1) g D_{35}}} \right) \left( \frac{U}{\sqrt{32 \log (10d/D_{35})}} \right)^{1-c_1} \quad (\text{II.25})$$

$$d_* = ((s-1) g/v^2)^{1/3} D_{35} \quad (\text{II.26})$$

For  $1.0 < d_* < 60.0$ ,

$$c_1 = 1.0 - 0.56 \log d_*$$

$$c_2 = 10^{(2.86 \log d_* - (\log d_*)^2 - 3.53)}$$

$$c_3 = 0.23/d_*^{1/2} + 0.14$$

$$c_4 = 9.66/d_* + 1.34$$

For  $d_* > 60.0$

$$c_1 = 0.0$$

$$c_2 = 0.025$$

$$c_3 = 0.17$$

$$c_4 = 1.5$$

where  $\bar{C}_T$  is sediment flux concentration (sediment mass flux per unit mass flow rate). To apply this formula to nonuniform material,  $D_{35}$  has to be replaced by each particle size, and the mobility number  $F_0$  has to be modified by the exposure correction factor  $\epsilon_j$  which is defined as:

$$\epsilon_j = \frac{F_0 \text{ (to satisfy the measured data)}}{F_0 \text{ (from Eq. (II.25) with } D = D_j)} \quad (\text{II.27})$$

Proffitt and Sutherland give  $\epsilon_j$  as follows:

$$\epsilon_j = 1.3, \quad D_j/D_u > 3.7 \quad (\text{II.28})$$

$$\epsilon_j = 0.53 \log (D_j/D_u) + 1.0, \quad 0.075 < D_j/D_u < 3.7 \quad (\text{II.29})$$

$$\epsilon_j = 0.4, \quad D_j/D_u < 0.075 \quad (\text{II.30})$$

The scaling size  $D_u$  can be determined by another relation given by Proffitt and Sutherland:

$$\frac{D_u}{D_{50}} = f[u_*^2/g(s-1) D_{50}] \quad (\text{II.31})$$

However, in practice  $D_{50}$  can always be used as the effective size  $D_u$ .

#### Engelund-Hansen Method:

The formula developed by Engelund and Hansen (1967) for the total bed-material load capacity is:

$$g_s = 0.05 \gamma_s V^2 \sqrt{\frac{D_{50}}{g \left( \frac{\gamma_s}{\gamma} - 1 \right)}} \left[ \frac{\tau_o}{(\gamma_s - \gamma) D_{50}} \right]^{3/2} \quad (\text{II.31A})$$

$$q_s \text{ (discharge per unit width)} = g_s / \gamma_s$$

in which  $g_s$  = the bed material discharge in weight per unit width;  $V$  = mean flow velocity;  $D_{50}$  = median fall diameter of bed sediment;  $\tau_o = \gamma d S_f$  = average shear stress at bed level;  $d$  = flow depth. This formula is unit-consistent.

This formula is based on data from four sets of experiments in a large flume 8 ft wide and 150 ft long. The sediments in these experiments had median full diameters of 0.19 mm, and 0.27 mm, 0.45 mm and 0.93 mm, respectively, and geometric standard deviations of particle sizes of 1.3 for the finest sediment and 1.6 for the others.

#### Power-Law Method:

From a practical point of view, when a river or flume under simulation already has its own empirical relations between flow condition and sediment-transport rate, it is more reliable to use those relationships instead of a more general sediment-transport predictor. Based on measured data, one can construct a power-law relation between sediment transport rate and several flow parameters, e.g. discharge  $Q$ , velocity  $V$  etc. The most reasonable way is generally to choose the effective velocity, that is the surplus velocity beyond that needed for incipient motion ( $U - U_c$ ):

$$q_s = a (U - U_c)^b \quad (\text{II.31b})$$

in which  $q_s$  = sediment discharge per unit width ( $L^3/TL$ );  $a, b$  = regression constants from analysis of available data;  $U$  = average velocity;  $U_c$  = critical velocity when sediment

begins to move.  $U_c$ (ft/s) can be based, for example, on the ASCE manual "Sedimentation Engineering" Eq. (2.121),

$$U_c = 0.5 \left( \frac{\gamma_s}{\gamma} - 1 \right)^{1/2} d_g^{4/9} \quad (\text{II.31c})$$

in which  $d_g$  = the appropriate sediment size in millimeters, often taken as the geometric mean of the sizes defining size-class intervals for sediment mixtures. It is important to use the correct units which are consistent with the regression data since this formula is empirical and not dimensionless.

**II.3.2. Critical Shear Stress** As pointed out by many researchers, the rate of sediment transport is very sensitive to the transporting power, which can be expressed as a function of bed-shear force. This relationship can be observed in many of the sediment-discharge formulae commonly used. Inaccuracy in the determination of the critical shear force for the particle's incipient motion will lead to large errors of prediction of sediment transport capacity under given flow conditions.

Many studies have been performed to determine the critical tractive stress. However, every resulting predictive formulation has its own limitation due to the fact that the experiment carried out by each researcher used a limited range of sediment size and other constraints. The curve that Rouse (1939) fitted to Shields' diagram is still the most commonly used predictor, although some limitations have been pointed out. Egiazaroff (1965) indicated that the nonuniformity of the mixture greatly influences the mobility of particles. When particle diameter is greater than the average diameter of both particles in movement and bed material, the dimensionless critical shear stress will be less than the value of 0.06 which was obtained by Shields for large Reynolds number as shown in Figure II.2; the particle is more mobile than uniform particles of the same size. If particle diameter is less than the average diameter of both particles in movement and bed material, then the dimensionless critical shear stress will be greater than 0.06; the mobility of such particles is less than that of uniform particles. Thus, larger particles have high mobility in the mixture, and these larger particles tend to shelter the smaller particles. For a completely rough boundary, Neill (1968) has observed that the dimensionless critical shear stress value is on the high side and the true critical condition may occur for a critical shear stress

of about 0.03. Furthermore, in a recent study by Shen and Lu (1983), the authors indicated that the effects of turbulence level and protrusion are important in the determination of critical shear stress for nonuniform bed material. As the standard deviation increases, the true critical shear stress will deviate increasingly from Rouse's curve. They therefore used a modification of Rouse's curve in their study.

Many other techniques have been developed to take into account the effect of nonuniformity for the determination of critical shear stress. Some examples pointed out by Garde and Ranga Raju (1977) are those of Kramer (1939), USWES (1937), Chang (1939), Indri (1956), Aki and Sata (1956), and Sakai (1956). However, in spite of the fact that many such methods are available, they are always rather difficult to formulate in the context of numerical modelling due to the difficulty of adjusting some empirical coefficients appearing in the formulation.

Based on the above-mentioned phenomena of sheltering effects and increased mobility of coarser particle in the mixture, the equation developed by Iwagaki (1956) appears to be an appropriate one and is compared with Rouse's curve herein. As shown in Figure II.2, it is obvious that the critical shear stress for the smaller particles is greater than that in Rouse's curve, and for larger particles it is smaller. Iwagaki's formulation can be expressed as follows:

$$R_o^* = (s-1)^{1/2} g^{1/2} D^{3/2} / \nu \quad (\text{II.32})$$

$$R_o^* \geq 671, \quad \tau_{oc}/(\gamma_s - \gamma_f) D = 0.05$$

$$162.7 \leq R_o^* \leq 671, \quad \tau_{oc}/(\gamma_s - \gamma_f) D = 8.45 \times 10^{-3} (R_o^*)^{3/11}$$

$$54.2 \leq R_o^* \leq 162.7, \quad \tau_{oc}/(\gamma_s - \gamma_f) D = 0.034 \quad (\text{II.33})$$

$$2.14 \leq R_o^* \leq 54.2, \quad \tau_{oc}/(\gamma_s - \gamma_f) D = 0.195 (R_o^*)^{-7/16}$$

$$R_o^* \leq 2.14, \quad \tau_{oc}/(\gamma_s - \gamma_f) D = 0.14$$

Iwagaki (1956) considered the equilibrium of a single spherical particle placed on a rough surface and derived an analytical formulation for determining the beginning of motion of the particle. Furthermore, in order to take into account the sheltering effect, he introduced an empirical coefficient and constructed the curve as given in Figure II.2.

In order to have the new code as general as possible, both Rouse's and Iwagaki's curves are coded in the program. If any better formulations are developed, they also can be easily inserted in these codes without any major change in the program structure.

**II.3.3. Friction Factor** The friction-factor predictor developed by Karim and Kennedy (1982) is used herein, as follows:

$$\frac{U}{\sqrt{g(s-1)D_{50}}} = c_5 \left( \frac{q}{\sqrt{g(s-1)D_{50}^3}} \right)^{c_6} (S_f \cdot 10^3)^{c_7} \quad (\text{II.34})$$

where  $q$  = unit water discharge; and  $c_5$ ,  $c_6$ , and  $c_7$  are the coefficients determined from the regression analysis of a given data base. For the 615 flows analyzed by Karim and Kennedy (1982), these coefficients are  $c_5 = 0.33$ ,  $c_6 = 0.376$ , and  $c_7 = 0.310$ .

**II.3.4. Dune-Height Predictor** Allen's relation (1978) is as follows:

$$H_d = d \left[ e_0 + e_1 \left( \frac{\eta}{3} \right) + e_2 \left( \frac{\eta}{3} \right)^2 + e_3 \left( \frac{\eta}{3} \right)^3 + e_4 \left( \frac{\eta}{e} \right)^4 \right];$$

$$(0.25 \leq \eta \leq 1.5) \quad (\text{II.35})$$

where  $\eta = \tau_o/(\rho(s-1)gD_{50})$ ;  $\tau_o$  = bed shear stress;  $e_0 = 0.079865$ ;  $e_1 = 2.23897$ ;  $e_2 = -18.1264$ ;  $e_3 = 70.9001$ ; and  $e_4 = -88.3293$ . The relation developed by Yalin et al. (1979) is:

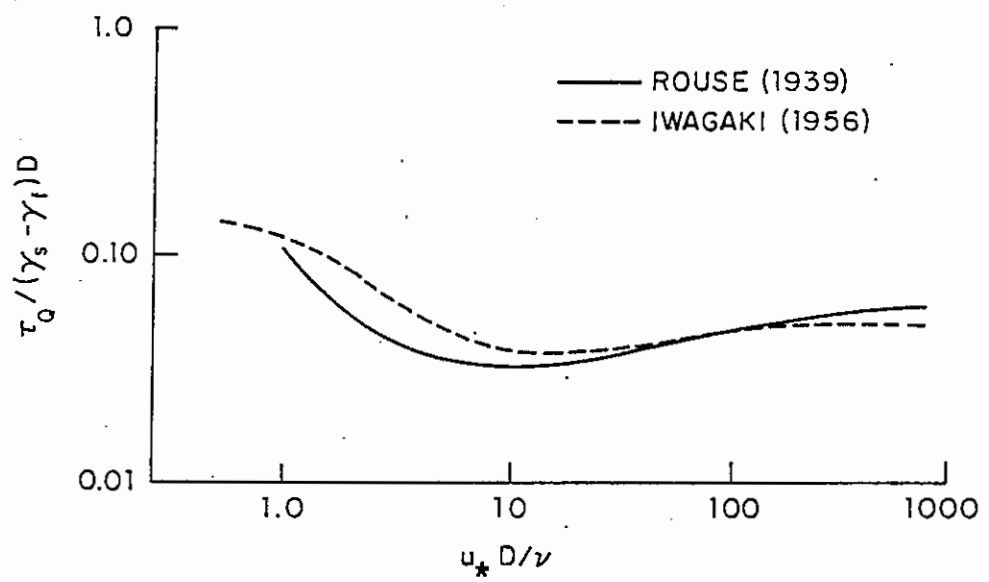


Figure II.2. Condition for incipient motion.

$$\frac{\delta}{\delta_{\max}} = \varepsilon_d \exp(1 - \varepsilon_d) \quad (\text{II.36})$$

in which

$$\begin{aligned} \varepsilon_d &= x\sqrt{\bar{x}} \\ x &= \text{dimensionless excess of the tractive force;} \\ \bar{x} &= \text{value of } x \text{ corresponding to } \delta_{\max}; \\ \delta &= H_d/\Lambda = \text{dune steepness;} \\ \delta_{\max} &= \text{maximum value of } \delta \text{ corresponding to a given } \bar{x}; \end{aligned}$$

From Eq. (II.36) if  $d/D$  and  $x$  are known, then  $H_d$  can be solved. Based on Yalin et al. (1978),

$$\begin{aligned} \delta_{\max} = 0.0095, \bar{x} = 2.03; & \quad 20 \leq d/D \leq 30 \\ \delta_{\max} = 0.018, \bar{x} = 3.85; & \quad 40 \leq d/D \leq 50 \\ \delta_{\max} = 0.027, \bar{x} = 5.78; & \quad 65 \leq d/D \leq 75 \\ \delta_{\max} = 0.006, \bar{x} = 12.84; & \quad 100 \leq d/D \end{aligned} \quad (\text{II.37})$$

In order to compute the dune height  $H_d$ , the length of dune has to be determined. In general, under the assumption of fully developed turbulent flow, the following relation can be used for the dune length:

$$\Lambda = 2\pi d \quad (\text{II.38})$$

However, if  $d/D$  is smaller than about 25, then

$$\Lambda \approx 20 d \quad (\text{II.39})$$

Therefore, from Eqs. (II.37-39), the dune height can be obtained.

#### II.4. Unsteady Flow Computation

**II.4.1. Introduction** In a single-channel model, each computational point is hydraulically linked only to two other points, immediately upstream and downstream. Moreover, the flow at a point is governed by the conditions at two boundary points at which the discharge, the water level, or relation between them is known. The flow paths from a point to its governing boundary points are unique; the significant result is that the matrix of linearized flow equations for the network is not only sparse, but also banded (tri-diagonal or penta-diagonal). This type of matrix can be efficiently solved using techniques such as the double-sweep method (Carnahan et al, 1969; Liggett and Cunge, 1975). The same conclusions hold true for branched networks in which channel junctions serve as interior boundary conditions, making it possible to use single-channel solution techniques.

In multiply-connected networks, on the other hand, flow at a point can directly depend on flow at several other points, and there is no unique path to boundary points. In this case the matrix of flow equations is sparse but not simply banded. Taking advantage of this sparsity, the algorithm described in the following sections still allows the system of equations to be solved without inverting the whole matrix, at the price of considerable increase in algorithmic complexity.

Figure II.3 establishes some definitions to be used in the sequel. A node is any junction of two or more links, or a boundary point; a link is any flow path beginning at one node and ending at another; a point is any location along a link at which the cross section is known and with which hydraulic parameters are associated; a reach is any stretch of channel between two points. Any link always has at least two points, one associated with the node at each end.

**II.4.2. Node Continuity** At nodes, the water-continuity equation (inflow = outflow) is applied. For any node  $m$  at time level  $n+1$ , the continuity equation can be written:

$$Q_m(t_{n+1}) + \sum_{\ell=1}^{L(m)} Q_{m,\ell}^{n+1} = 0, \quad m = 1, 2, \dots, M \quad (\text{II.40})$$

where  $L(m)$  denotes the total number of links connected to node  $m$ ,  $M$  is the total number of nodes in the network, and  $Q_m(t_{n+1})$  is any external inflow to node  $m$  at time  $t_{n+1}$ . If the discharge is expressed as the sum of the latest estimate  $Q$  and a correction to that estimate  $\Delta Q$  Eq. (II.40) can be rewritten as

$$Q_m(t_{n+1}) + \sum_{\ell=1}^{L(m)} Q_{m,\ell} + \sum_{\ell=1}^{L(m)} \Delta Q_{m,\ell} = 0, \quad m = 1, 2, \dots, M \quad (\text{II.41})$$

Now  $Q_m(t_{n+1})$  and  $Q_{m,\ell}$  are known quantities, but the  $\Delta Q_{m,\ell}$  values are unknown. The nodal solution strategy consists in using the de St. Venant equations along the links between nodes to express the  $\Delta Q$  values in terms of corrections to water surface elevations at the nodes.

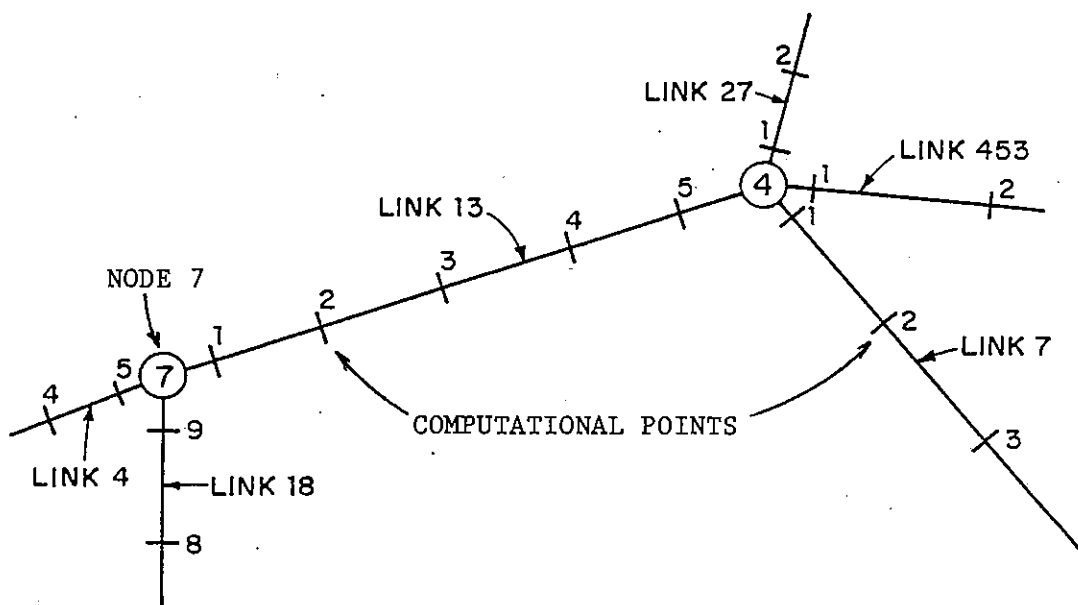


Figure II.3. Topological definition sketch.

**II.4.3. Discretization of Equations** The discretized continuity and momentum equations, based on Preissmann's finite-difference approximations, are given earlier as Eqs. (II.13) and (II.14).

As described by Liggett and Cunge (1975), with the use of Taylor's Series expansion Eqs. (II.13) and (II.14) can be written as:

$$A_o \Delta y_{i+1} + B_o \Delta Q_{i+1} = C_o \Delta y_i + D_o \Delta Q_i + G_o \quad (\text{II.42})$$

$$A'_o \Delta y_{i+1} + B'_o \Delta Q_{i+1} = C'_o \Delta y_i + D'_o \Delta Q_i + G'_o \quad (\text{II.43})$$

where  $i$  and  $i+1$  are indices of computational points at either end of the reach,  $\Delta Q$  and  $\Delta y$  are the increments of discharge and water surface elevation for every point during one iteration, and the positive flow direction is defined from  $i+1$  to  $i$ . Coefficients  $A_o, B_o, C_o, D_o, G_o, A'_o, B'_o, C'_o, D'_o, G'_o$  are as follows:

$$A_o = \phi B_{i+1} / \Delta t \quad (\text{II.44})$$

$$B_o = D_o = \theta / \Delta x \quad (\text{II.45})$$

$$C_o = - (1-\phi) B_i / \Delta t \quad (\text{II.46})$$

$$G_o = \frac{\phi}{\Delta t} \left( A_i^{n+1} - A_{i+1}^{n+1} \right) + \frac{(1-\phi)}{\Delta t} \left( A_i^n - A_i^{n+1} \right) + \frac{\theta}{\Delta x} \left( Q_{i+1}^n - Q_{i+1}^{n+1} \right) + \frac{(1-\theta)}{\Delta x} \left( Q_i^n - Q_{i+1}^n \right) \quad (\text{II.47})$$

$$A'_0 = \frac{-\alpha\theta Q_{i+1}^{n+1} B_{i+1}^{n+1}}{(A_{i+1}^{n+1})^2} \left[ \frac{\theta}{\Delta x} (Q_{i+1}^{n+1} - Q_i^{n+1}) + \frac{(1-\theta)}{\Delta x} (Q_{i+1}^n - Q_i^n) \right]$$

$$- \frac{\alpha\theta B_{i+1}^{n+1}}{\Delta x} \left[ \frac{\theta}{4} \left( \frac{Q_i^{n+1}}{A_i^{n+1}} + \frac{Q_{i+1}^{n+1}}{A_{i+1}^{n+1}} \right)^2 + \frac{1-\theta}{4} \left( \frac{Q_i^n}{A_i^n} + \frac{Q_{i+1}^n}{A_{i+1}^n} \right)^2 \right]$$

$$+ \frac{\alpha\theta Q_{i+1}^{n+1} B_{i+1}^{n+1}}{2(A_{i+1}^{n+1})^2} \left( \frac{Q_i^{n+1}}{A_i^{n+1}} + \frac{Q_{i+1}^{n+1}}{A_{i+1}^{n+1}} \right) \left[ \frac{\theta}{\Delta x} (A_{i+1}^{n+1} - A_i^{n+1}) \right.$$

$$\left. + \frac{1-\theta}{\Delta x} (A_{i+1}^n - A_i^n) \right]$$

$$+ \frac{\theta g}{\Delta x} \left[ \frac{\theta}{2} (A_i^{n+1} + A_{i+1}^{n+1}) + \frac{1-\theta}{2} (A_i^n + A_{i+1}^n) \right]$$

$$+ \frac{\theta g B_{i+1}^{n+1}}{2} \left[ \frac{\theta}{\Delta x} (y_{i+1}^{n+1} - y_i^{n+1}) + \frac{1-\theta}{\Delta x} (y_{i+1}^n - y_i^n) \right]$$

$$\begin{aligned}
& - \frac{\theta g(1-\beta) Q_{i+1}^{n+1} |Q_{i+1}^{n+1}| (K_{i+1}^{n+1})}{(K_{i+1}^{n+1})^3} \left[ \theta (A_i^{n+1} + A_{i+1}^{n+1}) + (1-\theta) (A_i^n + A_{i+1}^n) \right] \\
& + \frac{\theta g B_{i+1}^{n+1}}{2} \left\{ \theta \left[ \beta \frac{Q_i^{n+1} |Q_i^{n+1}|}{(K_i^{n+1})^2} + (1-\beta) \frac{Q_{i+1}^{n+1} |Q_{i+1}^{n+1}|}{(K_{i+1}^{n+1})^2} \right] \right. \\
& \left. + (1-\theta) \left[ \beta \frac{Q_i^n |Q_i^n|}{(K_i^n)^2} + (1-\beta) \frac{Q_{i+1}^n |Q_{i+1}^n|}{(K_{i+1}^n)^2} \right] \right\} \quad (\text{II.48})
\end{aligned}$$

$$\begin{aligned}
B'_0 &= \frac{\phi}{\Delta t} + \frac{\alpha\theta}{\Delta x} \left[ \theta \left( \frac{Q_i^{n+1}}{A_i^{n+1}} + \frac{Q_{i+1}^{n+1}}{A_{i+1}^{n+1}} \right) + (1-\theta) \left( \frac{Q_i^n}{A_i^n} + \frac{Q_{i+1}^n}{A_{i+1}^n} \right) \right] \\
& + \frac{\alpha\theta}{\Delta x A_{i+1}^{n+1}} \left[ \theta (Q_{i+1}^{n+1} - Q_i^{n+1}) + (1-\theta) (Q_{i+1}^n - Q_i^n) \right] \\
& - \frac{\alpha\theta}{2A_{i+1}^{n+1}} \left( \frac{Q_i^{n+1}}{A_i^{n+1}} + \frac{Q_{i+1}^{n+1}}{A_{i+1}^{n+1}} \right) \left[ \frac{\theta}{\Delta x} (A_{i+1}^{n+1} - A_i^{n+1}) + \frac{1-\theta}{\Delta x} (A_{i+1}^n - A_i^n) \right]
\end{aligned}$$

$$+ \frac{g\theta(1-\beta) |Q_{i+1}^{n+1}|}{(K_{i+1}^{n+1})^2} \left[ \theta (A_i^{n+1} + A_{i+1}^{n+1}) + (1-\theta) (A_i^n + A_{i+1}^n) \right] \quad (\text{II.49})$$

$$C'_0 = \frac{\alpha\theta B_i^{n+1} Q_i^{n+1}}{(A_i^{n+1})^2} \left[ \frac{\theta}{\Delta x} (Q_{i+1}^{n+1} - Q_i^{n+1}) + \frac{1-\theta}{\Delta x} (Q_{i+1}^n - Q_i^n) \right]$$

$$- \frac{\alpha\theta B_i^{n+1}}{\Delta x} \left[ \frac{\theta}{4} \left( \frac{Q_i^{n+1}}{A_i^{n+1}} + \frac{Q_{i+1}^{n+1}}{A_{i+1}^{n+1}} \right)^2 + \frac{1-\theta}{4} \left( \frac{Q_i^n}{A_i^n} + \frac{Q_{i+1}^n}{A_{i+1}^n} \right)^2 \right]$$

$$- \frac{\alpha\theta B_i^{n+1} Q_i^{n+1}}{(A_i^{n+1})^2} \left( \frac{Q_i^{n+1}}{A_i^{n+1}} + \frac{Q_{i+1}^{n+1}}{A_{i+1}^{n+1}} \right) \left[ \frac{\theta}{\Delta x} (A_{i+1}^{n+1} - A_i^{n+1}) + \frac{1-\theta}{\Delta x} (A_{i+1}^n - A_i^n) \right]$$

$$+ \frac{\theta g}{2\Delta x} \left[ \theta (A_i^{n+1} + A_{i+1}^{n+1}) + (1-\theta) (A_i^n + A_{i+1}^n) \right]$$

$$+ \frac{\theta g B_i^{n+1}}{2\Delta x} \left[ \theta (y_{i+1}^{n+1} - y_i^{n+1}) + (1-\theta) (y_{i+1}^n - y_i^n) \right]$$

$$\begin{aligned}
& + \frac{\theta \beta g (K_i^{n+1}) Q_i^{n+1} |Q_i^{n+1}|}{(K_i^{n+1})^3} \left[ \theta (A_i^{n+1} + A_{i+1}^{n+1}) + (1-\theta) (A_i^n + A_{i+1}^n) \right] \\
& - \frac{\theta g B_i^{n+1}}{2} \left\{ \theta \left[ \beta \frac{Q_i^{n+1} |Q_i^{n+1}|}{(K_i^{n+1})^2} + (1-\beta) \frac{Q_{i+1}^{n+1} |Q_{i+1}^{n+1}|}{(K_{i+1}^{n+1})^2} \right] \right. \\
& \left. + (1-\theta) \left[ \beta \frac{Q_i^n |Q_i^n|}{(K_i^n)^2} + (1-\beta) \frac{Q_{i+1}^n |Q_{i+1}^n|}{(K_{i+1}^n)^3} \right] \right\} \tag{II.50}
\end{aligned}$$

$$\begin{aligned}
D_o' &= \frac{\phi-1}{\Delta t} + \frac{\alpha \theta}{\Delta x} \left[ \theta \left( \frac{Q_i^{n+1}}{A_i^{n+1}} + \frac{Q_{i+1}^{n+1}}{A_{i+1}^{n+1}} \right) + (1-\theta) \left( \frac{Q_i^n}{A_i^n} + \frac{Q_{i+1}^n}{A_{i+1}^n} \right) \right] \\
& - \frac{\alpha \theta}{A_i^{n+1}} \left[ \frac{\theta}{\Delta x} (Q_{i+1}^{n+1} - Q_i^{n+1}) + \frac{1-\theta}{\Delta x} (Q_{i+1}^n - Q_i^n) \right] \\
& + \frac{\alpha \theta}{2A_i^{n+1}} \left( \frac{Q_i^{n+1}}{A_i^{n+1}} + \frac{Q_{i+1}^{n+1}}{A_{i+1}^{n+1}} \right) \left[ \frac{\theta}{\Delta x} (A_{i+1}^{n+1} - A_i^{n+1}) + \frac{(1-\theta)}{\Delta x} (A_{i+1}^n - A_i^n) \right]
\end{aligned}$$

$$-\frac{g\theta\beta|Q_i^{n+1}|}{(K_i^{n+1})^2} \left[ \theta (A_i^{n+1} + A_{i+1}^{n+1}) + (1-\theta) (A_i^n + A_{i+1}^n) \right] \quad (\text{II.51})$$

$$-G'_0 = \frac{\phi}{\Delta t} (Q_{i+1}^{n+1} - Q_{i+1}^n) + \frac{1-\phi}{\Delta t} (Q_i^{n+1} - Q_i^n)$$

$$+ \left[ \alpha\theta \left( \frac{Q_i^{n+1}}{A_i^{n+1}} + \frac{Q_{i+1}^{n+1}}{A_{i+1}^{n+1}} \right) + \alpha(1-\theta) \left( \frac{Q_i^n}{A_i^n} + \frac{Q_{i+1}^n}{A_{i+1}^n} \right) \right]$$

$$\left[ \frac{\theta}{\Delta x} (Q_{i+1}^{n+1} - Q_i^{n+1}) + \frac{1-\theta}{\Delta x} (Q_{i+1}^n - Q_i^n) \right]$$

$$- \alpha \left[ \frac{\theta}{4} \left( \frac{Q_i^{n+1}}{A_i^{n+1}} + \frac{Q_{i+1}^{n+1}}{A_{i+1}^{n+1}} \right)^2 + \frac{1-\theta}{4} \left( \frac{Q_i^n}{A_i^n} + \frac{Q_{i+1}^n}{A_{i+1}^n} \right)^2 \right]$$

$$\left[ \frac{\theta}{\Delta x} (A_{i+1}^{n+1} - A_i^{n+1}) + \frac{1-\theta}{\Delta x} (A_{i+1}^n - A_i^n) \right]$$

$$+ g \left[ \frac{\theta}{2} (A_i^{n+1} + A_{i+1}^{n+1}) + \frac{1-\theta}{2} (A_i^n + A_{i+1}^n) \right]$$

$$\begin{aligned}
& \left[ \frac{\theta}{\Delta x} \left( y_{i+1}^{n+1} - y_i^{n+1} \right) + \frac{1-\theta}{\Delta x} \left( y_{i+1}^n - y_i^n \right) \right] \\
& + g \left[ \frac{\theta}{2} \left( A_i^{n+1} + A_{i+1}^{n+1} \right) + \frac{1-\theta}{2} \left( A_i^n + A_{i+1}^n \right) \right] \\
& \left\{ \theta \left[ \beta \frac{Q_i^{n+1} |Q_i^{n+1}|}{(K_i^{n+1})^2} + (1-\beta) \frac{Q_{i+1}^{n+1} |Q_{i+1}^{n+1}|}{(K_{i+1}^{n+1})^2} \right] \right. \\
& \left. + (1-\theta) \left[ \beta \frac{Q_i^n |Q_i^n|}{(K_i^n)^2} + (1-\beta) \frac{Q_{i+1}^n |Q_{i+1}^n|}{(K_{i+1}^n)^2} \right] \right\} \quad (II.52)
\end{aligned}$$

**II.4.4. Formulation of Nodal Matrix Equation** The unsteady flow algorithm is essentially that described by Cunge et al. (1980) for multiply connected networks.

Suppose that there are  $I$  computational points along a link  $\ell$ . For any pair of points  $(i, i+1)$ , Eqs. (II.42) and (II.43) may be written as,

$$\Delta y_{i+1} = L_{i+1} \Delta y_i + M_{i+1} \Delta Q_i + N_{i+1} \quad (II.53)$$

where,

$$L_{i+1} = (C_o B_o' - C_o' B_o) / x_1 \quad (II.54)$$

$$M_{i+1} = (D_o B_o' - D_o' B_o) / x_1 \quad (II.55)$$

$$N_{i+1} = (G_o B_o' - G_o' B_o) / x_1 \quad (II.56)$$

$$x1 = A_o B_o' - A_o' B_o$$

Again, suppose that it is possible to express the discharge increment at any intermediate point  $i$  of the link  $\ell$  as a function of two water level increments:

$$\Delta Q_i = E_i \Delta y_i + F_i + H_i \Delta y_I \quad (\text{II.57})$$

where,

$$E_i = [C_o - L_{i+1}(A_o + B_o E_{i+1})]/x2 \quad (\text{II.58})$$

$$F_i = [G_o - (A_o + B_o E_{i+1}) N_{i+1} - B_o F_{i+1}]/x2 \quad (\text{II.59})$$

$$H_i = - B_o H_{i+1}/x2 \quad (\text{II.60})$$

$$x2 = (A_o + B_o E_{i+1}) M_{i+1} - D_o$$

and  $\Delta y_I$  is the water-level correction at point  $i = I$ , the last point on the link.

Coefficients  $E$ ,  $F$ , and  $H$  at point  $i = I$  for each link cannot be obtained directly, since the hydraulic conditions are not known a priori (except at a boundary point). However, the recursion relation can always proceed downstream without knowing the conditions at point  $I$ , because coefficients  $E$ ,  $F$ , and  $H$  at the second point can be obtained directly from Eqs. (II.42, II.43, and II.54):

$$E_{I(\ell)-1} = (C_o' B_o - C_o B_o')/x3 \quad (\text{II.61})$$

$$F_{I(\ell)-1} = (G_o' B_o - G_o B_o')/x3 \quad (\text{II.62})$$

$$H_{I(\ell)-1} = (A_o B_o' - A_o' B_o)/x3 \quad (\text{II.63})$$

$$x3 = D B' - D' B$$

Thus, once  $E$ ,  $F$ , and  $H$  have been initialized by Eqs. (II.61-II.63), the remaining  $E_i$ ,  $F_i$ ,  $H_i$  coefficients can be calculated by recurrence using Eqs. (II.58-60) for  $i = I(\ell) - 1, \dots, 2$ . In particular, once  $E_i$ ,  $F_i$ , and  $H_i$  for  $i = 2$  are known, Eqs. (II.57) can be written for  $i = 1$  as:

$$\Delta Q_1 = E_1 \Delta y_1 + F_1 + H_1 \Delta y_{I(\ell)} \quad (\text{II.64})$$

Now the same procedures are needed to find the nodal relation for point I. Again, suppose

$$\Delta Q_{I(\ell)} = E'_{i+1} \Delta y_{i+1} + F'_{i+1} + H'_{i+1} \Delta y_{I(\ell)} \quad (\text{II.65})$$

From Eqs. (II.42, II.53, II.57, II.65), the following recursion relations can be obtained:

$$E'_i = E'_{i+1} (C_0 M_{i+1} - D_0 L_{i+1}) / x4 \quad (\text{II.66})$$

$$F'_i = E'_{i+1} [(G_0 - B_0 F_{i+1}) M_{i+1} - D_0 N_{i+1}] / x4 \quad (\text{II.67})$$

$$H'_i = -B_0 H_{i+1} E'_{i+1} M_{i+1} / x4 \quad (\text{II.68})$$

$$x4 = (A_0 + B_0 E_{i+1}) M_{i+1} - D_0$$

Now for  $i = I(\ell) - 1$ ,

$$E'_{I(\ell)-1} = (C_0 D'_0 - C'_0 B_0) / x5 \quad (\text{II.69})$$

$$F'_{I(\ell)-1} = (G_0 D'_0 - G'_0 D_0) / x5 \quad (\text{II.70})$$

$$H'_{I(\ell)-1} = (A_0 D'_0 - A'_0 D_0) / x5 \quad (\text{II.71})$$

$$x5 = B_0 D'_0 - B'_0 D_0$$

Therefore,

$$\Delta Q_{I(\ell)} = E'_1 \Delta y_1 + F'_1 + H'_1 \Delta y_{I(\ell)} \quad (\text{II.72})$$

A relation among the water-level changes at adjacent nodes is established by substituting Eqs. (II.64) and (II.72) into the node continuity equation, Eq. (II.41). This leads to the matrix equation

$$[A]\{\Delta y\} = \{B\} \quad (II.73)$$

where [A] is a coefficient matrix comprising appropriate summations of E, H, E', and H' coefficients, and {B} is a known vector whose elements are imposed inflows, and sums of latest discharge estimates, F, and F' coefficients.

**II.4.5. Solution Strategy in One Iteration** The preceding section outlines the computational elements which are used to obtain corrections to a given set of water levels at points and discharges in links. The corrections may be needed because the inflows to the system have changed (typically the case for the first iteration); or because the sediment operations have changed the system geometry since the last estimate; or because several iterations may be needed to converge to obtain a set of levels and discharges which simultaneously satisfy node continuity, reach continuity and momentum equations (even when neither system inflows nor system geometry are changing). The purpose of this section is to outline the procedure for computing a set of corrections.

The general solution algorithm comprises four phases for each iteration: link forward sweep, node matrix loading, node solution, link backward sweep. These are described as follows:

#### Link Forward Sweep

- For each link  $\ell$ ,  $\ell = 1, \text{LINKS}$
- For each point  $i$ ,  $i = 1, I(\ell)-1$ :
  - \* compute  $A_O, B_O, C_O, D_O, G_O, A'_O, B'_O, C'_O, D'_O$ , and  $G'_O$  by Eqs. (II.44-52)
  - \* compute coefficients, E, F, H, E', F', and H' by Eqs. (II.58-63, II.66-71).

### Node Matrix Loading

- For downstream boundary nodes acquire the imposed water level  $Y_m(t_{n+1})$ , and replace the downstream boundary nodes' "continuity" equations by

$$\Delta Y_m = Y_m(t_{n+1}) - Y_m^n \quad (\text{II.74})$$

- For each non-boundary node m:
  - \* acquire the external inflow  $Q_m(t_{n+1})$ , if any, and load in appropriate term of {B}.
- For each link attached to node m,  $\ell = 1, L(m)$ 
  - \* retrieve  $E_1, F_1, H_1, E_1', F_1', H_1'$
  - \* accumulate  $Q_1$  (or  $Q_I$ ),  $F_1$  (or  $F_1'$ ) in appropriate term of {B}
  - \* accumulate  $E_1, H_1, E_1', H_1'$  in appropriate elements of [A]

$$\{\Delta Y\} = [A]^{-1} \{B\} \quad (\text{II.75})$$

### Link Backward Sweep

- For each link,  $\ell, \ell = 1, \text{LINKS}$ :
  - \* set  $\Delta y_{1,\ell} = \Delta Y_{m1}$ ,  $m1 =$  node to which the  $i = 1$  end of link  $\ell$  is attached
  - \* set  $\Delta y_{I,\ell} = \Delta Y_{mI}$ ,  $mI =$  node to which the  $i = I(\ell)$  end of link  $\ell$  is attached
  - \* compute  $\Delta Q_1, \Delta Q_I$  from Eqs. (II.57) and (II.64)
- For each point  $i, i = 2, I(\ell)-1$ :
  - \* compute  $\Delta Q_i, \Delta y_i$  from Eqs. (II.57) and (II.53)
  - \* compute  $y_i^{n+1} = y_i + \Delta y_i; Q_i^{n+1} = Q_i + \Delta Q_i$

It should be noted that in the above procedures, the upstream boundary conditions (imposed discharge entering any upstream limits) are handled naturally through the inflow  $Q_m(t_{n+1})$  appearing in Eq. (II.41). Indeed, this external inflow is strictly optional for all interior nodes, but absolutely essential for all boundary nodes.

**II.4.6. Inversion of Nodal Coefficient Matrix** The node-solution computation of Eq. (II.73) is straightforward in principle, but must be examined more carefully in practice. Since the size of the matrix (number of nodes in the network) may be

quite large, any direct inversion computation would be prohibitively expensive, unless performed using a dedicated matrix processor. Although it is tempting to employ an iterative or overrelaxation inversion procedure such as Gauss-Seidel, this too can be expensive due to the large number of iterations, and possibly troublesome when the matrix loses diagonal dominance. Moreover, node continuity requires a more accurate solution for the node water-level changes than an approximate iterative procedure generally can achieve.

These difficulties have led to the adoption of a block tri-diagonal matrix solution technique which, though algebraically complex and delicate to program, offers both computational economy and high accuracy. The method used in this study closely parallels that described in Mahmood and Yevjevich (1975).

The basic goal of the block tridiagonal matrix technique is to replace the inversion of a NODES x NODES matrix by the inversion of NG matrices, each of size MAXG x MAXG, where NG is the total number of node groups, and MAXG is the maximum number of nodes in a node group.

By definition, a node group is a group of nodes which contains nodes which are linked only to each other, or to nodes of the previous group, or to nodes of the following group. In the following derivations the subscript ng denotes the node group numbers,  $1 < ng < NG$ .

The node continuity equations Eq. (II.73) for a node group which is neither the first, nor the last, can be written:

$$[R]_{ng} \{\Delta Y\}_{ng-1} + [S]_{ng} \{\Delta Y\}_{ng} + [T]_{ng} \{\Delta Y\}_{ng+1} = \{V\}_{ng} \quad (II.76)$$

where  $\{\Delta Y\}_{ng}$  denotes the vector of nodal water-level corrections in node group ng, etc., matrices [R], [S], [T] can be thought of as sub-matrices of [A] in Eq. (II.73) and the vector {V} can be thought of as a sub-vector of {B} in Eq. (II.73).

If NGS denotes the number of nodes in a node group then the dimensions of the elements in Eq. (II.76) are as shown in Table II.1.

In order to develop an algorithm which requires inversion of matrices having square dimensions no larger than the number of nodes in the largest node group, one first proposes a relation of the form:

$$\{\Delta Y\}_{ng-1} = [E]_{ng-1} \{\Delta Y\}_{ng} + \{F\}_{ng-1} \quad (II.77)$$

where  $[E]_{ng-1}$  is an (unknown) matrix having  $NGS_{ng}$  columns and  $NGS_{ng-1}$  rows, and  $\{F\}_{ng-1}$  are (unknown) vectors having  $NGS_{ng-1}$  rows. If Eq. (II.77) is substituted into Eq. (II.76), the resulting expression becomes a relationship between  $\{\Delta Y\}_{ng}$  and  $\{\Delta Y\}_{ng+1}$  which can be written:

Table II.1  
Dimensions of block tri-diagonal matrix  
elements

Element	Number of Columns	Number of Rows
$\{\Delta Y\}_{ng-1}$	1	$NGS_{ng-1}$
$\{\Delta Y\}_{ng}$	1	$NGS_{ng}$
$\{\Delta Y\}_{ng+1}$	1	$NGS_{ng+1}$
$[R]_{ng}$	$NGS_{ng-1}$	$NGS_{ng}$
$[S]_{ng}$	$NGS_{ng}$	$NGS_{ng}$
$[T]_{ng}$	$NGS_{ng+1}$	$NGS_{ng}$
$\{V\}_{ng}$	1	$NGS_{ng}$

$$\{\Delta Y\}_{ng} = [E]_{ng} \{\Delta Y\}_{ng+1} + \{F\}_{ng} \quad (II.78)$$

in which  $[E]_{ng}$  and  $\{F\}_{ng}$  are recognized as:

$$[E]_{ng} = -[T]_{ng} [ [R]_{ng} [E]_{ng-1} + [S]_{ng} ]^{-1} \quad (II.79)$$

$$\{F\}_{ng} = [ [R]_{ng} [E]_{ng-1} + [S]_{ng} ]^{-1} \{ \{V\}_{ng} - [R]_{ng} \{F\}_{ng-1} \} \quad (II.80)$$

Therefore, if  $[E]_{ng-1}$  and  $\{F\}_{ng-1}$  are known, they can be used with the always-known matrices of Eq. (II.76) to compute  $[E]_{ng}$  and  $\{F\}_{ng}$  for  $ng = 2, 3, \dots, NG$ . As for  $[E]_1$ , and  $\{F\}_1$ , they can be determined by writing Eq. (II.76) for the first node group,  $ng = 1$ , for which case there is no "previous" group  $ng-1$ :

$$[S]_1 \{\Delta Y\}_1 + [T]_1 \{\Delta Y\}_2 = \{V\}_1 \quad (II.81)$$

In Eq. (II.31) it can be immediately recognized that:

$$[E]_1 = - [S]_1^{-1} [T]_1 \quad (II.82)$$

$$\{F\}_1 = [S]_1^{-1} \{V\}_1 \quad (II.83)$$

Consequently it is possible, through Eqs. (II.76, 79, 80, 82, and 83), to compute and store  $[E]_{ng}$ ,  $\{F\}_{ng}$ ,  $ng = 1, \dots, NG$ . In this process, which can be thought of as a "matrix forward sweep", the matrix inversions appearing in Eqs. (II.79, 80, 82, and 83) involve square matrices whose dimensions are no longer than the maximum number of nodes per group.

The only remaining task is to find  $\{\Delta Y\}_{NG}$ , on the basis of which a "matrix return sweep" can be initiated. Eq. (II.76) is first written for  $ng = NG$  (no "following" group) as:

$$[R]_{NG} \{\Delta Y\}_{NG-1} + [S]_{NG} \{\Delta Y\}_{NG} = \{V\}_{NG} \quad (II.84)$$

However,  $\{\Delta Y\}_{NG}$  can be eliminated from Eq. (II.84) by use of Eq. (II.77) written for  $ng = NG$ ,

$$\{\Delta Y\}_{NG-1} = [E]_{NG-1} \{\Delta Y\}_{NG} + \{F\}_{NG-1} \quad (II.85)$$

Substitution of Eq. (II.85) into Eq. (II.84) and solution for  $\{\Delta Y\}_{NG}$  yields an expression identical to the right-hand-side of Eq. (II.80) for  $ng = NG$ ; in other words,

$$\{\Delta Y\}_{NG} = \{F\}_{NG} \quad (II.86)$$

(One could have obtained Eq. (II.86) directly by recognizing that in Eq. (II.78) written for  $ng = NG$ ,  $[E]_{NG}$  must be identically zero.)

Once  $\{\Delta Y\}_{NG}$  has thus been obtained, Eq. (II.77) can be applied recursively for  $ng = NG, \dots, 2$  yielding the desired  $\{\Delta Y\}_{NG}$  vectors. The significance of the method is that it replaces inversion of the large  $[A]$  matrix in Eq. (II.76) by the inversion of  $NG$  small matrices, resulting in an enormous saving of computation time.

**II.4.7. Treatment of Weir-Equivalent Flows** Although the water-routing computation is based primarily on fluvial hydraulics as incorporated in the energy equation or the de St. Venant equations, it is useful to be able to represent certain flow paths as equivalent to flow over a weir. When overflow occurs at locations where the bank is particularly low or where man-made structures have been built or where natural levees exist, the physical situation clearly indicates the need to formulate the flow path as a weir-type link. In addition, supercritical-slope links often exist in a complex looped-channel system; in order to avoid the hydraulic anomaly caused by the supercritical flows, the weir-type link is usually used to replace the supercritical-slope channel.

Once the weir-type flow can be represented in the form of a linear relation among corrections of a discharge and two water levels, then weir-type and fluvial links need not be distinguished in the node-continuity structure upon which the water routing is based. The derivation of linear coefficients for weir-type links in both the steady and unsteady cases is given as follows:

For any non-fluvial flow such as that over a weir, the applicable flow law in general, can be written as:

$$Q^{n+1} = Q + \Delta Q = f(y_u + \Delta y_u, y_d + \Delta y_d) \quad (II.87)$$

where  $u$  denotes upstream,  $d$  denotes downstream,  $Q$ ,  $y_u$  and  $y_d$  denote latest known estimates,  $\Delta Q$ ,  $\Delta y_u$ , and  $\Delta y_d$  are unknown corrections to those estimates, and the function  $f$  denotes the appropriate hydraulic law. Through Taylor Series linearization, Eq. (II.87) can be written as:

$$Q + \Delta Q = f(y_u, y_d) + \frac{\partial f}{\partial y_u} \Delta y_u + \frac{\partial f}{\partial y_d} \Delta y_d \quad (\text{II.88})$$

Using this general expression, the coefficients of Eqs. (II.42, 43) can be immediately recognized for the two possible relations between upstream-downstream (which may change over the course of calculation) and  $i \rightarrow i+1$  (which is fixed).

i) Flow from point  $i+1$  toward point  $i$ :

Here  $y_u = y_{i+1}$ ,  $y_d = y_i$ , and  $Q > 0$  by the sign convention of Section II.4.3. For the dynamic equation,

$$A_0 = \frac{\partial f}{\partial y_u}$$

$$B_0 = -1$$

$$C_0 = -\frac{\partial f}{\partial y_d} \quad (\text{II.89})$$

$$D_0 = 0$$

$$G_0 = -f(y_u, y_d) + Q_{i+1}^n$$

For the continuity equation,

$$\begin{aligned}
A'_0 &= C'_0 = 0 \\
B'_0 &= D'_0 = 1 \\
G'_0 &= Q_i^n - Q_{i+1}^n
\end{aligned}
\tag{II.90}$$

ii) Flow from point i toward point i+1:

Here  $y_d = y_{i+1}$ ,  $y_u = y_i$ , and  $Q < 0$ . For the dynamic equation,

$$\begin{aligned}
A_0 &= - \frac{\partial f}{\partial y_d} \\
B_0 &= -1 \\
C_0 &= \frac{\partial f}{\partial y_u} \\
D_0 &= 0
\end{aligned}
\tag{II.91}$$

$$G_0 = Q_{i+1}^n + f(y_u, y_d)$$

For the continuity equation,

$$\begin{aligned}
A'_0 &= C'_0 = 0 \\
B'_0 &= D'_0 = 1 \\
G'_0 &= Q_i^n - Q_{i+1}^n
\end{aligned}
\tag{II.92}$$

The remaining task is to identify the appropriate function  $f$  for a weir. A rectangular weir is considered. Two distinct weir regimes must be treated: free flowing and flooded.

Free-Flowing Weir: Direct application of the Bernoulli Equation, neglecting approach velocity and recognizing a critical-flow control at the weir, leads to:

$$Q = f = C_{ff} B_w \frac{2}{3} \sqrt{1/3} \sqrt{2g} (y_u - y_w)^{3/2} \quad (\text{II.93})$$

with  $C_{ff}$  = free-flow discharge coefficient,  $B_w$  = crest width, and  $y_w$  = crest elevation. The required derivatives are recognized as:

$$\frac{\partial f}{\partial y_u} = C_{ff} B_w \sqrt{1/3} \sqrt{2g} (y_u - y_w)^{1/2} \quad (\text{II.94})$$

$$\frac{\partial f}{\partial y_d} \equiv 0 \quad (\text{II.95})$$

Flooded Weir: The assumptions used for the free-flowing case, along with an additional assumption that all velocity head over the weir is dissipated (no kinetic-energy recovery) lead to:

$$Q = f = C_{f\ell} B_w \sqrt{2g} (y_u - y_d)^{1/2} (y_d - y_w) \quad (\text{II.96})$$

with  $C_{f\ell}$  = flooded discharge coefficient, and

$$\frac{\partial f}{\partial y_u} = C_{f\ell} B_w \sqrt{2g} \frac{1}{2} (y_u - y_d)^{-1/2} (y_d - y_w) \quad (\text{II.97})$$

$$\frac{\partial f}{\partial y_d} = C_{f\ell} B_w \sqrt{2g} [(y_u - y_d)^{1/2} - \frac{1}{2} (y_d - y_w) (y_u - y_d)^{-1/2}] \quad (\text{II.98})$$

It can be shown that the condition which distinguishes between the two regimes is:

$$\text{Flooded: } y_d - y_w > \frac{2}{3} (y_u - y_w) \quad (\text{II.99})$$

$$\text{Free Flowing: } y_d - y_w < \frac{2}{3} (y_u - y_w) \quad (\text{II.100})$$

When  $y_d - y_w = 2(y_u - y_w)/3$ , both regimes yield the same discharge.

A practical difficulty associated with Eqs. (II.97-98) is that these derivatives approach infinity as  $y_u$  approaches  $y_d$ . The implications are that, whenever the water levels on either side of a weir are nearly or exactly equal (as in an arbitrary initial condition), a nearly singular or singular situation exists in which a small correction to either the upstream or downstream water level can induce an extremely large correction to the discharge. This singularity is obviated by linearizing Eq. (II.96) for  $(y_u - y_d) < \epsilon_w$ , where  $\epsilon_w$  is the order of 0.25 feet. The linearization is written:

$$Q = f = C_{f\ell} B_w \sqrt{2g} \left( \frac{y_u - y_d}{\epsilon_w} \right) \epsilon_w^{1/2} (y_d - y_w) \quad (\text{II.101})$$

Then the derivatives, which replace Eqs. (II.96-97), become:

$$\frac{\partial f}{\partial y_u} = C_{f\ell} B_w \sqrt{2g} (y_d - y_w) / \epsilon_w^{1/2} \quad (\text{II.102})$$

$$\frac{\partial f}{\partial y_d} = C_{f\ell} B_w \sqrt{2g} \left[ (y_u - y_d) / \epsilon_w^{1/2} - (y_d - y_w) / \epsilon_w^{1/2} \right] \quad (\text{II.103})$$

**II.4.8. Flow Stabilization Procedure for Quasi-Steady Flow** Steady flow calculations are required as part of an unsteady flow simulation study to provide a reasonable initial condition from which an unsteady simulation can be performed. For a complex river system, it is impossible to furnish an initial condition for every computational point which is close to the desired steady state. A common procedure is to

start with constant depths and an arbitrary chosen discharge, which can be zero. Obviously, a stabilization procedure is required to smooth out the discontinuities caused by the inconsistency between the initial condition, boundary conditions and the governing equations. The procedure expressed in this section basically follows the algorithm developed by Cunge et al. (1980).

The basic idea of this procedure is to allow disturbances (waves) generated by the initial discharge and water-level discontinuities to propagate out of the system as rapidly as possible. A certain systematic structure of time-step variations is used to stabilize the hydraulic conditions into a steady flow. The series of time steps must start with several small ones, so the computation will not be destroyed due to the rapid variation of water level in the early stages of flow adjustment. After the initial local disturbances are thus smoothed, the model must be run for a long equivalent time, with boundary conditions fixed, to allow for volume adjustment by following a systematic series of time steps which are progressively increased.

The time step could be increased by a certain factor whenever the maximum change in water levels becomes smaller than a specified value  $\epsilon$ . As the time steps increase, the specified criterion  $\epsilon$  itself becomes smaller and smaller. In addition, if there is danger of the flow passing locally and temporarily into supercritical regime during the stabilization phase, the convective acceleration terms in the de St. Venant equations can be suppressed for a preliminary volume stabilization; then the process can be repeated retaining the convective term to let the water-surface slope adjust itself to differences in velocity from one section to another.

Through test experience, the systematic time-step variations and the corresponding specified criterion  $\epsilon$  used to control the simulation (i.e., when the maximum water-level change is less than  $\epsilon$  the simulation proceeds to the next iteration with the larger time step), have been established as shown in the following table:

Table II.2

Systematic time-step Variations and  
corresponding criteria for flow  
stabilization procedure

$\Delta t$	$.2t_b$	$.5t_b$	$t_b$	$2t_b$	$5t_b$	$10t_b$	$20t_b$	$30t_b$	$40t_b$	$50t_b$
$\epsilon$	$50\epsilon_b$	$50\epsilon_b$	$50\epsilon_b$	$15\epsilon_b$	$7\epsilon_b$	$5\epsilon_b$	$4\epsilon_b$	$3\epsilon_b$	$2\epsilon_b$	$\epsilon_b$

where  $t_b$  is a specified fundamental time step which is determined on the basis of the given initial condition (input variable FDELTB). If the initial condition is close to the true steady-state condition,  $t_b$  can be relatively large, otherwise it must be relatively small.  $\epsilon_b$  is the specified fundamental value for the water level change, usually 0.01 feet.

As shown in the above table, the time step  $\Delta t$  is maintained until the maximum water-level change between two successive cycles is less than  $\epsilon$ , then the next larger time step is adopted, and so on. At the end of this procedure the flow is fully stabilized.

Taking the complex network of channels comprising a portion of the Susitna River as shown in Figure I.1 as an example consisting of 249 nodes, 306 links and 918 computational points, the total stabilization time, which is the sum of all time steps used to stabilize the model, is about 15 hours (the fundamental time step  $t_b$  is 5 minutes).



**Pacific Northwest**  
NATIONAL LABORATORY

*Proudly Operated by **Battelle** Since 1965*

902 Battelle Boulevard  
P.O. Box 999  
Richland, WA 99352  
1-888-375-PNNL (7665)  
[www.pnnl.gov](http://www.pnnl.gov)



U.S. DEPARTMENT OF  
**ENERGY**